Master's thesis

Numerical simulations of highly efficient quantum memories

Quantum information group, Lund university, Sweden

LUNDS UNIVERSITET

Author:
Axel Thuresson

Supervisor:
Lars Rippe

May 19, 2011

Contents

Part I
Abstract

This thesis describes a number of theoretical investigations concerning optical quantum memories where the implementation is mainly intended for rare-earth-ion-doped crystals. Most of the theoretical models are based on the Maxwell-Bloch equations which is a semi-classical model for light-matter interactions.

Quantum information science is a new and rapidly developing field that concerns information science based on quantum mechanics. Within quantum information science there are a number of subfields, such as: quantum computing, quantum cryptography and quantum communication. A quantum memory is an important component for all these subfields, especially in order to realize long-distance quantum communication. The basic requirements for a quantum memory is the ability to store qubits for a certain amount of time and release them on-demand.

The development of quantum memories is constantly moving forward and it was former believed that high optical depth was neccessary to get a high efficient memory. A number of publications recently published have shown that this is not neccessary. The idea is to include a cavity to the protocols. With the cavity a moderate optical depth is needed in order to get efficiency close to unity.

In this thesis three optical quantum memory protocols are considered: transverse/longitudal CRIB and AFC. A theoretical investigation by simulations of the Maxwell-bloch equations compares the different properties of these protocols. Moreover two different theoretical approaches to explain recent experimental results concerning a rare-earth-ion-doped crystal inside a cavity is derived and investigated. And finally a new scheme to improve the sharpness of the edges of a spectral hole is demonstrated.

Part II
Populärvetenskaplig sammanfattning

En vanlig dator är uppbyggd av ett antal komponenter. En viktig komponent i en vanlig dator är minnet. Informationen inuti en vanlig dator består av bitar, som antingen kan ha värdena 0 eller 1. Minnets uppgift är att lagra bitar under en viss tid, samt skicka informationen vidare till en annan komponent när det behövs.
En kvantdator är en ny typ av dator som potentiellt har förmågan att för vissa problem vara mycket snabbare än en vanlig dator. Kvantdatorn behöver ett minne, precis som en vanlig dator. Men för att en kvantdator ska kunna fungera behövs ett nytt typ av minne som kallas kvantminne. Kvantinformationen inuti en kvantdator består av kvantbitar. Kvantbitar kan inte bara ha värdena 0 eller 1, utan också ett "kanske-tillstånd". Det är bland annat tack vare detta "kanske-tillstånd" som en kvantdator kan bli bättre än en klassisk dator. Kvantminnets uppgift är mycket likt ett klassiskt minne. Uppgiften är att lagra kvantbitar under en viss tid, samt skicka kvantinformationen vidare till en annan komponent när det behövs.

På Atomfysikavdelning inom Lunds universitet försöker man utveckla ett optiskt kvantminne. Tanken med detta optiska kvantminne är att spara ljus inuti en kristall under en viss tid och efter ett tag skicka ut ljuset igen. Det inkommande ljuset innehåller kvantinformation, och denna information får ej förstöras inuti kristallen. Kristallen som utgör kvantminnet består av bland annat joner ifrån sällsynta jordartsmetaller. Dessa joner har speciella egenskaper som gör det möjligt att kvantinformationen inte förstörs. Det är viktigt att ett kvantminne har hög effektivtet så att den mesta kvantinformationen som sparas i minnet kan skickas ut igen.

Denna uppsats handlar om att teoretiskt undersöka olika hög-effektiva optiska kvantminnen. Uppsatsen är indelad i tre olika delar. I varje del så tas formler fram som beskriver kristallens växelverkan med det ljus som ska sparas. Dessa formler är i många fall för komplicerade att lösa för hand. Av denna anledningen så simulerar man formlerna i en vanlig dator. Med hjälp av resultaten ifrån datorn kan man förutsäga vad som kommer att ske i verkligheten.
I första delen undersöks några olika typer av protokoll som finns till kvantminnen. Det finns i huvudsak tre olika protokoll av optiska kvantminnen för de kristaller som används. De olika protokollens för- samt nackdelar jämförs med hjälp av de resultat som simuleringarna ger.
I andra delen tas en modell fram med för att förklara nya experimentella resultat där man har satt två speglar runt en kristall. Speglarna är inga vanliga speglar utan de är halvt genomskinliga vilket skapar underliga effekter inuti kristallen. Dessa effekter kan förklaras med hjälp av den modell som tas fram och de simulerade resultaten matchas mot de experimentella värdena.
I tredje och sista delen så tas ett nytt koncept fram för att i framtiden förbättra kvaliten av kvantminnen baserade på en viss typ av kristall. Detta konceptet förklaras i detalj, dessutom så bevisas det att den fungerar i teorin.

Part III
Introduction

1. BACKGROUND

Quantum information science is a new and rapidly developing field. Quantum cryptography is one application inside this field that uses quantum mechanics to theoretically guarantee secure communication [1]. A lot of exciting challenges remains in order to realize quantum cryptography to its full potential in practise. One problem is that long-distance quantum communication needs some sort of quantum repeater. With a quantum repeater it will be possible to send quantum information around the globe. A quantum repeater has three main requirements in order to be realized [2]:

- Distribution of entanglement
- Entanglement swapping
- Quantum memory

In this thesis the focus will be on the quantum memory. A quantum memory is very similar to a classical memory in the sense that it should be able to reliably store and on-demand release information. The difference is that a quantum memory should be able to handle quantum information. A lot of theoretical proposals as well as experimental realizations for a quantum memory has been done. Controlled Reversible Inhomogeneous Broadening (CRIB) first proposed by Moiseev and Kröll in 2001 [3] is one example of a quantum memory scheme. A variation of the CRIB protocol was experimentally proven to obtain well over 60% efficiency by Hedges et. al. in 2010 [4]. Another interesting quantum memory scheme is the Atomic Frequency Comb (AFC), it was introduced by Afzelius et. al. in 2008 [5]. Experimental results of 35% efficiency was shown by Amari et. al. in the beginning of 2010 [6]. Recently in Lund at the Quantum information group, a quantum memory based on the AFC protocol together with a cavity has been realized experimentally [7]. The fusion between the AFC protocol together with a cavity has been shown theoretically to give efficiency close to unity given that the cavity is on resonance [8]. In this thesis a theoretical investigation of both the CRIB and the AFC scheme with and without a cavity is done as well as improvements and suggestions around this topic.

2. PROBLEM STATEMENT AND PURPOSE

This thesis is divided into three different problems:

1. Understanding the advantages and disadvantages of the CRIB and the AFC quantum memory protocols is vital in order to create a high efficiency quantum memory in practise. The analytical treatment of the quantum memory protocols are often simplified with respect to the shape of the absorption profile in order to get an analytical solution. The problem is that the experimental setup isn't always as simple as the parameters used in the analytical treatment. One way to extend the analytical treatment is to use numerical simulations with more complex input parameters.
   The purpose of this part is to learn more about the differences of the CRIB and the AFC quantum memory protocols, compare their advantages and disadvantages and also see how the shape of the absorption profile effects the efficiency by numerical simulations.

2. New experimental result has been obtained at the Quantum information group in Lund considering a quantum memory realized with a rare-earth-ion-doped crystal inside a cavity [7]. The goal of the experiment was to get a high efficiency quantum memory. The theoretical motivation for this kind of experiment, with certain approximations, was made by Mikael Afzelius and Christoph Simon [8]. But the experimental results where not the expected and a model to understand the results is needed. For example some approximations made in the previous theoretical investigation might not hold for this type of experimental setup.
   The purpose of this part is to create a model that can explain the experimental results. Predictions and recommendations can then be made of how to change the experimental setup in order to get a high efficienct quantum memory.

3. Creating a spectral hole in the inhomogenous profile is a key concept for many applications. Both the CRIB and the AFC scheme relies on the fact that there is one or several narrow peak(s) in the absorption profile. Near the peak(s) (in the frequency-domain) there should be ideally no absorbing ions in order to get a high efficienct quantum memory. Thus there is a need to get as sharp structures as possible inside the inhomogenous profile.
   The purpose of this part is to investigate if improvements can be made to the current hole burning procedure in the inhomogenous profile in order to get more sharper structures.

3. STRUCTURE OF THIS THESIS

This thesis has seven different parts.

- The first and the second part is an introduction to quantum mechanics and the quantum repeater.

- The third part is a theoretical derivation of the well-known Maxwell-Bloch equations (MB) for a 2-level system. This model is a semiclassical model that treats the atoms quantum mechanically and the light classically by Maxwell's wave equation.

- The fourth part uses the MB equations in order to simulate the CRIB and AFC protocols, this part will investigate point 1 in "Problem statement and purpose".

- The fifth and the sixth part of this thesis concerns point 2 in "Problem statement and purpose" where a rare-earth-ion-doped crystal inside a cavity is modelled in two different ways. The first model is a simple model that sums all round-trips inside a cavity given a certain absorption profile. The second model is more advanced and it's basically an extension to the MB equations, whereas the quantum memory efficiency can be tested.

- The last part concerns point 3 in "Problem statement and purpose" where a scheme that improves the sharpness of the edges of a spectral hole. A proof-of-concept is made with a simplified model containing the MB-equations.

Part IV
Quantum mechanics

4. THE DENSITY OPERATOR

The density operator is a vital operator in order to describe an ensemble of atoms. This operator will be the ground-stone in the quantum mechanical postulate defined in Section 5. In the following the definition of the density operator will be stated.

Definition 4.1. *The density operator ρ can be defined from the spectral decomposition*

$$\rho \equiv \sum_{i=0}^{n} p_i |\psi_i\rangle\langle\psi_i| \tag{1}$$

with the conditions that $\sum_{i=0}^{n} p_i = 1$ and $|\psi_i\rangle$ are normalized state vectors in some Hilbert space.

Theorem 4.1. *An operator ρ is the density operator associated to some ensemble, iff it satisfies the conditions:*
(1) ρ has trace equal to one.
(2) ρ is a Hermitian positive-semidefinite matrix.

Proof in [9], page 101. □

5. POSTULATES

To understand quantum mechanics it is vital to understand the postulates of quantum mechanics. There are four postulates that are the building blocks of quantum mechanics and everything else in quantum mechanics are consequences of these statements. The postulates will be stated in this section and they will be explained a little.

Postulate I
A closed physical system is a projective Hilbert space $\mathcal{H}$ that is called the state space. The physical states of the system are represented as density operators on a state space. Given a state $|\psi\rangle \in \mathcal{H}$ the corresponding density operator is

$$\rho := |\psi\rangle\langle\psi| \tag{2}$$

Postulate II
The evolution of the closed quantum system from time t_0 to time t_1 is described by a unitary transformation. This means that there exists a unitary operator U that is unique up to a phase factor that connects a state $\rho(t_0)$ to $\rho(t_1)$ by

$$\rho(t_1) = U\rho(t_0)U^\dagger \tag{3}$$

Postulate III
Quantum measurements on $\mathcal{H}$ whose state are represented as ρ are specified by a Hermitian operator

$O = \sum_x xP_x$ called an observable. The probability of observing an outcome x is

$$P_X(x) = Tr(P_x\rho) \tag{4}$$

given a certain outcome x the resulting density operator is

$$\rho' = \frac{1}{P_X(x)} P_x \rho P_x \tag{5}$$

Postulate IV
Compostion of two state spaces $\mathcal{H}_A$ and $\mathcal{H}_B$ is isomorphic to $\mathcal{H}_A \otimes \mathcal{H}_B$. For two independent density operators ρ_A from $\mathcal{H}_A$ and ρ_B from $\mathcal{H}_B$ the joint state becomes

$$\rho_{AB} = \rho_A \otimes \rho_B \tag{6}$$

The first postulate sets up the world that the states live in. As can be seen the postulates describes a closed physical system. Now what system is closed? Probably the only system that is closed is the universe itself. When a model is built to explain some experiment, care has to be taken since the experiments are not closed systems.
The second postulate says how the density operator changes between two times. The key here is unitary operators, hence unitary operators are very important (unitary operators preserves the normalization in order to interpret different outcomes a probability). This postulate is equilvalent to the Schrödinger equation,

$$i\hbar \frac{d|\psi\rangle}{dt} = H|\psi\rangle \tag{7}$$

The time evolution of a state of a closed system is described by the Schrödinger equation where H is a Hermitian operator called the Hamiltonian.
The third postulate tells us how to measure a state. Note that when a measurement has been performed the density operator is instantely changed. A useful expression for the expectation value of an observable can be calculated by

$$\langle O \rangle = \sum_x xP_X(x) = \sum_x xTr(P_x\rho) = Tr(\sum_x xP_x\rho) = Tr(O\rho) \tag{8}$$

From this postulate the famous Heisenberg uncertainty principle can be derived. The uncertainty principle states that for example an arbitrary accuracy can't be obtained for the position and momentum of an electron simultaneously.
The last postulate tells us how to composite two state spaces. The tensor product is important in order to build a quantum computer of more than one qubit ([9], p. 80-96; [10], p. 30-32).

6. THE QUBIT

A classical computer have bits to represent information. A bit is like a flash light, either it is turned on or off. This way a base 2 system is made up to store values. So what is different in qubits? The answer is that the qubit does not only hold on or off, it also holds a quantum superposition. The quantum superposition is used when multiple qubits are in use, for instance a pair of qubits can be in four states and three qubits in eight different states. The important thing is that the 2^n states can be hold at the same time in a quantum computer but a classical computer

can only hold one of 2^n states at one time.
A single qubit is represented by the following notation

$$|\psi\rangle = \alpha|0\rangle + \beta|1\rangle \tag{9}$$

the corresponding density operator is

$$\rho = |\psi\rangle\langle\psi| = |\alpha|^2|0\rangle\langle 0| + \alpha\beta^*|0\rangle\langle 1| + \alpha^*\beta|1\rangle\langle 0| + |\beta|^2|1\rangle\langle 1| \tag{10}$$

The $|0\rangle$ and $|1\rangle$ can for example be the two different states an electron can have (spin up and spin down).
The state-vector can be seen as a vector:

$$|\psi\rangle = \begin{pmatrix}\alpha\\0\end{pmatrix} + \begin{pmatrix}0\\\beta\end{pmatrix} = \begin{pmatrix}\alpha\\\beta\end{pmatrix} \tag{11}$$

The state set $\{|0\rangle, |1\rangle\}$ can be seen as an orthonormal basis that spans a 2-dimensional vector space. The density operator in this representation will then be a 2x2 matrix (the density operator is called the density matrix due to this reason, in this thesis no difference is made between the density operator and the density matrix):

$$\rho = \begin{pmatrix}\alpha\\\beta\end{pmatrix}\begin{pmatrix}\alpha^* & \beta^*\end{pmatrix} = \begin{pmatrix}|\alpha|^2 & \alpha\beta^*\\\alpha^*\beta & |\beta|^2\end{pmatrix} \tag{12}$$

α and β in Eq. (9) are complex numbers and the probability to measure the zero-state is $|\alpha|^2$ and the probability to measure the one-state is $|\beta|^2$. Note that these are the diagonal elements of the density matrix. This can be expressed as

$$\{\ |\alpha|^2 + |\beta|^2 = 1 \quad \Leftrightarrow \begin{cases}\alpha = e^{i\gamma}sin(\frac{\theta}{2})\\\beta = e^{i\gamma}e^{i\varphi}cos(\frac{\theta}{2})\end{cases} \tag{13}$$

Note that the convention of α and β is chosen differently compared to for example Wikipedia: [11].
Given Eq. (13) we can write Eq. (9) as

$$|\psi\rangle = e^{i\gamma}(sin\left(\frac{\theta}{2}\right)|0\rangle + e^{i\varphi}cos\left(\frac{\theta}{2}\right)|1\rangle) \tag{14}$$

The $e^{i\gamma}$-term in Eq. (14) is taken away, the equation to represent the state is then as follows.

$$|\psi\rangle = sin(\frac{\theta}{2})|0\rangle + e^{i\varphi}cos(\frac{\theta}{2})|1\rangle \tag{15}$$

The reason to remove the $e^{i\gamma}$-term is because it won't return any physics. This can be understood by looking at the density operator of Eq. (14),

$$\rho = \begin{pmatrix}sin(\frac{\theta}{2})^2 & e^{-i\varphi}cos(\frac{\theta}{2})sin(\frac{\theta}{2})\\e^{i\varphi}cos(\frac{\theta}{2})sin(\frac{\theta}{2}) & cos(\frac{\theta}{2})^2\end{pmatrix} \tag{16}$$

the term $e^{i\gamma}$ has been multiplied by its complex conjugate. Since the density matrix contains all physics that can be seen from an observer there is no loss in removing it. Eq. (15) can be visualized as a point in the *Bloch sphere* of a single qubit (for the more general case see Theorem 8.2, there is also the possibility to be inside the sphere). To visualize quantum mechanics is always a good

idea since quantum mechanics is not always intuitive (classic mechanics is more understandable for humans since we live in the "big world"). But when studying atomic physics I learned to see the world though the eyes of a child. Figure 1 are visualizing the θ and φ as degrees on *Bloch sphere*, the degrees are real numbers. The *Bloch vector* is the vector with initial point in origo and terminal point to a certain state in the *Bloch sphere*. In Figure 1 the *Bloch vector* has a length equal to one.

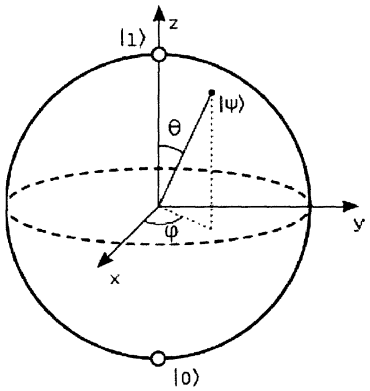

FIG. 1: The Bloch sphere. Image taken from [11]. The groundstate is now chosen to be at $z = -1$ instead of $z = 1$ as in [11].

7. MULTIPLE QUBITS

In the following an example with two qubits are shown. When two classical bits are represented they have four possible states 00, 01, 10 and 11. The qubits has what is called four computational basis states $|0\rangle \otimes |0\rangle := |00\rangle$, $|0\rangle \otimes |1\rangle := |01\rangle$, $|1\rangle \otimes |0\rangle := |10\rangle$ and $|1\rangle \otimes |1\rangle := |11\rangle$. This will give the superposition the following equation

$$|\psi\rangle = \alpha_{00}|00\rangle + \alpha_{01}|01\rangle + \alpha_{10}|10\rangle + \alpha_{11}|11\rangle = \begin{pmatrix} \alpha_{00} \\ \alpha_{01} \\ \alpha_{10} \\ \alpha_{11} \end{pmatrix} \tag{17}$$

The set $\{|00\rangle, |01\rangle, |10\rangle, |11\rangle\}$ can be seen as an orthonormal basis that spans a 4-dimensional vector space. The new basis vectors are obtained by calculating the tensor product between the basis vectors of two single qubits. Postulate IV states how to composite two state spaces in terms of the density operator. For Eq. (17) the corresponding density operator is (the density matrix will be of size 4x4, this matrix will not be stated)

$$\rho = |\psi\rangle\langle\psi| \tag{18}$$

If there are two qubits in two different states we can calculate the tensor product between them to get the Eq. (17) like this.

$$\begin{aligned} |\psi\rangle &= \alpha_1|0\rangle + \beta_1|1\rangle \\ |\phi\rangle &= \alpha_2|0\rangle + \beta_2|1\rangle \\ |\psi\rangle \otimes |\phi\rangle &= (\alpha_1|0\rangle + \beta_1|1\rangle) \otimes (\alpha_2|0\rangle + \beta_2|1\rangle) \\ &= \alpha_1\alpha_2|00\rangle + \alpha_1\beta_2|01\rangle + \beta_1\alpha_2|10\rangle + \beta_1\beta_2|11\rangle \end{aligned}$$

In analogy with the single qubit, the sum of the absolute value square of the coefficients is equal to one.

$$|\alpha_{00}|^2 + |\alpha_{01}|^2 + |\alpha_{10}|^2 + |\alpha_{11}|^2 = 1 \tag{19}$$

This can be generalized to an arbitrary number of qubits. To understand how much better the quantum computer potentially can be is to set the number of qubit to for instance $n = 500$, then 2^n would be a larger value than the estimated number of atoms in the observable universe. To store all these complex numbers is of course not possible by a classical computer. But as the quantum world is opening more and more for human, the possibilities are greater than we every can imagine ([9], p. 16-17).

8. PURE AND MIXED STATES

A pure state is a state that can be represented by a state vector, it means that the state is known exactly. For a single qubit the quantum state can be expressed as in Eq. (9). When the state vector isn't enough to describe a quantum state the density operator is used. A pure state can also be represented by the density operator and hence the density operator is a generalization of the state vector. For a pure state the density operator looks like

$$\rho = |\psi\rangle\langle\psi| \tag{20}$$

where $|\psi\rangle$ is exactly known.
The denisty operator representation for a mixed state is a mixture of pure states. The mixed state can in particular represent an ensemble of atoms, this will be used later in this thesis when deriving the *Bloch equations*. When solving the *Bloch equations* numerically, space will be discretized. Every discretized point in space contains a lot of atoms in reality. If every discretized point would be represented by a state vector (a pure state) then the model assumes that there is only one atom in every discretized point. Using the density operator instead will be a better approximation to reality since now every discretized point can be described by an ensemble of atoms.
The opposite of a pure state is a completely mixed state ([12], p. 111). The completely mixed state is represented by the density matrix as

$$\rho = \frac{1}{n}\mathcal{I} \tag{21}$$

where n is the dimension of the state space and $\mathcal{I}$ is the identity matrix of dimension n x n.
For example when a single qubit is used the opposite of a pure state is $\rho = \frac{1}{2}\mathcal{I} = \frac{1}{2}(|0\rangle\langle 0| + |1\rangle\langle 1|)$.
Two useful theorems will be stated and proved. The second theorem is important in order to derive the *Bloch equations*.

Theorem 8.1. *Let ρ be a density operator, then the following holds*

$$Tr(\rho^k) \leqslant 1 \tag{22}$$

where $k \geqslant 2$ is an integer, with equality iff ρ is in a pure state.

Proof. In Theorem 4.1 the second condition is that ρ is Hermitian (this means that the density matrix is normal, which leads us to use Theorem 12.5 in [13]). It says that a matrix can be diagonalized by a unitary matrix with the eigenvalues on the diagonal iff the matrix is normal (that is $\rho = UDU^\dagger$ for some unitary matrix U and diagonal matrix D). Lets look at the trace for one single density operator, and since it is Hermitian all eigenvalues are real (so the diagonal element of D are all real).

$$Tr(\rho) = Tr(UDU^\dagger) = Tr(UU^\dagger D) = Tr(\mathcal{I}D) = Tr(D) = 1 \tag{23}$$

The trace is one according to the first condition in Theorem 4.1. This means that any element in D is less or equal to one. Now lets look at the density operator to the power k.

$$Tr(\rho^k) = Tr(UDU^\dagger UDU^\dagger UDU^\dagger ... UDU^\dagger) = Tr(UD^kU^\dagger) = Tr(D^k) \tag{24}$$

Since any element d_i in D is less or equal to one.

$$Tr(D^k) = \sum_{i=1}^{n} d_i^k \leqslant 1 \tag{25}$$

For a pure state the trace is

$$Tr(\rho^k) = Tr(|\psi\rangle\langle\psi|\psi\rangle\langle\psi|...|\psi\rangle\langle\psi|) = Tr(|\psi\rangle\langle\psi|) = Tr(\rho) = 1 \tag{26}$$

Conversely suppose

$$Tr(\rho^k) = Tr(D^k) = 1 \tag{27}$$

for an arbitrary density matrix ρ, then according to Eq. (25) the diagonal elements d_i is less or equal to one. If there exists one element equal to one it implies that it comes from a pure state. And if d_i is less than one, then k must be equal to one to fulfil Eq. (27) and therefore ρ must be a pure state. □

Theorem 8.2. *An arbitrary density matrix for a mixed state of one qubit can be written as*

$$\rho = \frac{1}{2}\begin{pmatrix} 1 - r_z & r_x + ir_y \\ r_x - ir_y & 1 + r_z \end{pmatrix} \tag{28}$$

where $\vec{r} = (r_x, r_y, r_z)$ is a real vector that is called the Bloch vector and $||\vec{r}|| \leqslant 1$, with equality iff ρ is a pure state.

Proof. For a single qubit the density matrix is of size 2x2.

$$\rho = \begin{pmatrix} a & b \\ c & d \end{pmatrix} \tag{29}$$

Lets start with the conditions in Theorem 4.1 and see what that gives for conditions on the values of the matrix ρ.

Hermitian:

$$\rho = \rho^\dagger = \begin{pmatrix} a & b \\ c & d \end{pmatrix} = \begin{pmatrix} a^* & c^* \\ b^* & d^* \end{pmatrix} \tag{30}$$

So a and d must be real. And c and b are connected as:

$$b = g - ih \tag{31}$$
$$c = g + ih \tag{32}$$

where h and g are real.
Trace of ρ must be one which gives $a+d = 1$.
ρ must be positive semi-definite $\Leftrightarrow$ $\lambda \geq 0$ ([13], p. 124). By calculating the characteristic polynomial and get the eigenvalues of ρ this condition can be used.

$$\det(\rho - \lambda\mathcal{I}) = \begin{vmatrix} a-\lambda & g-ih \\ g+ih & 1-a-\lambda \end{vmatrix} = \lambda^2 - \lambda + x = 0 \tag{33}$$

where $x = a - a^2 - g^2 - h^2$.
This gives the eigenvalues

$$\lambda_1 = \frac{1}{2} + \sqrt{\frac{1}{4} - x} \tag{34}$$
$$\lambda_2 = \frac{1}{2} - \sqrt{\frac{1}{4} - x} \tag{35}$$

And now applying the condition $\lambda \geq 0$

$$\frac{1}{2} - \sqrt{\frac{1}{4} - x} \geq 0 \Longleftrightarrow x \geq 0 \tag{36}$$

The density matrix that is stated in the theorem will be set equal to Eq. (30)

$$\rho = \frac{1}{2}\begin{pmatrix} 1-r_z & r_x + ir_y \\ r_x - ir_y & 1+r_z \end{pmatrix} = \begin{pmatrix} a & b \\ c & d \end{pmatrix} \tag{37}$$

This gives $a = \dfrac{1-r_z}{2}$, $g = r_x/2$ and $h = -r_y/2$. Inserting this into Eq. (36) with $x = a - a^2 - g^2 - h^2$, the condition we wanted is obtained:

$$r_x^2 + r_y^2 + r_z^2 \leq 1 \tag{38}$$

The first part of the proof is done.

The density matrix for a single qubit pure state

$$\begin{aligned} \rho &= |\psi\rangle\langle\psi| \\ &= (\alpha|0\rangle + \beta|1\rangle)(\alpha^*\langle 0| + \beta^*\langle 1|) \\ &= \alpha\alpha^*|0\rangle\langle 0| + \alpha\beta^*|0\rangle\langle 1| + \beta\alpha^*|1\rangle\langle 0| + \beta\beta^*|1\rangle\langle 1| \end{aligned} \tag{39}$$

And in matrix form

$$\rho = \begin{pmatrix} \alpha\alpha^* & \alpha\beta^* \\ \beta\alpha^* & \beta\beta^* \end{pmatrix} \tag{40}$$

Which gives the following equation-system:

$$\begin{cases} \alpha\alpha^* = \frac{1}{2}(1 - r_z) \\ \beta\beta^* = \frac{1}{2}(1 + r_z) \\ \alpha\beta^* = \frac{1}{2}(r_x + ir_y) \\ \beta\alpha^* = \frac{1}{2}(r_x - ir_y) \end{cases} \Leftrightarrow \begin{cases} \alpha\alpha^* + \beta\beta^* = \frac{1}{2}(1 - r_z + 1 + r_z) = 1 \\ \alpha\alpha^* - \beta\beta^* = \frac{1}{2}(1 - r_z - (1 + r_z)) = -r_z \\ \alpha\beta^* + \beta\alpha^* = r_x \\ i(\alpha\beta^* - \beta\alpha^*) = i(-ir_y) = r_y \end{cases}$$

Lets look at the three last equations and use Eq. (16),

$$\begin{cases} \alpha\alpha^* - \beta\beta^* = sin^2(\frac{\theta}{2}) - cos^2(\frac{\theta}{2}) = -cos(\theta) = -r_z \\ \alpha\beta^* + \beta\alpha^* = e^{-i\varphi}sin(\theta)/2 + e^{i\varphi}sin(\theta)/2 = cos(\varphi)sin(\theta) = r_x \\ i(\alpha\beta^* - \beta\alpha^*) = i(e^{-i\varphi}sin(\theta)/2 - e^{i\varphi}sin(\theta)/2) = sin(\varphi)sin(\theta) = r_y \end{cases} \Leftrightarrow$$

$$\begin{cases} r_x = cos(\varphi)sin(\theta) \\ r_y = sin(\varphi)sin(\theta) \\ r_z = cos(\theta) \end{cases}$$

The above equation is called spherical coordinates with the radius one ([14], p. 27), this gives $||\overrightarrow{r}|| = 1$ and hence a pure state has *Bloch vector* length equal to one.
Conversely, suppose $||\overrightarrow{r}|| = 1$. Theorem 8.1 says that $Tr(\rho^k) = 1$ iff ρ is in a pure state where $k \geqslant 2$, and in particular this is true for $k = 2$. Using $Tr(\rho^2)$ for the density matrix that is stated in the theorem given that $||\overrightarrow{r}|| = 1$

$$Tr(\rho^2) = \frac{1}{4}((1 - r_z)^2 + 2r_x^2 + 2r_y^2 + (1 + r_z)^2) = \frac{1}{4}(2 + 2\,||\overrightarrow{r}||) = 1 \tag{41}$$

Hence according to Theorem 8.1 the density matrix ρ is pure. □

9. TIME EVOLUTION OF THE DENSITY OPERATOR

For a state vector the time evolution is described by Eq. (7). In the following the time evolution for the density operator will be derived:

$$\frac{d}{dt}\rho(t) = \frac{d}{dt}\sum_{i=0}^{n} p_i|\psi_i(t)\rangle\langle\psi_i(t)| \tag{42}$$

$$= \sum_{i=0}^{n}(p_i(\frac{d}{dt}|\psi_i(t)\rangle)\langle\psi_i(t)| + p_i|\psi_i(t)\rangle(\frac{d}{dt}\langle\psi_i(t)|)) \tag{43}$$

$$= \sum_{i=0}^{n}(p_i(\frac{1}{i\hbar}H|\psi_i(t)\rangle)\langle\psi_i(t)| + p_i|\psi_i(t)\rangle(-\frac{1}{i\hbar}\langle\psi_i(t)|H)) \tag{44}$$

$$= \frac{1}{i\hbar}H\sum_{i=0}^{n} p_i|\psi_i(t)\rangle\langle\psi_i(t)| - \frac{1}{i\hbar}\sum_{i=0}^{n} p_i|\psi_i(t)\rangle\langle\psi_i(t)|H \tag{45}$$

$$= \frac{1}{i\hbar}[H, \rho(t)] \tag{46}$$

The equation above will be used in the derivation of the *Bloch equations.*

Part V
The Quantum repeater

10. SCALING ERRORS IN QUANTUM COMMUNICATION

The most common way to send quantum information is to send photons through an optical fiber. The information can be encoded in the two-dimensional basis consisting of horizontal respective vertical polarization of single photons. In an ideal world it would be possible to send quantum information over very large distances. But in reality there are for example imperfections in the optical fibers and detector noise that creates errors. It turns out that the probability of absorption and depolarization of a photon in an optical fiber scales exponentially with the distance. This introduces three complications:

1. The number of trials that is needed to transmit a photon grows exponentially with the length of the fiber.

2. Imperfections in the detector can give dark counts (a dark count is when the detector registers that a photon is detected, but in reality nothing came in to the detector). This implies that the rate of the real photons reaching the detector must be higher than the dark count rate otherwise the signal-to-noise drops to zero [1].

3. Even if a photon is successfully transmitted, the fidelity between the inital quantum state and the received quantum state decreases exponentially with the length of the fiber (fidelity is a measure of how similar two quantum states are [9]).

The mission of a quantum repeater is to improve the scaling of errors with respect to the length. This will enable long-distance quantum communication [15].

11. DEMONSTRATION OF HOW A QUANTUM REPEATER WORKS

The goal of the quantum repeater is to create entanglement between two parties called *Alice* (A) and *Bob* (B) where A and B are spatially separated. Entanglement is a property of quantum states that has no analogue in classical mechanics. Since there is no classical analogue the phenomena is very unintuitive. Even so it has been experimentally shown to be a property of nature. Entanglement is a key-stone in for example Quantum Key Distribution (QKD) that enables secure communication between two parties. If any third party tries to measure the communication sent between the two parties the state will collapse. The third party can then be detected with some probability [9].
In Figure 2 an illustration of how a basic setup for QKD looks like. A source in the middle sends out two entangled photons through for example an optical fiber. One photon is sent to Alice and one to Bob. The distance between them is d. As mentioned before the number of trials scales exponentially with the distance, hence the distance d is limited. It's at this point the quantum repeater comes into play.
In order to for example double the distance between Alice and Bob a quantum measurement device is put in the middle (can be seen in Figure 3). There are now two sources that sends out entangled particles. The source to the left sends out two entangled photons, one photon to Alice and one photon to the quantum measurement device. The source to the right sends out two entangled photons, one photon to Bob and one photon to the quantum measurement device. Inside the quantum measurement device *entanglement swapping* is peformed. This makes the two photons inside the

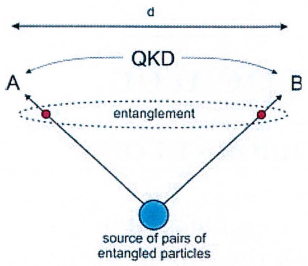

FIG. 2: Illustration of the setup for QKD. Image from [16].

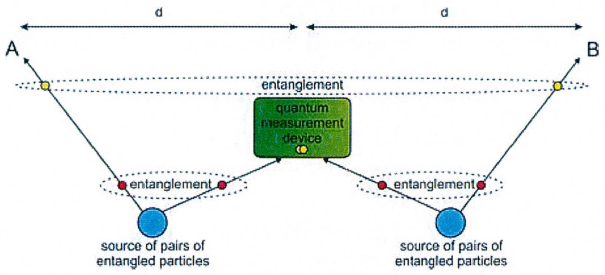

FIG. 3: Illustration of the setup together with a quantum measurement device that performs entanglement swapping. Image from [16].

device to dis-entangle with their respectively photon and instead the photon that Alice has becomes entangled with Bobs photon [17]. At this point the quantum repeater scheme has created entanglement between Alice and Bob with a distance of $2d$ between the parties. This concept can now be generalized by building a chain of quantum repeaters shown in Figure 4. Notice that a quantum memory is also introduced in this figure. The purpose of having a quantum memory in this scheme is to get better performance [16].

Although the question remains: has the scaling problem been reduced?

To be able to answer this question a small investigation of the QBER (Quantum Bit Error Rate) will be done. The QBER is defined as the ratio between the the wrong number of bits and the total number of bits received ($QBER = P_{det}/(P_{det} + P_{raw})$, where P_{raw} is the probability to get a correct bit and P_{det} is the probability to get an error). The probability of getting a correct bit is calculated to be: $P_{raw} = t_{link}\eta^n$, where t_{link} is the transmission coefficient (the probability that a sent photon gets to the wanted detector given the total distance), η is the detector efficiency and n is the number of sections of length d. The probability to get an error is calculated to be: $P_{det} = (t_{link}^{1/n}\eta + (1 - t_{link}^{1/n})p_{dark})^n - t_{link}\eta^{1/n}$, where p_{dark} is the probability to get a dark count.

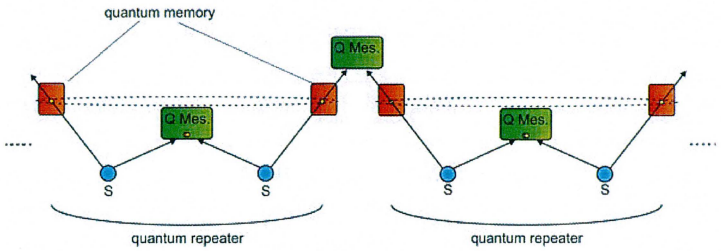

FIG. 4: Illustration how a quantum repeater enables to create entangled photon to an arbitrary distance. Image from [16].

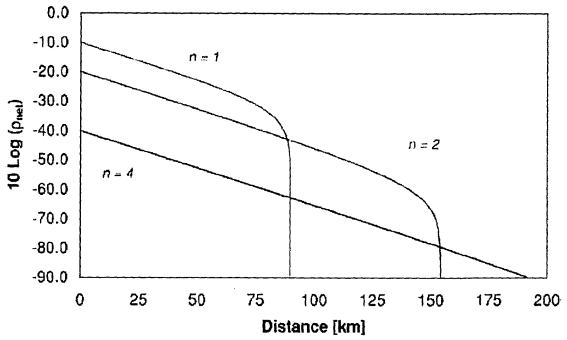

FIG. 5: Three different n is shown. The parameters are set to: $\eta = 10\%$, $p_{dark} = 10^{-4}$ and fiber attenuation $\alpha = 0.25dB/km$. Image from [1].

Finally the normalized net rate (the number of succesfully transmitted photons over a period of time) is $\rho_{net} = (P_{raw} + P_{det}) \cdot fct(QBER)$, where the function fct denotes the fraction of bits remaining after error correction and privacy amplification. For a more detailed description see ([1], p.20-21). In Figure 5 an example of ρ_{net} is plotted as a function of the distance. Three different n is shown. The parameters are set to: $\eta = 10\%$, $p_{dark} = 10^{-4}$ and fiber attenuation $\alpha = 0.25dB/km$. As can be seen when $n = 1$ the net rate drops to zero at $90km$, while for $n = 2$ the net rate drops to zero at $155km$. The reason for a much lower net rate for several quantum repeaters is because the detector efficiency is set to a low value ($\eta = 10\%$).

Part VI
The Maxwell-Bloch equations for a 2-level system

The Maxwell-Bloch equations is a model that describes light-matter interaction. The model is simplified so that numerical simulations is possible with only three nested loops. The equations is called Maxwell-Bloch since the atoms are treated quantum mechanically by the Bloch equations while the light is treated by the Maxwell's wave equation.

12. DERIVATION OF THE BLOCH EQUATIONS

Starting of from Eq. (46) (the density matrix will always be time-dependent in this section therefore $\rho := \rho(t)$) the Hamiltonian needs to be defined in order to describe the physics. In this case there are only two energy-levels. The groundstate denoted as $|g\rangle$ with eigenvalue $\hbar\omega_g$ and the excited state denoted as $|e\rangle$ with eigenvalue $\hbar\omega_e$ The Hamiltonian has two parts

$$H = H_0 + H_I(t) \tag{47}$$

where H_0 is the Hamiltonian for an unperturbed atom and $H_I(t)$ is a time-dependent perturbation. The unperturbed Hamiltonian described as

$$H_0 = \hbar\omega_0 |e\rangle\langle e| \tag{48}$$

where $\omega_0 = \omega_e - \omega_g$ is the transition frequency for the atom.
The time-dependent perturbation will be produced by a spatially 1-dimensional oscillating electric field $E(z,t)$. In the *dipole approximation* the perturbation can be described by

$$H_I(t) = -ME(z,t) = -(\mu_{ge}|g\rangle\langle e| + \mu_{ge}^*|e\rangle\langle g|)E(z,t) \tag{49}$$

where M is the dipole moment operator and $\mu_{ge} = -e\langle g|z|e\rangle$ is the transition dipole moment between ground state and the excited state. The electric field is described as

$$\begin{aligned} E(z,t) &= \xi(z,t)\cos(\omega_L t - kz + \varphi(t)) && (50)\\ &= \xi(z,t)(\cos(\omega_L t - kz)\cos\varphi(t) - \sin(\omega_L t - kz)\sin\varphi(t)) && (51) \end{aligned}$$

where $\xi(z,t)$ is the envelope of the field, k is the wavenumber, $\varphi(t)$ is the phase and ω_L is the laser frequency ([18]; [19], p. 8-14).
The *rotating wave approximation* (RWA) is an approximation that assumes that the radiation frequency is close to the atomic resonance:

$$|\Delta| = |\omega_0 - \omega_L| \ll \omega_0 \tag{52}$$

where Δ is called detuning.
This approximation will be used to simplify the equations. First of all we need to move from the Schrödinger picture into the interaction picture. This is done by the unitary operator

$$U = e^{-iH_0 t/\hbar} = \begin{bmatrix} 1 & 0 \\ 0 & e^{-i(w_0 t)} \end{bmatrix} \tag{53}$$

Thus the denisty matrix and Hamiltonian in this picture is $\rho' = U^{-1}\rho U$ resp. $H' = U^{-1}HU$. Note that for a unitary matrix the following holds $U^* = U^{-1}$. The time-evolution in this picture will now be derived. Lets start of by rewriting the time-evolution for the density matrix.

$$
\begin{aligned}
i\hbar\frac{d}{dt}\rho &= [H,\rho] && (54)\\
&= H\rho - \rho H && (55)\\
&= UU^{-1}HUU^{-1}\rho UU^{-1} - UU^{-1}\rho UU^{-1}HUU^{-1} && (56)\\
&= UH'\rho'U^{-1} - U\rho'H'U^{-1} && (57)\\
&= U(H'\rho' - \rho'H')U^{-1} && (58)\\
&\Leftrightarrow && (59)\\
i\hbar U^{-1}(\frac{d}{dt}\rho)U &= H'\rho' - \rho'H' && (60)\\
&= [H',\rho'] && (61)
\end{aligned}
$$

The left hand side of Eq. (54) will be written in terms of ρ'.

$$
\begin{aligned}
\frac{d}{dt}\rho &= \frac{d}{dt}(U\rho'U^{-1}) && (62)\\
&= (\frac{d}{dt}U)\rho'U^{-1} + U(\frac{d}{dt}\rho')U^{-1} + U\rho'(\frac{d}{dt}U^{-1}) && (63)
\end{aligned}
$$

Lets put the left hand side of Eq. (60) and Eq. (63) together

$$
\begin{aligned}
i\hbar U^{-1}(\frac{d}{dt}\rho)U &= i\hbar U^{-1}((\frac{d}{dt}U)\rho'U^{-1} + U(\frac{d}{dt}\rho')U^{-1} + U\rho'(\frac{d}{dt}U^{-1}))U && (64)\\
&= i\hbar(U^{-1}(\frac{d}{dt}U)\rho' + (\frac{d}{dt}\rho') + \rho'(\frac{d}{dt}U^{-1})U) && (65)
\end{aligned}
$$

And finally Eq. (65) is inserted into Eq. (61) and now the time-evolution becomes

$$
\begin{aligned}
i\hbar U^{-1}(\frac{d}{dt}\rho)U &= H'\rho' - \rho'H' && (66)\\
&\Leftrightarrow && (67)\\
i\hbar\frac{d}{dt}\rho' &= [H',\rho'] - i\hbar(U^{-1}(\frac{d}{dt}U)\rho' + \rho'(\frac{d}{dt}U^{-1})U) && (68)
\end{aligned}
$$

Note that

$$
U^{-1}(\frac{d}{dt}U) = \begin{bmatrix} 0 & 0 \\ 0 & -i\omega_0 \end{bmatrix} \quad (69)
$$

$$
(\frac{d}{dt}U^{-1})U = \begin{bmatrix} 0 & 0 \\ 0 & i\omega_0 \end{bmatrix} \quad (70)
$$

by introducing $G := i\hbar U^{-1}(\frac{d}{dt}U)$ and Eq. (68) can now be written as

$$
i\hbar\frac{d}{dt}\rho' = [H' - G, \rho'] \quad (71)
$$

H' will now be explicitly stated

$$H' = \hbar \begin{bmatrix} 0 & -\mu_{ge}E(z,t)e^{-i\omega_0 t}/\hbar \\ (-\mu_{ge}E(z,t)e^{-i\omega_0 t}/\hbar)^* & \omega_0 \end{bmatrix} \tag{72}$$

The off-diagonal terms will be further developed together with Eq. (51):

$$\begin{aligned} -\mu_{ge}E(z,t)e^{-i\omega_0 t}/\hbar &= -\mu_{ge}\xi(z,t)(\cos(\omega_L t - kz)\cos\varphi(t) - \sin(\omega_L t - kz)\sin\varphi(t))e^{-i\omega_0 t}/\hbar & (73)\\ &= -\frac{\mu_{ge}\xi(z,t)}{2\hbar}((e^{i(-kz+(\omega_L-\omega_0)t)} + e^{-i(-kz+(\omega_L+\omega_0)t)})\cos\varphi(t) & (74)\\ &\quad +i(e^{i(-kz+(\omega_L-\omega_0)t)} - e^{-i(-kz+(\omega_L+\omega_0)t)})\sin\varphi(t))) & (75) \end{aligned}$$

The RWA Eq. (52) will be used and neglect the fast oscillating term $e^{i(\omega_0+\omega_L)t}$. Moreover the real and imaginary Rabi frequencies will be introduced

$$\begin{aligned} \Omega_r &:= \Omega_r(t) = \frac{\mu_{ge}}{\hbar}\xi(z,t)\cos\varphi(t) & (76)\\ \Omega_i &:= \Omega_i(t) = \frac{\mu_{ge}}{\hbar}\xi(z,t)\sin\varphi(t) & (77) \end{aligned}$$

The electric field can then be written as

$$\begin{aligned} E(z,t) &= \frac{\hbar}{2\mu_{ge}}(\Omega_r\cos(\omega_L t - kz) - \Omega_i\sin(\omega_L t - kz)) & (78)\\ &= \frac{\hbar}{2\mu_{ge}}(e^{i(\omega_L t-kz)}(\Omega_r + i\Omega_i) + e^{-i(\omega_L t-kz)}(\Omega_r - i\Omega_i)) & (79) \end{aligned}$$

Now with the *rotating wave approximation* the Hamiltonian is denoted as H'_{RWA},

$$H'_{RWA} = \hbar \begin{bmatrix} 0 & -\frac{1}{2}(\Omega_r + i\Omega_i)e^{i(-kz-\Delta t)} \\ (-\frac{1}{2}(\Omega_r + i\Omega_i)e^{i(-kz-\Delta t)})^* & \omega_0 \end{bmatrix} \tag{80}$$

Also the global Hamiltonian in the interaction picture becomes

$$H'_{RWA} - G = \hbar \begin{bmatrix} 0 & -\frac{1}{2}(\Omega_r + i\Omega_i)e^{i(-kz-\Delta t)} \\ (-\frac{1}{2}(\Omega_r + i\Omega_i)e^{i(-kz-\Delta t)})^* & 0 \end{bmatrix} \tag{81}$$

A transformation back to the Schrödinger picture by applying the inverse of the unitary operator in Eq. (53) given the RWA will be done. Starting of from Eq. (66), but with the RWA

$$\begin{aligned} i\hbar U^{-1}(\frac{d}{dt}\rho)U &= H'_{RWA}\rho' - \rho' H'_{RWA} & (82)\\ i\hbar UU^{-1}(\frac{d}{dt}\rho)UU^{-1} &= UH'_{RWA}U^{-1}U\rho'U^{-1} - U\rho'U^{-1}UH'_{RWA}U^{-1} & (83)\\ i\hbar(\frac{d}{dt}\rho) &= UH'_{RWA}U^{-1}\rho - \rho UH'_{RWA}U^{-1} & (84) \end{aligned}$$

Now the Hamiltonian in the Schrödinger picture with the RWA is

$$H_{RWA} = UH'_{RWA}U^{-1} = \hbar \begin{bmatrix} 0 & -\frac{1}{2}(\Omega_r + i\Omega_i)e^{i(-kz+\omega_L t)} \\ (-\frac{1}{2}(\Omega_r + i\Omega_i)e^{i(-kz+\omega_L t)})^* & \omega_0 \end{bmatrix} \tag{85}$$

The last step is to change the rotating frame and use the frequency ω_L as reference frame. This is done by applying the unitary transformation R in the same manner as above but without going back to the original picture,

$$R = \begin{bmatrix} 1 & 0 \\ 0 & e^{-i(\omega_L t - kz)} \end{bmatrix} \tag{86}$$

Starting of from Eq. (68),

$$i\hbar \frac{d}{dt}\rho''(t) = [H''_{RWA}, \rho''(t)] - i\hbar(R^{-1}(\frac{d}{dt}R)\rho''(t) + \rho''(t)(\frac{d}{dt}R^{-1})R) \tag{87}$$

where $\rho''(t) = R^{-1}\rho R$ and $H''_{RWA}(t) = R^{-1}H_{RWA}(t)R$.
A similar expression is obtained for the additional terms on the right-hand side as above:

$$R^{-1}(\frac{d}{dt}R) = \begin{bmatrix} 0 & 0 \\ 0 & -i\omega_L \end{bmatrix} \tag{88}$$

$$(\frac{d}{dt}R^{-1})R = \begin{bmatrix} 0 & 0 \\ 0 & i\omega_L \end{bmatrix} \tag{89}$$

The global Hamiltonian H_{final} is then (with $G' = i\hbar R^{-1}(\frac{d}{dt}R)$):

$$H_{final} = H''_{RWA} - G' = \hbar \begin{bmatrix} 0 & -\frac{1}{2}(\Omega_r + i\Omega_i) \\ (-\frac{1}{2}(\Omega_r + i\Omega_i))^* & \omega_0 - \omega_L \end{bmatrix} \tag{90}$$

The Schrödinger equation can now be divided into 4 connected first order differential equations by looking at each term in the density matrix separately,

$$\rho_{final} = \begin{bmatrix} \rho_{gg} & \rho_{ge} \\ \rho^*_{ge} & \rho_{ee} \end{bmatrix} \tag{91}$$

$$i\hbar \frac{d}{dt}\rho_{final} = [H_{final}, \rho_{final}] \tag{92}$$

This is the result

$$\frac{d\rho_{gg}}{dt} = \frac{i}{2}((\Omega_r + i\Omega_i)\rho^*_{ge} - (\Omega_r - i\Omega_i)\rho_{ge}) \tag{93}$$

$$\frac{d\rho_{ge}}{dt} = i(\frac{1}{2}(\Omega_r + i\Omega_i)(\rho_{ee} - \rho_{gg}) + \rho_{ge}(\omega_0 - \omega_L)) \tag{94}$$

$$\frac{d\rho^*_{ge}}{dt} = i(\frac{1}{2}(\Omega_r - i\Omega_i)(\rho_{gg} - \rho_{ee}) - \rho^*_{ge}(\omega_0 - \omega_L)) \tag{95}$$

$$\frac{d\rho_{ee}}{dt} = \frac{i}{2}((\Omega_r - i\Omega_i)\rho_{ge} - (\Omega_r + i\Omega_i)\rho^*_{ge}) \tag{96}$$

The *Bloch equations* will now be stated in terms of the *Bloch vector* from Theorem 8.2.

$$\begin{cases} 2\rho_{gg} = 1 - r_z \\ 2\rho_{ge} = r_x + ir_y \\ 2\rho_{ee} = 1 + r_z \end{cases} \Leftrightarrow \begin{cases} r_x = 2Re(\rho_{ge}) \\ r_y = 2Im(\rho_{ge}) \\ r_z = \rho_{ee} - \rho_{gg} \end{cases} \tag{97}$$

In order to figure out how the equations will look with the *Bloch vector*, one intermediate calculation is done

$$\frac{d}{dt}(\rho_{ee} - \rho_{gg}) = i((\Omega_r - i\Omega_i)(Re(\rho_{ge}) + iIm(\rho_{ge})) - (\Omega_r + i\Omega_i)(Re(\rho_{ge}) - iIm(\rho_{ge}))) \quad (98)$$

$$\frac{d}{dt}(Re(\rho_{ge}) + iIm(\rho_{ge})) = i(\frac{1}{2}(\Omega_r + i\Omega_i)(\rho_{ee} - \rho_{gg}) + (Re(\rho_{ge}) + iIm(\rho_{ge}))(\omega_0 - \omega_L)) \quad (99)$$

and finally the *Bloch equations* are derived

$$\frac{dr_x}{dt} = -\Delta r_y - \Omega_i r_z \quad (100)$$

$$\frac{dr_y}{dt} = \Delta r_x + \Omega_r r_z \quad (101)$$

$$\frac{dr_z}{dt} = \Omega_i r_x - \Omega_r r_y \quad (102)$$

where $\Delta = \omega_0 - \omega_L$ is the detuning ([20]; [21], p. 123-127; [22], p. 32-33).

13. DERIVATION OF THE MAXWELL WAVE EQUATION

Starting of from the well known Maxwell's equations in SI units,

$$\nabla \times H = j + \frac{dD}{dt} \quad (103)$$

$$\nabla \times E = -\frac{dB}{dt} \quad (104)$$

$$\nabla \cdot D = \zeta \quad (105)$$

$$\nabla \cdot B = 0 \quad (106)$$

where H is the magnetic field, E is the electric field, D is the dielectric flux, B is the magnetic flux, j is the current density of free carriers and ζ is the free charge density.
The following material equations will be used

$$D = \epsilon E + P_{total} \quad (107)$$

$$P_{total} = P_{host} + P \quad (108)$$

$$P_{host} = \chi \epsilon E \quad (109)$$

$$B = \mu H + \eta \quad (110)$$

where P_{total} is the macroscopic electric dipole polarization, P_{host} is the host material which is linear, χ is the electric susceptibility, P is the polarization for the material of interest that will be given from the Bloch vector. η is the magnetization, ϵ is the dielectric permeability and μ is the magnetic permeability in the host medium.
Taking the curl of Eq. (104) gives

$$\nabla \times (\nabla \times E) = -\nabla \times \frac{dB}{dt} \tag{111}$$

$$\nabla(\nabla E) - \Delta E = -\nabla \times \frac{d}{dt}(\mu H + \eta) \tag{112}$$

$$\nabla(\nabla E) - \Delta E = -\frac{d}{dt}(\mu \nabla \times H + \nabla \times \eta) \tag{113}$$

Inserting Eq. (103) and Eq. (107) into Eq. (113)

$$\nabla(\nabla E) - \Delta E = -\frac{d}{dt}\left(\mu\left(j + \epsilon(1+\chi)\frac{dE}{dt} + \frac{dP}{dt}\right) + \nabla \times \eta\right) \tag{114}$$

$$\nabla(\nabla E) - \Delta E = -\mu\left(\frac{dj}{dt} + \epsilon(1+\chi)\frac{d^2E}{dt^2} + \frac{d^2P}{dt^2}\right) - \nabla \times \frac{d\eta}{dt} \tag{115}$$

The following assumptions will be made: $\eta = 0$, $j = \sigma E$, $\zeta = 0$ and $\nabla E = 0$ where σ is the electrical conductivity introduced due to ohmic losses in the host material. Moreover for the host material $n^2 := (1 + \chi)$ is the constant refractive index squared. Eq. (115) turns into

$$\Delta E = \mu\left(\sigma\frac{dE}{dt} + \epsilon n^2\frac{d^2E}{dt^2} + \frac{d^2P}{dt^2}\right) \Leftrightarrow \Delta E - \mu\sigma\frac{dE}{dt} - \frac{n^2}{c^2}\frac{d^2E}{dt^2} = \mu\frac{d^2P}{dt^2} \tag{116}$$

where $c = 1/\sqrt{\epsilon\mu}$ is the speed of light in vaccum. Moreover assume that the ohmic losses is zeros ($\sigma = 0$). This will give us the Maxwell wave equation in a medium, together with a host material ([23], p. 21-23; [24] p. 97-103; [25] p. 266-267)

$$\Delta E - \frac{n^2}{c^2}\frac{d^2E}{dt^2} = \mu\frac{d^2P}{dt^2} \tag{117}$$

The electric field is now written as Eq. (79) and inserted into Eq. (117), moreover assuming that the space is one-dimensional:

$$\frac{\hbar}{2\mu_{ge}}\left(\frac{d^2}{dz^2} - \frac{n^2}{c^2}\frac{d^2}{dt^2}\right)(e^{i(\omega_L t - kz)}(\Omega_r + i\Omega_i) + e^{-i(\omega_L t - kz)}(\Omega_r - i\Omega_i)) = \mu\frac{d^2P}{dt^2} \tag{118}$$

Note that

$$\frac{d^2}{dx^2}(f(x)e^{i\beta x}) = (f''(x) + 2i\beta f'(x) - \beta^2 f(x))e^{i\beta x} \tag{119}$$

where $f(x)$ is an arbitrary continous function and β constant. The *slowly varying envelope approximation* (SVEA) will now be used. This approximation assumes that the $f(x)$ is varying slowly in time compared to the laser frequency β. This gives the following inequalities $f''(x) \ll \beta f'(x) \ll \beta^2 f(x)$, and hence

$$\frac{d^2}{dx^2}(f(x)e^{i\beta x}) =^{SVEA} (2i\beta f'(x) - \beta^2 f(x))e^{i\beta x} \tag{120}$$

SVEA will be used for the Rabi frequencies Ω_r and Ω_i, assuming that they are slowly variying compared to the laser frequency ω_L ($\Omega''_{r/i} \ll \omega_L \Omega'_{r/i} \ll \omega_L^2 \Omega_{r/i}$).

Developing the left-hand side in Eq. (118) (the wavenumber $k := \omega_L n/c$),

$$\frac{\hbar}{2\mu_{ge}}\left(\frac{d^2}{dz^2} - \frac{n^2}{c^2}\frac{d^2}{dt^2}\right)(e^{i\omega_L(t-zn/c)}(\Omega_r + i\Omega_i) + e^{-i\omega_L(t-zn/c)}(\Omega_r - i\Omega_i)) = \tag{121}$$

$$\frac{\hbar}{2\mu_{ge}}\left(\frac{d^2}{dz^2} - \frac{n^2}{c^2}\frac{d^2}{dt^2}\right)(e^{i\omega_L(t-zn/c)}(\Omega_r + i\Omega_i)) + c.c. =^{SVEA} \tag{122}$$

$$\frac{\hbar}{2\mu_{ge}}e^{i\omega_L(t-zn/c)}((-2i\frac{\omega_L n}{c}\frac{d}{dz}(\Omega_r + i\Omega_i) -$$

$$\frac{\omega_L^2 n^2}{c^2}(\Omega_r + i\Omega_i)) - (2i\frac{\omega_L n^2}{c}\frac{d}{dt}(\Omega_r + i\Omega_i) - \frac{\omega_L^2 n^2}{c^2}(\Omega_r + i\Omega_i))) + c.c. = \tag{123}$$

$$\frac{-i\omega_L\hbar}{\mu_{ge}}e^{i\omega_L(t-zn/c)}\left(\frac{n}{c}\frac{d}{dz}(\Omega_r + i\Omega_i) + \frac{n^2}{c^2}\frac{d}{dt}(\Omega_r + i\Omega_i)\right) + c.c. \tag{124}$$

The macroscopic polarization will be expressed in terms of the expectation value of the dipole moment integrated over all detunings:

$$P(z,t) \;=\; N\int_{-\infty}^{+\infty} g(\Delta)\langle M\rangle d\Delta \tag{125}$$

where N is the number of atoms, $g(\Delta)$ is the inhomogeneous profile and $\langle M\rangle$ is the expectation value of the dipole moment. The inhomogenous profile satisfy the following condition ([26], p. 805):

$$\frac{1}{2\pi}\int_{-\infty}^{+\infty} g(\Delta)d\Delta = 1 \tag{126}$$

The expectation value of the dipole moment is calculated from quantum mechanics. This is how the Maxwell wave equation is connected to quantum mechanics and hence this is a semi-classical model. The atoms is treated quantum mechanicly while the light is treated classically. From Eq. (8) the expectation value of the observable M can be calculated

$$\begin{aligned}
\langle M\rangle &= tr(\rho M) && (127)\\
&= = tr(\rho(\mu_{ge}|g\rangle\langle e| + \mu_{ge}^*|e\rangle\langle g|)) && (128)\\
&= \rho_{ge}\mu_{ge}^* + \rho_{ge}^*\mu_{ge} && (129)\\
&= \rho_{ge}\mu_{ge}^* + c.c. && (130)
\end{aligned}$$

From Theorem 8.2:

$$\rho_{ge} = \frac{1}{2}(r_x + ir_y) \tag{131}$$

Inserting Eq. (131) into Eq. (130) and also letting the density matrix elements oscillate as $e^{i(\omega_L t - kz)}$ gives

$$\langle M\rangle \;=\; \frac{1}{2}(r_x + ir_y)e^{i(\omega_L t-kz)}\mu_{ge}^* + c.c. \tag{132}$$

Now Eq. (132) is inserted into Eq. (125)

$$P(z,t) \;=\; \frac{1}{4\pi}N\int_{-\infty}^{+\infty} g(\Delta)(r_x + ir_y)e^{i(\omega_L t-kz)}\mu_{ge}^* d\Delta + c.c. \tag{133}$$

Developing the right-hand side of Eq. (117) (the wavenumber $k := \omega_L n/c$). SVEA will be used for the Bloch vector components r_x and r_y, assuming that they are slowly variying compared to the laser frequency ($r''_{x/y} \ll \omega_L r'_{x/y} \ll \omega_L^2 r_{x/y}$)

$$\mu\frac{d^2}{dt^2}\left(\frac{1}{4\pi}N\int_{-\infty}^{+\infty} g(\Delta)(r_x+ir_y)e^{i(\omega_L t-kz)}\mu_{ge}^* d\Delta\right)+c.c.= \tag{134}$$

$$\frac{1}{4\pi}\mu N\int_{-\infty}^{+\infty} g(\Delta)\frac{d^2}{dt^2}\left((r_x+ir_y)e^{i(\omega_L t-kz)}\mu_{ge}^*\right)d\Delta+c.c.=^{SVEA} \tag{135}$$

$$\frac{1}{4\pi}\mu N\int_{-\infty}^{+\infty} g(\Delta)\left(e^{i(\omega_L t-kz)}(-\omega_L^2)(r_x+ir_y)\mu_{ge}^*\right)d\Delta+c.c.= \tag{136}$$

$$-\omega_L^2\frac{1}{4\pi}\mu N e^{i(\omega_L t-kz)}\int_{-\infty}^{+\infty} g(\Delta)(r_x+ir_y)\mu_{ge}^* d\Delta+c.c. \tag{137}$$

Now the right-hand side is equal to the left-hand side, that is Eq. (124) equal to Eq. (137)

$$\frac{-i\omega_L\hbar}{\mu_{ge}}e^{i\omega_L(t-zn/c)}\left(\frac{n}{c}\frac{d}{dz}(\Omega_r+i\Omega_i)+\frac{n^2}{c^2}\frac{d}{dt}(\Omega_r+i\Omega_i)\right)+c.c.=$$

$$-\omega_L^2\frac{1}{4\pi}\mu N e^{i(\omega_L t-kz)}\int_{-\infty}^{+\infty} g(\Delta)(r_x+ir_y)\mu_{ge}^* d\Delta+c.c. \tag{138}$$

$$ie^{i\omega_L(t-zn/c)}\left(\frac{d}{dz}(\Omega_r+i\Omega_i)+\frac{n}{c}\frac{d}{dt}(\Omega_r+i\Omega_i)\right)+c.c.=$$

$$\frac{\mu_{ge}\omega_L\mu c N}{4\pi\hbar n}e^{i(\omega_L t-kz)}\int_{-\infty}^{+\infty} g(\Delta)(r_x+ir_y)\mu_{ge}^* d\Delta+c.c. \tag{139}$$

Extract the real and the imaginary part as well as the term $e^{i\omega_L(t-zn/c)}$ into two different equations gives

$$\frac{d\Omega_r}{dz}+\frac{n}{c}\frac{d\Omega_r}{dt}=\frac{\alpha}{2\pi}\int_{-\infty}^{+\infty} g(\Delta)r_y d\Delta \tag{140}$$

$$\frac{d\Omega_i}{dz}+\frac{n}{c}\frac{d\Omega_i}{dt}=-\frac{\alpha}{2\pi}\int_{-\infty}^{+\infty} g(\Delta)r_x d\Delta \tag{141}$$

where $\alpha=\frac{|\mu_{ge}|^2\omega_L N}{2c\hbar n\epsilon}$ is called the absorption coefficient ([19], p. 14-16; [20]).

14. THE COMPLETE EQUATIONS

The postulates of quantum mechanics is only valid for a closed system. When performing an experiment the system 2-level atom model is not a closed system. A quick fix to solve this problem is to introduce two phenomenological decay constants T_1 and T_2. $1/T_1$ is the rate for an atom to relax toward equilibrium. $1/T_2$ is the rate at which the coherence will decrease through for example collisions. The complete Maxwell-Bloch (MB) equations is then Eq. (100)-(102) together with Eq.

(140) and Eq. (141).

$$\frac{dr_x(z,t,\Delta)}{dt} = -\Delta r_y(z,t,\Delta) - \Omega_i(z,t) r_z(z,t,\Delta) - \frac{r_x(z,t,\Delta)}{T_2} \tag{142}$$

$$\frac{dr_y(z,t,\Delta)}{dt} = \Delta r_x(z,t,\Delta) + \Omega_r(z,t) r_z(z,t,\Delta) - \frac{r_y(z,t,\Delta)}{T_2} \tag{143}$$

$$\frac{dr_z(z,t,\Delta)}{dt} = \Omega_i(z,t) r_x(z,t,\Delta) - \Omega_r(z,t) r_y(z,t,\Delta) - \frac{1 + r_z(z,t,\Delta)}{T_1} \tag{144}$$

$$\frac{d\Omega_r(z,t)}{dz} + \frac{n}{c}\frac{d\Omega_r(z,t)}{dt} = \frac{\alpha}{2\pi}\int_{-\infty}^{+\infty} g(\Delta) r_y(z,t,\Delta) d\Delta \tag{145}$$

$$\frac{d\Omega_i(z,t)}{dz} + \frac{n}{c}\frac{d\Omega_i(z,t)}{dt} = -\frac{\alpha}{2\pi}\int_{-\infty}^{+\infty} g(\Delta) r_x(z,t,\Delta) d\Delta \tag{146}$$

15. RETARDED TIME AND THE RUNGE-KUTTA METHOD

A smart change in variables for the MB equations will be done in order to easily solve the equations. Lets introduce two new variables

$$\tau(z,t) = t - \frac{zn}{c} \tag{147}$$

$$z'(z,t) = z \tag{148}$$

where $\tau := \tau(z,t)$ is called retarded time and $z' := z'(z,t)$ is introduced for our convinence. The chain rule will be applied [27].

$$\frac{d}{dt} = \frac{d\tau}{dt}\frac{d}{d\tau} + \frac{dz'}{dt}\frac{d}{dz'} \tag{149}$$

$$\frac{d}{dz} = \frac{d\tau}{dz}\frac{d}{d\tau} + \frac{dz'}{dz}\frac{d}{dz'} \tag{150}$$

An intermediate step in order to continue the calculations

$$\begin{aligned} \frac{d\tau}{dt} &= 1 \quad \frac{dz'}{dt} = 0 \\ \frac{d\tau}{dz} &= -\frac{n}{c} \quad \frac{dz'}{dz} = 1 \end{aligned} \tag{151}$$

Inserting the above in Eq. (149) and Eq. (150) gives

$$\frac{d}{dt} = \frac{d}{d\tau} \tag{152}$$

$$\frac{d}{dz} = -\frac{n}{c}\frac{d}{d\tau} + \frac{d}{dz'} \tag{153}$$

These result will now be substituted into the MB equations,

$$\frac{dr_x(z',\tau,\Delta)}{d\tau} = -\Delta r_y(z',\tau,\Delta) - \Omega_i(z',\tau)r_z(z',\tau,\Delta) - \frac{r_x(z',\tau,\Delta)}{T_2} \tag{154}$$

$$\frac{dr_y(z',\tau,\Delta)}{d\tau} = \Delta r_x(z',\tau,\Delta) + \Omega_r(z',\tau)r_z(z',\tau,\Delta) - \frac{r_y(z',\tau,\Delta)}{T_2} \tag{155}$$

$$\frac{dr_z(z',\tau,\Delta)}{d\tau} = \Omega_i(z',\tau)r_x(z',\tau,\Delta) - \Omega_r(z',\tau)r_y(z',\tau,\Delta) - \frac{1+r_z(z',\tau,\Delta)}{T_1} \tag{156}$$

$$\frac{d\Omega_r(z',\tau)}{dz'} = \frac{\alpha_0}{2\pi}\int_{-\infty}^{+\infty} g(\Delta)r_y(z',\tau,\Delta)d\Delta \tag{157}$$

$$\frac{d\Omega_i(z',\tau)}{dz'} = -\frac{\alpha_0}{2\pi}\int_{-\infty}^{+\infty} g(\Delta)r_x(z',\tau,\Delta)d\Delta \tag{158}$$

These equations can now be solved numerically. In the numerical model $g(\Delta)$ can't be defined from $-\infty$ to $+\infty$, therefore a different α will be used called α_0. $\alpha_0 := \alpha(\omega_0)/g(\omega_0)$ where $g(\omega_0) \neq 0$ ([22], p. 37). The numerical program will contain three nested loops. Whereas the outermost loop runs over all z-slices, the middleloop runs over all detunings. The innermost loop contains the Bloch equations, these can easily be solved by the classical Runge-Kutta method for given z' and Δ [28]. When the two inner loops has finished, the integral (the macroscopic polarization) for the Maxwell part can be calculated. Note that the variable substitution is vital to get a efficient and fast numerical program.

Part VII
Quantum memory protocols

16. THEORY

A. Homogenous- , inhomogenous linewidth and spectral hole burning

The *homogenous linewidth* is the width in the frequency domain that an ion can absorb or emit electromagnetic radiation. The homogenous linewidth has a lorentzian shape and the linewidth is $\Gamma_h = 1/(\pi T_2)$, where T_2 is the coherence time introduced in Section 14.
The doped ions in a rare-earth-ion-doped crystal are embedded in a crystal lattice. Due to imperfections in the lattice, the transition frequencies between ions in the crystal varies. The *inhomogenous profile* is created by summing up all the ion's homogenous linewidths with their respectively transition frequencies. In the 2-level MB equations the ions transition frequencies is given by the detuning Δ and the inhomogenous profile is given by the function $g(\Delta)$. The inhomogenous profile has a gaussian shape. For example in the case of a $Pr^{3+} : Y_2SiO_5$ the inhomogenous profile is in the order of 5 GHz wide while the homogenous profile is in order of kHz.
A concept that is often refered to in this thesis is the absorption profile for an inhomogenous profile mainly in the context of a spectral hole (sometimes called spectral pit). The absorption profile refers to a three-dimensional picture where the x-axis represents a spatial one-dimensional position in the crystal, on the y-axis represents the detuning and the z-axis represent the amount of absorbers/ions (sometimes the spatial dimension is neglected). A spectral hole (stricty speaking the term is: persistent spectral hole) can be created in the inhomogenous profile. Suppose the atomic structure is limited to a 3-level system with two ground states and one excited state. An incoming laser pulse excites some population from one ground state to the excited state. With some probability the excited population will relax to one of the two ground states (given that this is possible). The lifetime between the ground states are much longer than the lifetime in the excited state. It's thereby possible to "burn away" population from one ground state to another. This is called optical pumping. The incoming pulses is usually called burn-pulses for this reason. Due to the broad inhomogenous profile, different ions with different transition frequencies can be addressed by choosing the incoming laser frequency. By scanning the laser in frequency it's possible to create a wide spectral hole. When a spectral hole has been created some ions can be burned back into the pit ([29], [22]). This burn-back procedure is important for all the quantum memory protocols described in this thesis. To be able to have an absorption profile with one or more narrow peaks inside a spectral hole is one key ingredient to get a high efficient quantum memory. In the results and discussion section, different shapes of the burned-back peaks will be compared against each other.

B. What is a quantum memory?

To get a feeling of what a quantum memory is, it's good first to look at a classical computer memory. A classical memory is a device that can store bits over time and on-demand release the information. The bits can be stored in many different ways. For a classical computer the bits are normally stored as charges or magnetization of memory cells.
A quantum memory is a device that can store qubits. The qubits should be able to be stored for a certain amount of time and released on-demand. There are four things that are important when realizing a quantum memory [30]:

- The storage and recall efficiency: The efficiency is in most cases defined to be the ratio between the output and input quantum state amplitudes squared.
- Fidelity: This is the overlap between the output and the input quantum state wave functions.
- Storage time: The separation in time between the input and output quantum states.
- Multi-mode: The number of optical modes that can be stored.

In the following sections a number of quantum memory protocols are described. All these protocols have the same basic technique of exploiting the inhomogenous profile in for example a rare-earth-ion-doped crystal. The advantage of using a rare-earth-ion-doped crystal is the long coherence times (T_2) at cryogenic temperature. The information carriers will consist of single photons, these are coherently absorbed by an ensemble of atoms. The recall process of the photon is done by a certain technique or structure that makes the atoms rephase. When the ensemble of atoms rephase they generate a macroscopic polarization which affects the field according to Maxwell's equations. Optimally this process sends out a photon that contains the same quantum information as the incoming photon that was stored [22].

C. Definition of efficiency

The efficiency of a quantum memory is defined as the ratio between the integral of the intensity of the outgoing stored pulse and the integral of the intensity of the incoming pulse:

$$\eta = \frac{\int_{t_2}^{t_3} |E_{echo}(t)|^2 dt}{\int_{t_0}^{t_1} |E_{inc}(t)|^2 dt} \tag{159}$$

where η is the efficiency, $|E_{echo}(t)|^2$ is proportional to the outgoing stored pulse intensity and $|E_{inc}(t)|^2$ is proportional to the intensity of the incoming pulse. The span in the time-domain of the incoming pulse is between t_0 and t_1 and the span in the time-domain of the outgoing stored pulse is between t_2 and t_3.

D. CRIB

Controlled reversible inhomogeneous broadening (CRIB) first proposed by Moiseev and Kröll [3], exploits a hidden time-reversal symmetry. This symmetry forces the atomic ensemble to rephase and reproduce the stored photon. This concept will be explained by two different implementations called the transverse and the longitudal CRIB both relying on the DC Stark effect. The DC Stark effect will have different effect for different type of crystals. For one type of crystal the doped ions have two possible orientations of the permanent electric dipole with respect to a electric field. The effect has been measured experimentally and shown in Figure 6. In the other type of materials every ion has a permanent electric dipole moment in a random orientation with respect to a electric field.

1. Transverse CRIB

The transverse CRIB protocol was introduced by M.Nilsson and Kröll [31] and investigated analytically by Sangouard et. al. [32].

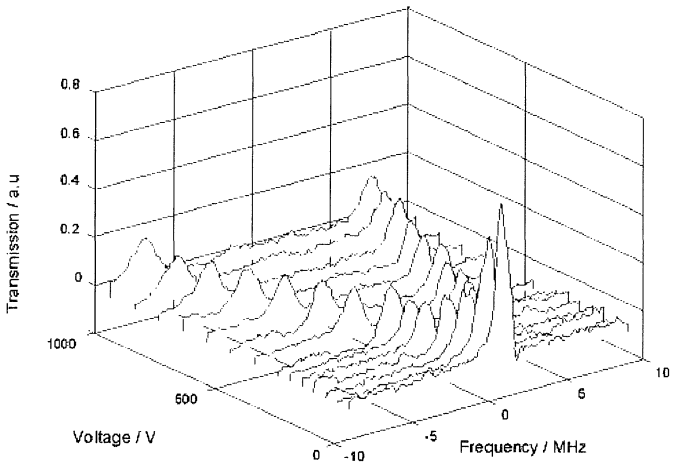

FIG. 6: The DC Stark effect for $Eu : YAlO_3$. The resonance frequency splits into two parts, this is due to the fact that there are two possible orientations of the permanent electric dipole moment of the doped ions with respect to the field. The stronger electric field the more separation between the levels. What can be seen is one initial spectral hole for zero voltage that splits in two parts for non-zero voltage ([22], p. 14).

In this subsection an intuitive step-by-step description of how the scheme works will be done. The initial scheme was to include a third level in order to reverse the propagation direction of the outgoing stored pulse. The reason to reverse the propagation of the outgoing stored pulse is to exceed the maximum efficiency limit of 54% that occurs when the outgoing stored pulse propagates in forward direction [32]. In the intuitive step-by-step description the implication of the third level will be excluded. The ions in the crystal are assumed to have a permanent electric dipole moment in a random orientation with respect to a electric field.

1. Prepare a peak of absorbing ions inside a spectral hole. This is shown in Figure 7a. The peak will contain a large number of ions.

2. A constant electric field is now turned on. This will shift all the ions transition frequency randomly since the ions are assumed to have a random orientation of their permanent electric dipole moment. The inital peak is then spread out more or less uniformly, shown in Figure 7b. This inhomogenous profile in Figure 7b will now be defined as $g(\Delta)$ (Eq. (125)).

3. A light pulse (for example a single photon) can now be sent in to the material. Suppose the light pulse entered at time $t = t_0$. The frequency-span of the incoming pulse should not be broader than the uniform structure inside the spectral hole. Given that there are high absorption (a lot of ions in in the initial peak) the pulse will be almost completely absorbed. The incoming pulse will excite the ions in the inhomogenous profile and since they are spread out over different frequencies they will start to dephase relative to each other.

4. At time $t = t_0 + \tau$ the electric field is reversed, shown in Figure 7c. This will cause all ions to reverse their shift: $g(\Delta) \rightarrow g(-\Delta)$ given that $\Delta = 0$ is the center position of the inital peak, this is shown in Figure 7a. It should be noted that the transformation $g(\Delta) \rightarrow g(-\Delta)$ is a simplification that assumes that the inital peak is a delta function. Since all ions have reversed their shift they will get in phase at time $t = t_0 + 2\tau$ and thereby release the stored pulse.

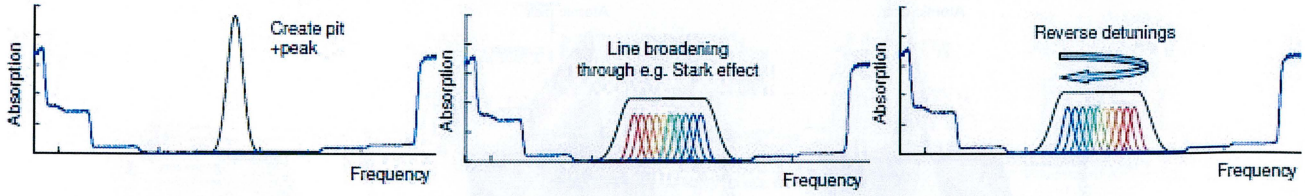

(a) Step 1 (b) Step 2 (c) Step 4

FIG. 7: Step 1,2 and 4 are visualized for the transverse CRIB protocol. Figures from [29]

2. *Longitudal CRIB/ GEM*

Longitudal CRIB, also called gradient echo memory (GEM), first demonstrated experimentally by Sellars et. al. [33] and in year 2010 efficiency as high as 70% was obtained experimentally [4]. The protocol was investigated analytically by Longdell et. al. [34]. The protocol will be explained by a step-by-step description. GEM is easier to implement than transverse CRIB with respect to get high efficiency. The reason for this is that GEM doesn't suffer from the maximum 54% efficiency limit in forward direction and hence GEM doesn't need any third level to reverse the propagation of the outgoing stored pulse. Even though GEM is easier to implement it should be taken into consideration that a phase shift is applied for the outgoing stored pulse. Suggestions to avoid the phase shift is to for example put two memories in row with opposite gradients and therefore cancel the phase shift of the photon [34].
The doped ions in the crystal are assumed to have one possible orientation of their permanent electric dipole moment with respect to the field (actually there are two orientations of the doped ions but one of the orientation is excluded).

1. Prepare a peak of absorbing ions inside a spectral hole. This is shown in Figure 8a, note that the z-dependency is included and the edges of the spectral hole are not shown compared to Figure 7a. The peak will contain a large number of ions.

2. A linear electric field with respect to the z-position is turned on. This can mathematically be represented as $\eta(z,t) = \eta_0 \cdot (z - L/2)$ where $\eta(z,t)$ is the electric field strength, η_0 is the maximum field strength and L is the total length of the crystal. All ions for a given electric field strength will shift the same amount since they have the same orientation of their permanent electric dipole moment with respect to the field. The result can be seen in Figure 8b.

3. A light pulse (for example a single photon) can now be sent in to the material. Suppose the light pulse entered at time $t = t_0$. The frequency of the incoming pulse should not be broader than the line broadening. Given that there are high absorption (a lot of ions in in the initial peak) the pulse will be almost completely absorbed. The incoming pulse will excite the ions in the inhomogenous profile and since they are spread out over different frequencies they will start to dephase relative to each other.

4. At time $t = t_0 + \tau$ the electric field is reversed: $\eta(z, t > t_0 + \tau) = -\eta_0 \cdot (z - L/2)$, this can be seen in Figure 8c. This will cause all ions within the same z-position to shift equally much for any given frequency. At time $t = t_0 + 2\tau$ all ions have aquired the same phase and thereby release the stored pulse.

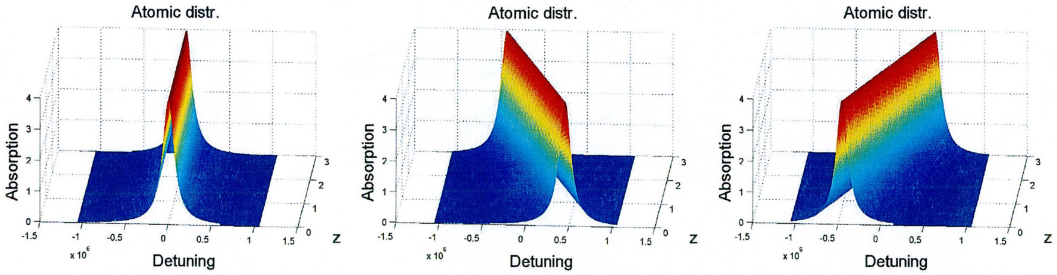

(a) Step 1 (b) Step 2 (c) Step 4

FIG. 8: Step 1,2 and 4 are visualized for the longitudal CRIB protocol.

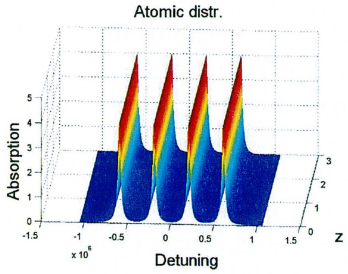

FIG. 9: Four AFC peaks inside a spectral hole.

E. AFC

The atomic frequency comb (AFC) protocol was introduced and analytically investigated by Afzelius et. al. [5]. Experimental results of 35% efficiency was shown by Amari et. al. in the beginning of 2010 [6]. The AFC protocol doesn't rely on any DC Stark effect as the transverse/longitudal CRIB protocols. In this scheme it's the equally spaced frequency comb in the absorption profile that creates the rephasing. This protocol has been analytically proven to obtain a maximum efficiency of 54% when outgoing stored pulse propagates in forward direction (note that this is the same limit as for the transverse CRIB protocol) [5]. But by placing the crystal inside a cavity it has been shown theoretically that efficiency up to 92% (whereas higher efficiency is only limited by the finesse of the atomic frequency comb) given that the cavity is on resonance [8]. An example of how the absorption profile should look like is shown in Figure 9 (the edges of the spectral hole have been discarded). The frequency-span of the incoming pulse should not be smaller than the distance between the AFC peaks and the pulse should not be broader than the total frequency-span of the peaks. The distance between the AFC peaks is denoted as Δ and the FWHM of the peaks is denoted as γ. Suppose a light pulse (for example a single photon) is sent in to the material at time $t = t_0$. At time $t = t_0 + k2\pi/\Delta$ (given that Δ is in radians per second) where k is an positive integer the ions will get in phase and release some parts of the stored pulse.
The *finesse* of the AFC is defined as: $F := \Delta/\gamma$.

F. Difference between effective absorption and peak absorption

Two different notions of absorption will be used. The term *effective absorption* refers to how much the absorption will be in average whereas the term *peak absorption* refers to how much absorption the maximum value of a peak has. For example the AFC protocol in section 16 E the

absorption profile consists of multiple peaks. In between the peaks in frequency (see Figure 9) there are no ions absorbing. Therefore in this case the effective absorption will basicly be the peak absorption divided by the finesse. For longitudal CRIB the peak absorption will be given when the electric field is turned off. But the effective absorption will be given when the electric field is turned on. The reason for this definition of the peak absorption is because this is the value experimentalists are interested in when ordering a crystal (that is, the absorption when no structure or electric field has been created/applied).

G. Simulation of outgoing stored pulse in backward direction

In Section 15 an explanation of how to simulate the Maxwell-Bloch equations in the forward direction with three nested loops.
To easily be able to simulate when the outgoing stored pulse propagates in backward direction one crucial simplification is done. Suppose the incoming pulse starts at retarded time $T = t_0$ and ends at retarded time $T = t_1$. Then the trick is to use the simulation in the forward direction up until retarded time $T = t_1$. After $T = t_1$ the most outerloop over the z-slices is performed in reverse order. This will make the outgoing stored pulse propagate in backward direction since there is no defined direction in the Rabi frequency. In reality this process will not be possible without some kind process that reverses the direction of the rephasing of the ions. This normally leads to losses in the system.

17. RESULTS AND DISCUSSION

All results in this section has been obtained by numerically solve the MB equations with the Runge-Kutta method described in Section 15. The decay rates $1/T_1$ and $1/T_2$ are set to zero otherwise noted.

A. Simulation of transverse CRIB

In an ideal world the reversed electric field for the transverse CRIB protocol will cause all ions to reverse their shift: $g(\Delta) \rightarrow g(-\Delta)$ (this occurs when the initial peak is infinitely narrow). This is the assumption taken in the simulations for the transverse CRIB protocol. The incoming light is made out of two gaussian pulses (blue curve in Figure 10), the first pulse has greater FWHM than the second one. The red cure in Figure 10 shows the outgoing pulse as a function of retarded time. As can be seen the efficiency is not very good when the outgoing pulse propagates in forward direction. This coincide with the maximum efficiency limit described in Subsection 16 D 1.
In Figure 11b the intensity inside the material can be seen as a function of retarded time and one spatial dimension, given that the outgoing stored pulse propagates in forward direction. The electric field is reversed after at $t_r = 0.8\mu s$ in retarded time and hence the outgoing stored pulse of the widest pulse comes at $t = 1.6\mu s$ in retarded time.
Note that the incoming pulse is reversed in time. The reversion of the pulse can be understood by the applied transformation $g(\Delta) \rightarrow g(-\Delta)$. Lets only look at two different positions in time of the incoming pulse in Figure 11a: $t_1 = 0\mu s$ and $t_2 = 0.4\mu s$ (this is the time when the wide respectively the narrow pulse has its center). At time t_1 the first pulse enters the material and the ions are getting excited and thus start to dephase. At time t_2 the second pulse enters the material and the ions are getting excited and thus start to dephase. So the ions that store the first pulse have dephased for a longer time relative to the second pulse. When the field is reversed at time

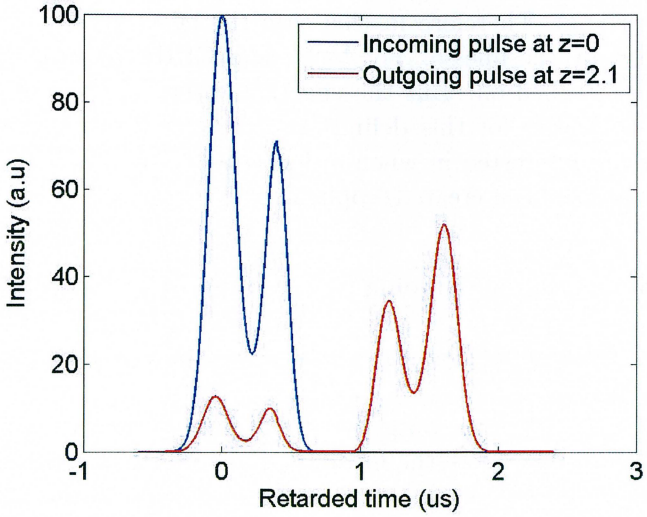

FIG. 10: Simulation of transverse CRIB. The last incoming pulse (the most narrow pulse) is sent out of the material first. Outgoing stored pulse propagates in forward z-direction. The intensity doesn't reach over 54% efficiency.

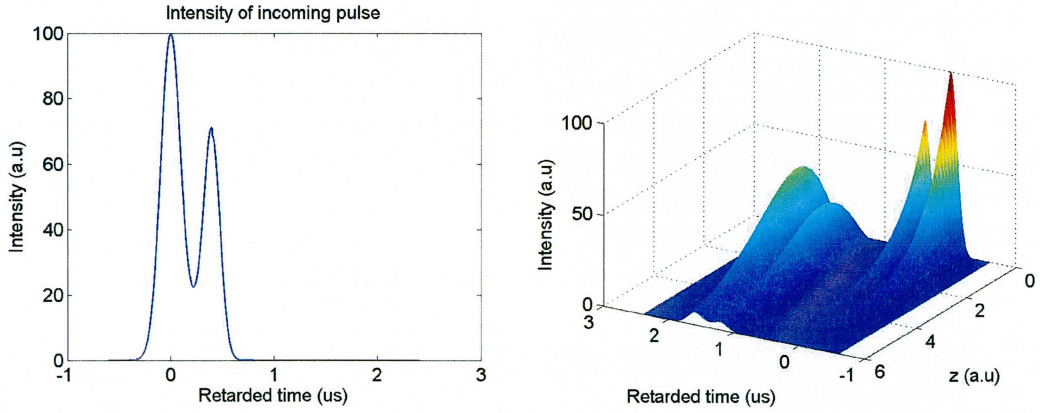

(a) Incoming pulse

(b) Intensity inside the material

FIG. 11: Simulation of transverse CRIB with spatial dimension included. Outgoing stored pulse propagates in forward z-direction. The last incoming pulse (the most narrow pulse) is sent out of the material first. Outgoing stored pulse propagates in forward z-direction. Maximum intensity at $z = 2.1$ can be seen, the intensity doesn't reach over 54% efficiency.

$t_r = 0.8\mu s$, the ions that store the first pulse will rephase at time $t_{1,rephase} = t_1 + 2\cdot(t_r - t_1) = 1.6\mu s$. But the ions that store the second pulse will rephase at time $t_{2,rephase} = t_2 + 2\cdot(t_r - t_2) = 1.2\mu s$ and hence the second pulse will be sent out first.
The maximum intensity occurs at $z = 2.1$ in Figure 11b, this would be the optimal absorption of a crystal in order to obtain the highest efficiency for the transverse CRIB in the forward direction.

In Figure 12 the intensity of the incoming pulse and outgoing stored pulse are shown as a function of retarded time, given that the outgoing stored pulse propagates in backward direction. In Figure 13b the intensity inside the material is shown as a function of retarded time and one spatial

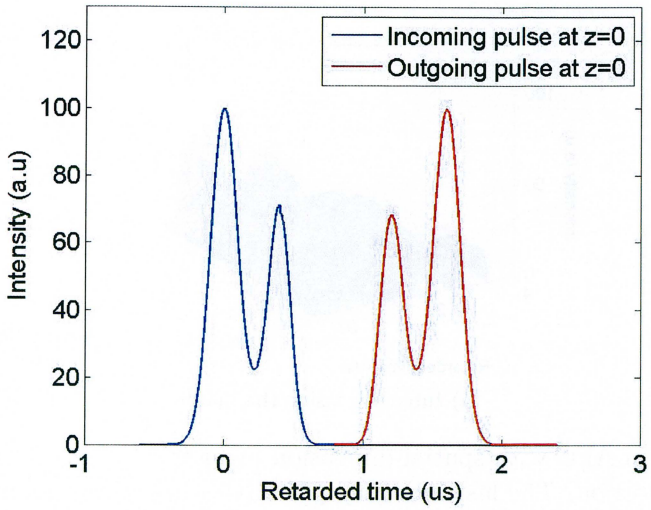

FIG. 12: Simulation of transverse CRIB. Outgoing stored pulse propagates in backward z-direction. The last incoming pulse (in the narrowest pulse) is sent out of the material first. Efficiency close to unity.

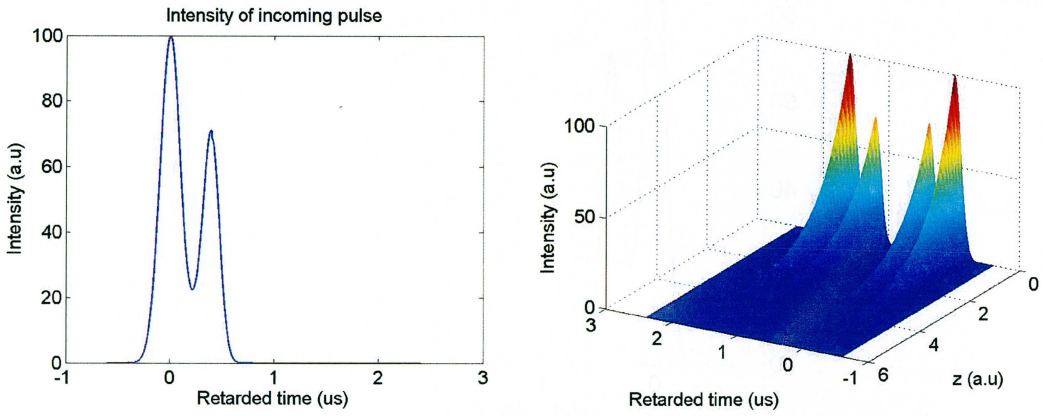

(a) Incoming pulse

(b) Intensity inside the material

FIG. 13: Simulation of transverse CRIB with spatial dimension included. Outgoing stored pulse propagates in backward z-direction. The last incoming pulse (the most narrow pulse) is sent out of the material first.

dimension, given that the outgoing stored pulse propagates in the backward direction. This gives an efficiency of the outgoing stored pulse close to unity.

B. Simulation of AFC

In Subsection 16 E it was mentioned that the AFC protocol releases an outgoing stored pulse at time $t = t_0 + k2\pi/\Delta$ given that the incoming pulse entered at $t = t_0$ and given that the spacing between the peaks was Δ radians. In Figure 14a the intensity inside the material can be seen, the incoming pulse is shown in Figure 13a. Figure 14a for the AFC protocol and Figure 11b from

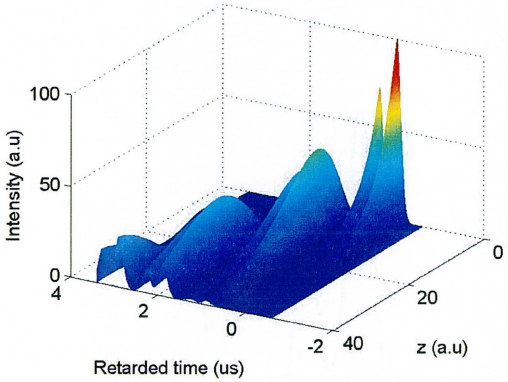

(a) Intensity inside the material

FIG. 14: Simulation of AFC with spatial dimension included. Outgoing stored pulse propagates in the forward z-direction. The last incoming pulse (the most narrow pulse) is sent out of the material last.

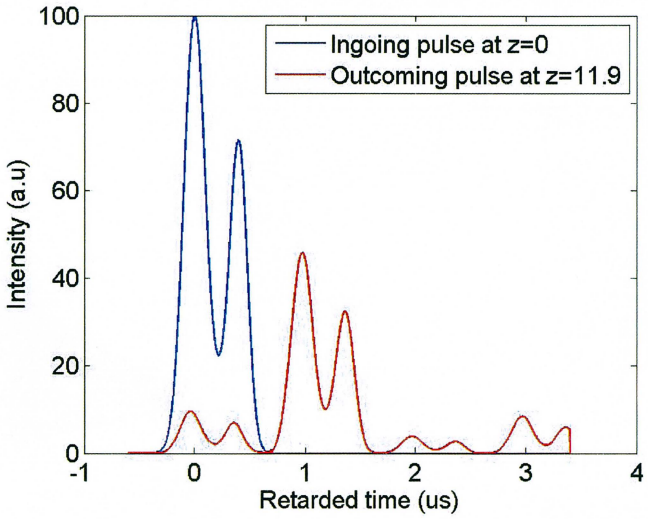

FIG. 15: Simulation of AFC. Outgoing stored pulse propagates in the forward z-direction. The last incoming pulse (the most narrow pulse) is sent out of the material last.

the transverse CRIB protocol gives similar output up to the retarded time $1.6\mu s$, that is both outgoing stored pulses are reabsorbed and releases a maximum of 54% of the incoming intensity. The difference compared to the AFC protocol is that the reabsorbed pulse is yet again reemitted inside the material after an equal amount of time. The explanation for this is the the ions rephase periodicly as described in the theory section: $t = t_0 + k2\pi/\Delta$, where k is a positive integer. Note that the second reemitted pulse has lower intensity. The reason for the decrease is that ions inside the AFC peaks within themself start to dephase relative to each other since they are not infinitely narrow in frequency. If the crystal length would be cut at $z = 11.9$ the maximum intensity of the outgoing pulse would be obtained, this can be seen in Figure 15.

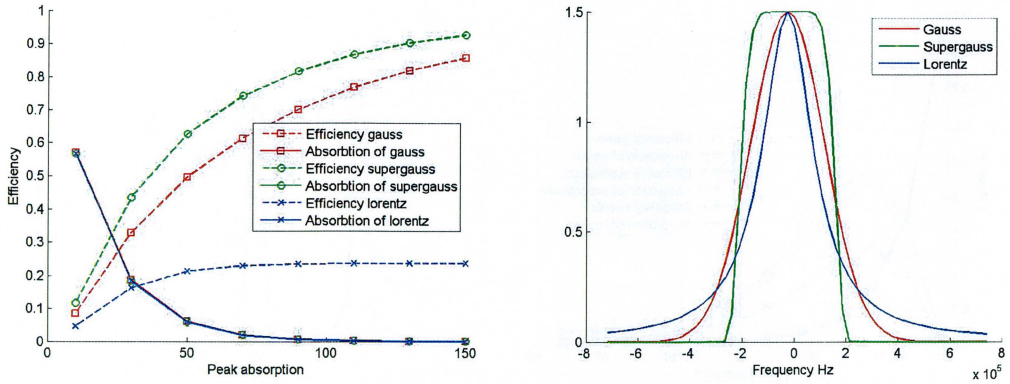

(a) Efficiency

(b) Shapes, descibed by Eq. (160)-(162)

FIG. 16: Efficiency for GEM given different absorption shapes of the initial peak. The outgoing stored pulse propagates in the forward direction. The FWHM is different for the different shapes in order to get the same effective absorption.

C. Simulation of efficiency for GEM and AFC in forward direction

Comparsion between the GEM and AFC protocol given that the echo propagtes in forward direction will be shown. In Figure 16a three different efficiency curves is shown as a function of peak absorption for GEM. The outgoing stored pulse propagates in the forward direction. The absorption curves in Figure 16a overlap, this is due to that the gauss, supergauss and lorentz function (shown in Figure 16b) are chosen such that they all contribute to the same effective absorption.
The lorentz function is described as:

$$L(\omega) = \frac{(\gamma_{Lor}/2)^2}{\omega^2 + (\gamma_{Lor}/2)^2} \tag{160}$$

where $\gamma_{Lor} = \frac{1}{8.5}$ MHz.
The gauss function is described as:

$$G(\omega) = e^{-\omega^2 ln(2)/(\gamma_{Gau}/2)^2} \tag{161}$$

where $\gamma_{Gau} = \frac{1}{6}$ MHz.
The supergauss function is described as:

$$SG(\omega) = e^{-\omega^8 ln(2)/(\gamma_{SGau}/2)^8} \tag{162}$$

where $\gamma_{SGau} = \frac{1}{5.5}$ MHz.
The difference between effective absorption and peak absorption is described in Section 16 F.
The efficiency is getting close to unity as the absorption gets higher and hence the GEM protocol can give high efficiency when the outgoing stored pulse propagates in the forward direction.
In Figure 17a three different efficiency curves is shown as a function of peak absorption for AFC. The outgoing stored pulse propagates in forward direction. The absorption curves overlap, this is due to that the gauss, supergauss and lorentz function (shown in Figure 17b) is chosen such that they all contribute to the same effective absorption.

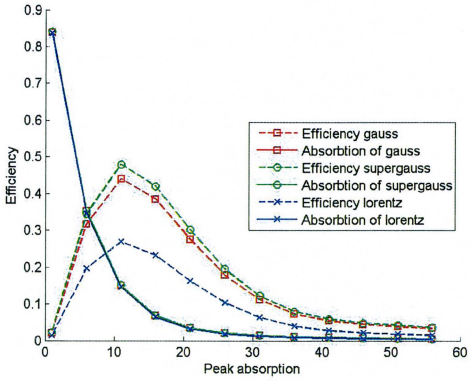

(a) Efficiency

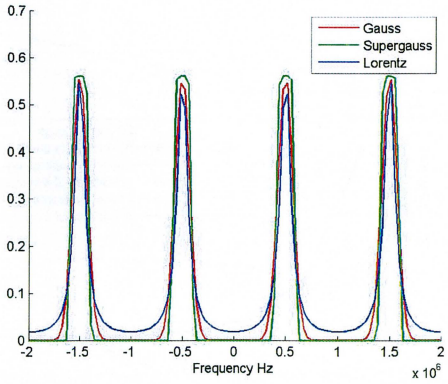

(b) AFC structure, the single peaks is descibed by Eq. (160)-(162)

FIG. 17: Efficiency for AFC given different absorption shapes of initial peaks. Outgoing stored pulse propagating in forward direction. The FWHM is different for the different shapes in order to get the same effective absorption (hence the finesse is different).

Note that the efficiency never reaches above 54%. The reason that the efficiency doesn't reach the 54% analytical limit is due to two main reasons. The first reason is that the peaks in the AFC structure have a finite finesse that leads to dephasing within the AFC peaks. The second reason is that the incoming pulse is not a perfect pulse but is actually cut-off due to the finite simulation time. Hence some frequency components of the pulse are outside of the AFC structure and are not absorbed. As can be seen in both Figure 16a and 17a the shape of the peaks are very important to get high efficiency. The sharper slope on the peaks, the better. The Lorentz shape never reaches over 30% efficiency in any of the cases. The supergauss gives the best efficiency of these three different shapes. Note that the GEM protocol needs higher peak absorption than the AFC protocol in order to absorb the incoming pulse.

D. Simulation of efficiency for GEM and AFC in backward direction

In Figure 18a three different efficiency curves are shown as functions of peak absorption for GEM. The outgoing stored pulse propagates in backward direction. The absorption curves coincide, this is due to that the gauss, supergauss and lorentz function (shown in Figure 18b) is chosen such that they all contribute to the same effective absorption. GEM seems to give fairly high efficiency in backward direction, but not as high as the forward direction given the same peak absorption (can be seen by comparing Figure 16a and 18a).

In Figure 19a, three different efficiency curves are shown as function of peak absorption for AFC. The outgoing stored pulse propagates in the backward direction. The absorption curves coincide, this is due to that the gauss, supergauss and lorentz functions (shown in Figure 19b) are chosen such that they all contribute to the same effective absorption. The efficiency is now not limited by the 54% efficiency and hence efficiency close to unity can be reached.

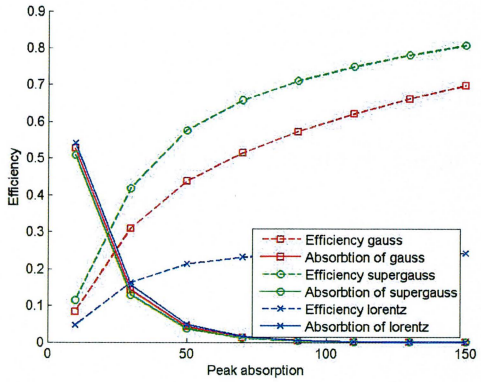

(a) Efficiency

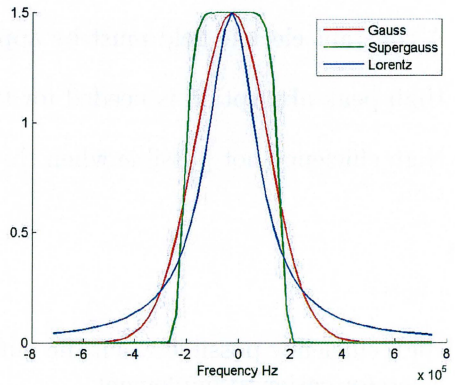

(b) Shapes, descibed by Eq. (160)-(162)

FIG. 18: Efficiency for GEM given different absorption shapes of the initial peaks. Outgoing stored pulse is propagating in the backward direction. The FWHM is different for the different shapes in order to get the same effective absorption.

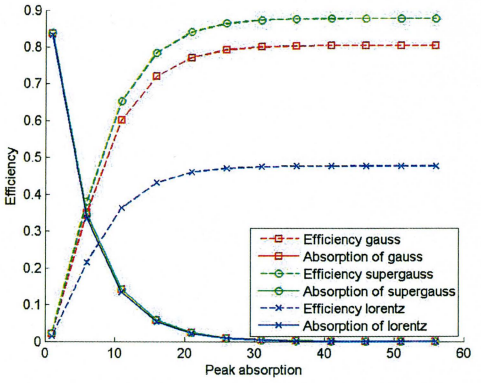

(a) Efficiency

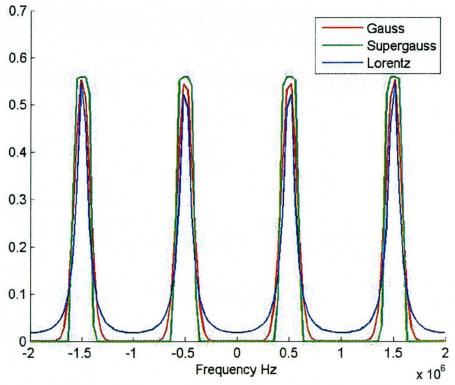

(b) AFC structure, the single peaks is descibed by Eq. (160)-(162)

FIG. 19: Efficiency for AFC given different absorption shapes of the initial peaks. Outgoing stored pulse propagating in the backward direction. The FWHM is different for the different shapes in order to get the same effective absorption (hence the finesse is different).

18. CONCLUSIONS

Three different quantum memory protcols has been introduced. A summary of the advantages and the disadvantages for the different protocols will be listed given the theory and the results in this section:

Transverse CRIB
Advantages:

- The electric field can be reversed at any given time. More freedom to decide when to release the outgoing stored pulse.

Disadvantages:

- A constant electric field must be applied.
- High peak absorption is needed for the inital peak.
- High efficiency not possible when the outgoing stored pulse propagates in the forward direction.

GEM
Advantages:

- High efficiency possible when the outgoing stored pulse propagates in the forward direction. Therefor easier to implement.
- The electric field can be reversed at any given time. More freedom to decide when to release the outgoing stored pulse.

Disadvantages:

- A linear electric field gradient must be applied.
- High peak absorption is needed for the inital peak.
- The outgoing stored pulse aquires a phase shift.

AFC
Advantages:

- The Stark shift isn't neccessary, this makes it easier to implement.
- The peak aborption is basically the effective absorption multiplied by the finesse. The peak absorption doesn't have to be too high.

Disadvantages:

- High efficiency not possible when outgoing stored pulse propagates in the forward direction.
- The emission of the outgoing stored pulse is given by the spacing between the AFC peaks, this can't be changed once the photon has entered the material. Less freedom when to release the outgoing stored pulse.

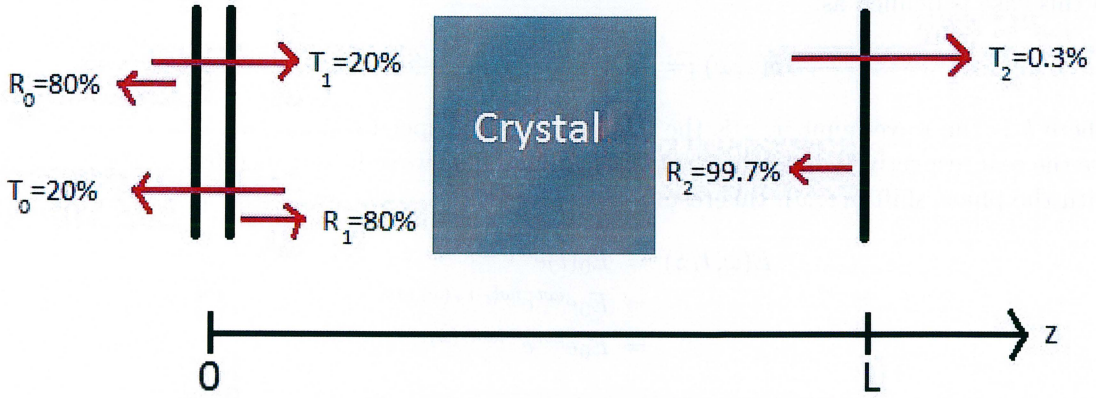

FIG. 20: Crystal inside a cavity, reflectivity and transmission shown in percent.

Part VIII
Cavity simulations by interference

19. THEORY

A quantum memory scheme has recently been realized experimentally in Lund at the Quantum information group [7]. The scheme has been suggested and analytically investigated by several theoretical papers, for example one paper by Mikael Afzelius and Christoph Simon [35] and one paper from Sergey A. Moiseev et. al. [36]. The paper from Mikael Afzelius and Christoph Simon suggest to use the AFC protocol for a crystal inside a cavity. The advantages of having a cavity for the AFC protocol is to enhance the absorption and extend the limit of 54% efficiency without using a third energy-level ([5], p. 2).
The idea of this section is to extend the paper by Mikael Afzelius and Christoph Simon and in addition understand the experimental results.

A. Derivation of transmission and reflection spectrum

Figure 20 illustrates the experimental setup. A 2mm crystal is placed between two partially transparent mirrors with different reflectivity. When a light pulse enters from the left in Figure 20 either constructive or destructive interference will occur inside the medium. Constructive interference happens for certain frequencies, these are called resonance frequencies. Light will be transmitted out of the crystal only for the resonance frequencies given that the light is not totally absorbed. In the following the transmission and reflection spectrum will be theoretically calculated in the simplest possible way. When a pulse comes in on a certain frequency the phase will change depending on the refractive index. Lets assume that the incident complex wave can be described by the following equation:

$$E_0(t) = E_0 e^{i\omega t} \tag{163}$$

where E_0 is the initial size of the amplitude, t is the time and ω is the frequency. For every roundtrip inside the cavity a phase shift and some attuenuation $\delta(z,\omega)$ is introduced. The $\delta(z,\omega)$

in this case is defined as:

$$\delta(z,\omega) := -kz = \omega(-n_r(\omega) + in_i(\omega))z/c \tag{164}$$

where k is the wave-number, z is the distance, c is the speed of light in vaccum, $n_r(\omega)$ and $n_i(\omega)$ are the real respectively imaginary refractive index. The wave from Eq. (163) will now be extended with the phase shift $\delta(z,\omega)$, this results into:

$$\begin{aligned} E(\omega,t,z) &= E_0(t)e^{i\delta(z,\omega)} && (165)\\ &= E_0 e^{i\omega t} e^{i\omega(-n_r(\omega)+in_i(\omega))z/c} && (166)\\ &= E_0 e^{i\omega t} e^{-i\omega n_r(\omega)z/c} e^{-\omega n_i(\omega)z/c} && (167) \end{aligned}$$

Note that the term $e^{-\omega n_i(\omega)z/c}$ introduces a damping effect. The intensity of the wave is attenuated as the square whereas the absorption coefficient can be identified ([37], p. 170-173):

$$\begin{aligned} |e^{-\omega n_i(\omega)z/c}|^2 &= e^{-2\omega n_i(\omega)z/c} = e^{-\alpha(\omega)z} && (168)\\ &\Leftrightarrow && (169)\\ n_i(\omega) &= \alpha(\omega)\frac{c}{2\omega} && (170) \end{aligned}$$

When comparing with experimental data the convention is to measure absorption in terms of $\alpha_L(\omega)$. This will introduce the following definition: $\alpha(\omega) := \alpha_L(\omega)/L$, where L is the length of the crystal. The absorption $\alpha_L(\omega)$ is given from experimental data so the last unknown parameter is the real refractive index. It turns out that the real and the imaginary parts of the refractive index have a strong connection by the Kramer-Kronig relations ([38], p. 13):

$$\begin{aligned} n_r(\omega) &= n(\infty) + \frac{1}{\pi}P\int_{-\infty}^{+\infty}\frac{n_i(\omega')}{\omega'-\omega}d\omega' && (171)\\ n_i(\omega) &= -\frac{1}{\pi}P\int_{-\infty}^{+\infty}\frac{n_r(\omega')-n(\infty)}{\omega'-\omega}d\omega' && (172) \end{aligned}$$

where $n(\infty) = 1.8$ is assumed so that the host material is taken into account and P is called the Cauchy principal value that removes the singularity

$$P\int_{-\infty}^{+\infty}\frac{1}{\omega'-\omega}d\omega' := \lim_{\epsilon\to 0_+}\left(\int_{-\infty}^{w-\epsilon}\frac{1}{\omega'-\omega}d\omega' + \int_{w+\epsilon}^{+\infty}\frac{1}{\omega'-\omega}d\omega'\right) \tag{173}$$

Eq. (171) can easily be solved numerically together with a small trick that approximates the solution. Instead of using the Cauchy principal value the idea is to move the singularity to the imaginary plane. First lets reformulate the equation:

$$\begin{aligned} n_r(\omega) &= n(\infty) + \frac{1}{\pi}P\int_{-\infty}^{+\infty}\frac{n_i(\omega')}{\omega'-\omega}d\omega' && (174)\\ &= n(\infty) + \frac{1}{\pi}P\int_{-\infty}^{+\infty}\frac{n_i(\omega')(\omega'-\omega)}{(\omega'-\omega)^2}d\omega' && (175)\\ &= n(\infty) + \lim_{\epsilon\to 0}\frac{1}{\pi}P\int_{-\infty}^{+\infty}\frac{n_i(\omega')(\omega'-\omega)}{(\omega'-\omega)^2+\epsilon^2}d\omega' && (176) \end{aligned}$$

The roots of the denominator are $\omega' = \omega \pm i\epsilon$, so by not taking the limit and instead choose ϵ small enough the singularity is removed from the real axis to the imaginary plane and hence,

$$n_r(\omega) \approx n(\infty) + \frac{1}{\pi} P \int_{-\infty}^{+\infty} \frac{n_i(\omega')(\omega' - \omega)}{(\omega' - \omega)^2 + \epsilon^2} d\omega' \tag{177}$$

where ϵ is small.
The transmission/reflection spectrum will be calculated by summing up all the fields coming out from the front/back of the crystal. The intensity is calculated by taking the absolute value squared of the field. The cavity transmittance is calculated by taking the ratio between the transmission intensity and the incoming intensity . The intensity coefficients are defined as $R + T = 1$ where R is the reflection coefficient and T is the transmission coefficient. The amplitude coefficients are defined as $r = \sqrt{R}$ and $t = \sqrt{T}$ ([39], p. 418). The sum is illustrated in Figure 27 and the cavity is unfolded for convenience. The total sum is calculted below:

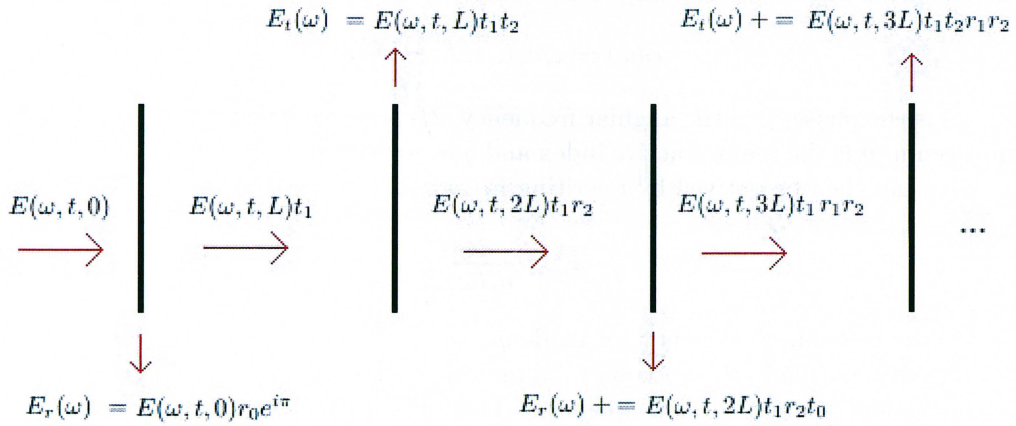

FIG. 21: Model for the cavity.

$$\begin{aligned} E_t(\omega) &= E(\omega, t, L)t_1t_2 + E(\omega, t, 3L)t_1t_2r_1r_2 + E(\omega, t, 5L)t_1t_2(r_1r_2)^2 + ... && (178)\\ &= E_0e^{i\omega t}t_1t_2e^{ikL}\sum_{j=0}(e^{i2kL}(r_1r_2))^j && (179)\\ &= \frac{E_0e^{i\omega t}t_1t_2e^{ikL}}{1 - e^{i2kL}r_1r_2} && (180) \end{aligned}$$

$$\begin{aligned} E_r(\omega) &= E(\omega, t, 0)r_0e^{i\pi} + E(\omega, t, 2L)t_1r_2t_0 + E(\omega, t, 4L)t_1r_2t_0(r_1r_2)^1 + ... && (181)\\ &= E_0e^{i\omega t}(-r_0 + t_1r_2t_0e^{i2kL}\sum_{j=0}(e^{i2kL}(r_1r_2))^j) && (182)\\ &= E_0e^{i\omega t}(-r_0 + \frac{t_1r_2t_0e^{i2kL}}{1 - e^{i2kL}r_1r_2}) && (183) \end{aligned}$$

where Eq. (179) and Eq. (182) contains a geometric sum that is evaluated [40].
Finally the cavity transmittance and reflectivity is calculated by taking the ratio between the

outgoing intensity and initial intensity:

$$T_c(\omega) = |E_t(\omega)/E_0(\omega)|^2 = \left| \frac{t_1 t_2 e^{ikL}}{1 - e^{i2kL} r_1 r_2} \right|^2 \tag{184}$$

$$R_c(\omega) = |E_r(\omega)/E_0(\omega)|^2 = \left| -r_0 + \frac{t_1 r_2 t_0 e^{i2kL}}{1 - e^{i2kL} r_1 r_2} \right|^2 \tag{185}$$

The material constants L, r_0, t_0, r_1, t_1, r_2, and t_2 is known from the crystal.

B. Mode spacing

Constructive interference inside a cavity will happen for certain frequencies. If the phase has changed by a multiple of 2π maximum constructive interference will be obtained (given that the frequency is given in radians/second). This is the round-trip phase condition:

$$\phi(\omega) := \omega n_r(\omega) 2L/c = q2\pi \tag{186}$$

where $\phi(\omega)$ is the phase, ω is the angular frequency, $2L$ is the round-trip length, c is the velocity of light in vaccum, n is the real refractive index and q is a positive integer. The resonance frequencies of the cavity can then be derived by rewriting Eq. (186):

$$\omega_q = \frac{q2\pi c}{n_r(\omega)2L} \tag{187}$$

where ω_q is the resonance frequency for mode q.
For a cold cavity with only the host material present where the refractive index $n_{host} = n_r(\omega)$ will be assumed to be constant for all frequencies. The mode spacing can then be calculated as

$$\Delta\omega_{mode} = \omega_{q+1} - \omega_q = \frac{2\pi c}{2L n_{host}} \tag{188}$$

But in general the refractive index is not constant and depends on the frequency, this makes the mode spacing calculation a little bit more complicated. By Taylor expanding to first order the real refractive index is approximately $n_r(\omega_{q+1}) \approx n_r(\omega_q) + n'(\omega_q)\Delta\omega_{mode}$, using this together with Eq. (187) an approximated expression for the mode spacing can be calculated,

$$\Delta\omega_{mode} = \omega_{q+1} - \omega_q \approx \frac{2\pi c}{2L} \frac{1}{n_r(\omega) + \omega \frac{dn_r(\omega)}{d\omega}} \bigg|_{\omega_q} \tag{189}$$

The FWHM of a resonance peak can be approximated analytically as well, but this will not be done in this thesis. The only thing to note about the approximated FWHM is that it will be proportional to the mode spacing $\Delta\omega_{mode}$ ([25], p. 432-437).

C. Group velocity

The group velocity will be an important tool to understand the results in the next section. A small introduction about group velocity will be made. The definition of the group velocity given

Name	Value
t_0	$\sqrt{0.2}$
t_1	$\sqrt{0.2}$
t_2	$\sqrt{0.003}$
r_0	$\sqrt{0.8}$
r_1	$\sqrt{0.8}$
r_2	$\sqrt{0.997}$

TABLE I: Constants for cavity simulations.

that the second and higher order derivatives of the real refractive index is negligible:

$$v_g(\omega_c) := \left(\frac{d\omega}{dk}\right)_{\omega_c} = \frac{c}{n_g(\omega_c)} = \left.\frac{c}{n_r(\omega) + \omega\frac{dn_r(\omega)}{d\omega}}\right|_{\omega_c} \tag{190}$$

where ω is the angular frequency, ω_c is the central angular frequency, k is the wavenumber, $n_g(\omega_c) := n_r(\omega_c) + \omega_c\frac{dn_r(\omega_c)}{d\omega}$ is the group refractive index and c is the velocity of light in vaccum ([38], p. 17-19). The group velocity exist due to interference between different frequencies and the envelope of a pulse travels at the group velocity due to constructive interference and destructive interference. Note that under three different circumstances the group velocity can be very different than the phase velocity.

- If $n_r(w) \approx -w\frac{dn_r(\omega)}{d\omega}$ the group refractive index will be close to zero and hence the group velocity will be larger than the speed of light in vaccum. Important to note is that this doesn't break the theory of special relativity since it's not the signal or information that travels faster than speed of light of vaccum [41]. A deeper discussion about fast light is out of the scope of this thesis.

- If $n_r(w) \ll w\frac{dn_r(\omega)}{d\omega}$ the group velocity will be much slower than the phase velocity, this is called slow light. At the Quantum information group in Lund very low group velocity has been measured experimentally, for example 2200 m/s ([42], p. 40). Slow light effects will be one key point in the next section.

- The last case will be if $n_r(\omega) < -\omega\frac{dn_r(\omega)}{d\omega}$ then the group velocity propagate in opposite direction relative to the phase velocity.

20. RESULTS AND DISCUSSION

For all simulations in this section some parameter will be constant, these are represented in Table I

A. Cold cavity

First of all lets assume that there is no inhomogenous profile. This will result in a constant real refractive index of 1.8 and a constant imaginary refractive index of 0 (the refractive index of the host material). The length of the crystal is set to $L = 0.00200010$ m, $L = 0.00200016$ m and

$L = 0.00200019$ m to the see the length dependence of the resonance frequencies. The result can be seen in Figure 22. Some longitudal modes can be seen and as the length changes the resonance frequencies changes, moreover the transmission peaks FWHM is in range of GHz. Comparsion

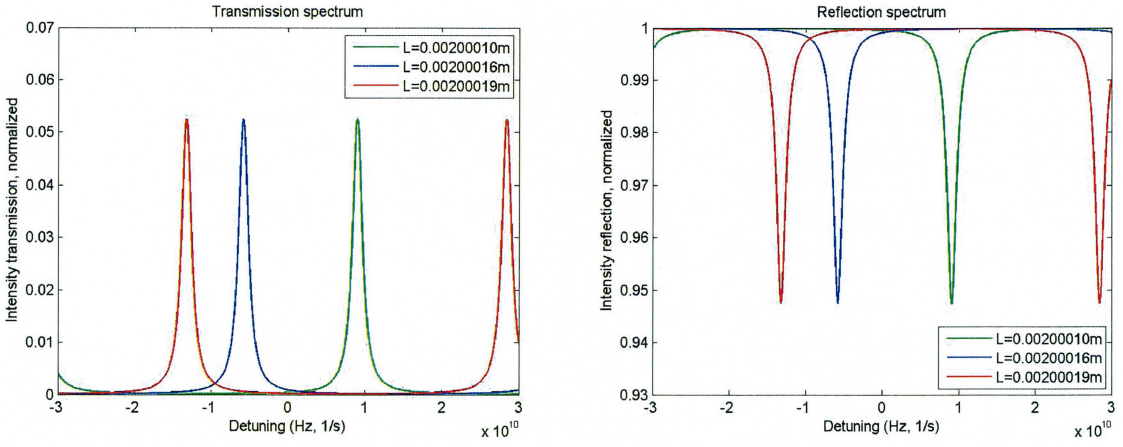

(a) Transmission spectrum

(b) Reflection spectrum

FIG. 22: Simulation of a cavity with no absorbing ions present, refractive index from host material set to 1.8. Zero detuning is at $5 \cdot 10^{14}$ Hz.

between the analytical expression in Eq. (188) and the numerical simulations will be done to see if they coincide (this is done in frequency (1/s), therefore the factor 2π is removed from the analytical expression),

$$\Delta\omega_{mode}^{analytical} = \frac{c}{2Ln_{host}} \approx 41.63GHz \tag{191}$$

$$\Delta\omega_{mode}^{numerical} \approx 41.66GHz \tag{192}$$

where $\Delta\omega_{mode}^{numerical}$ is measured in Figure 22 (distance between the red peaks), $L \approx 0.002$m and $n_{host} = 1.8$. The values coincide very well.

B. Spectral hole as a supergaussian

In the following a spectral hole from a supergauss function with a width of almost 20 MHz will be included inside the inhomogenous broadening. The result can be seen in Figure 23, note that the FWHM of the resonance frequency peak has decreased from being in the range of GHz to be in the range of MHz! This effect can understood by looking at Eq. (189) and the fact that the $FWHM$ of the resonance peak is approximately proportional to Eq. (189):

$$FWHM \propto \omega_{q+1} - \omega_q \approx \frac{2\pi c}{2L} \frac{1}{n_r(\omega) + \omega \frac{dn_r(\omega)}{d\omega}}\bigg|_{\omega_q} = \frac{2\pi}{2L} v_g(\omega_q) \tag{193}$$

so the $FWHM$ and the mode spacing are proportional to the group velocity introduced in Subsection 19 C. In Figure 24a the real refractive index is shown. As can be seen the difference between the maximum value and the minimum value of the refractive index inside the spectral hole is not large, so $\frac{dn_r(\omega)}{d\omega}$ is actually small. So at first glance it's hard to believe that the group velocity can be three orders of magnitude smaller than the phase velocity. But the wavelength of the incoming

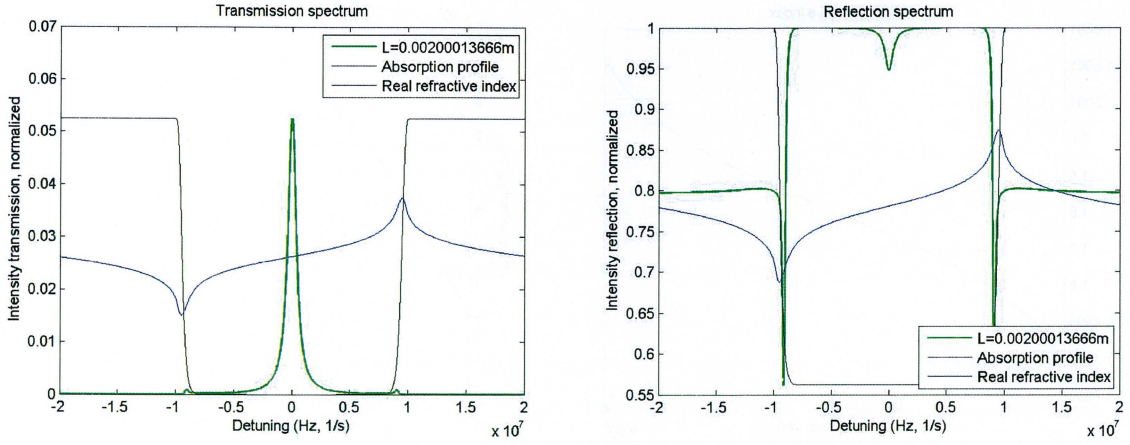

(a) Transmission spectrum

(b) Reflection spectrum

FIG. 23: Simulation of a cavity with a spectral hole present inside the medium. The spectral hole is represented as a supergaussian and the width is almost 20 MHz. The length of the crystal is chosen so that the transmission peaks is centered in the spectral hole: $L = 0.00200013666\text{m}$. The real refractive index and absorption profile has been scaled in order to fit into the plot. Peak absorption $\alpha_L = 5$ on the edge. Zero detuning is at $5 \cdot 10^{14}$ Hz.

light is around 606nm and hence the angular frequency ω is in the order of 10^{15} rad/s and is multiplied by the derivative of the real refractive index. Since $n_r(\omega) < \omega \frac{dn_r(\omega)}{d\omega}$ a simplified expression for the group velocity is:

$$v_g(\omega_c) \approx \left. \frac{c}{\omega \frac{dn_r(\omega)}{d\omega}} \right|_{\omega_c} \tag{194}$$

So in the case of slow light the group velocity is inversely proportional to the derivative of the real refractive index. The ratio between the FWHM of the transmission peaks from Figure 22 and Figure 23 is roughly the same as the ratio between the group velocity for a cold cavity (for a cold cavity the derivative of the real refractive index is zero and hence: $v_g = c/n_{host}$) and the group velocity in Figure 24b. When studying Figure 24b in more detail note that the group velocity is much lower near the edges of the spectral hole (the edges of the spectral hole are just outside the x-axis values at ± 10 MHz) and hence the cavity transmission peak will be smaller near the edges of the spectral hole. This effect can be seen by comparing the FWHM of the transmission cavity peaks between Figure 23 and Figure 25.

C. Spectral hole together with the AFC protocol

In a paper by Mikael Afzelius and Christoph Simon the derivations in the second half of the paper assumes that the cavity is on resonance for the frequencies of interest. With this assumption they show that the efficiency can be as high as 92% where the efficieny is only limited by the finesse of the comb. While this sounds promising the question remains whether this assumption is true or not. And if it's true what condition must hold for the absorption profile. In the following some results will be shown that investigates this assumption. To obtain 92% efficiency the finesse of the frequency comb should be equal to 10 and the single pass effective absorption (optical depth)

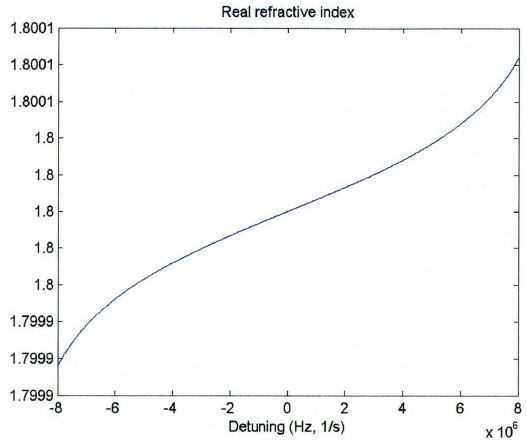

(a) Real refractive index (calculated by Eq. (177))

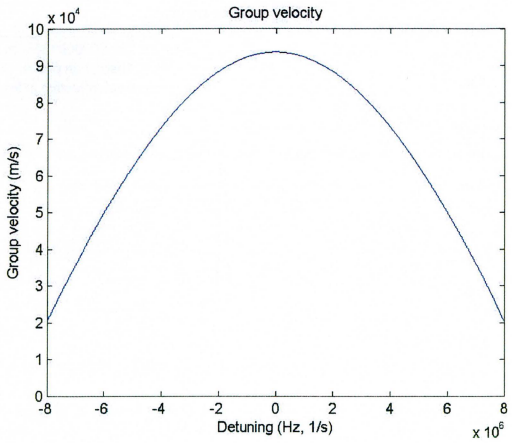

(b) Group velocity (calculated by Eq. (190))

FIG. 24: Numerical results for the real refractive index and the group velocity at the center of the spectral hole in Figure 23. Zero detuning is at $5 \cdot 10^{14}$ Hz.

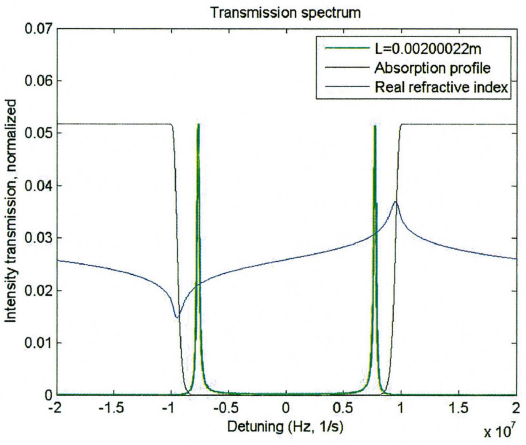

(a) Transmission spectrum

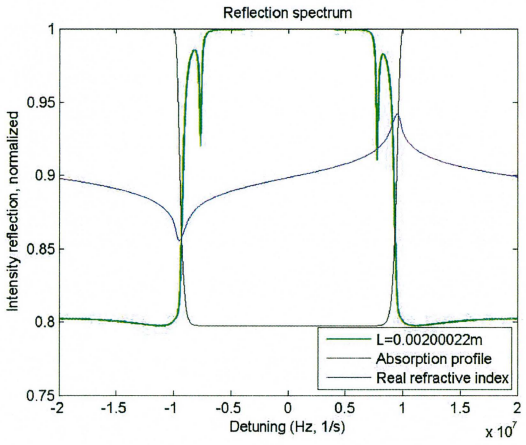

(b) Reflection spectrum

FIG. 25: Simulation of a cavity with a spectral hole present inside the medium. The spectral hole is represented as a supergaussian and the width is almost 20 MHz. The length of the crystal is set to $L = 0.00200022$m. The real refractive index and absorption profile has been scaled in order to fit into the plot. Peak absorption $\alpha_L = 5$ on the edge. Zero detuning is at $5 \cdot 10^{14}$ Hz. The group velocity is lower near the edge of the spectral hole this is the reason for the difference in FWHM of the transmission peaks between this figure and Figure 23.

should be $\alpha_L^{effective} = 0.1$. This means that the absorption of the AFC peaks should be set to $\alpha_L = 1$ ([35], p. 3-4).
At the Quantum information group in Lund the AFC peaks are made by initially burn a spectral hole. When the spectral hole has been created some ions are sent back into the spectral hole in such a way that they are forming an atomic frequency comb (AFC). A theoretical example of how the absorption profile might look like after this procedure is shown in Figure 26.

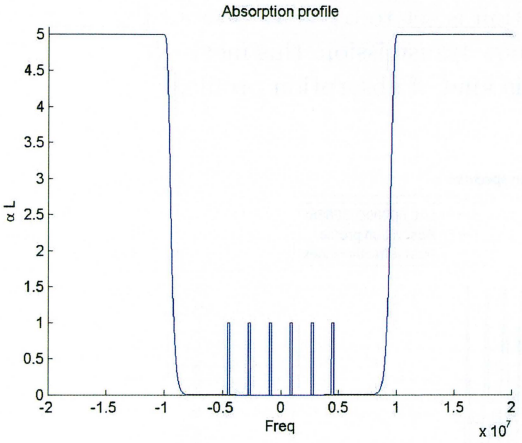

FIG. 26: AFC peaks are put back into a spectral hole. Example of the absorption profile with the AFC protocol, finesse=10, number of peaks=6. Peak absorption $\alpha_L = 5$ on the edge.

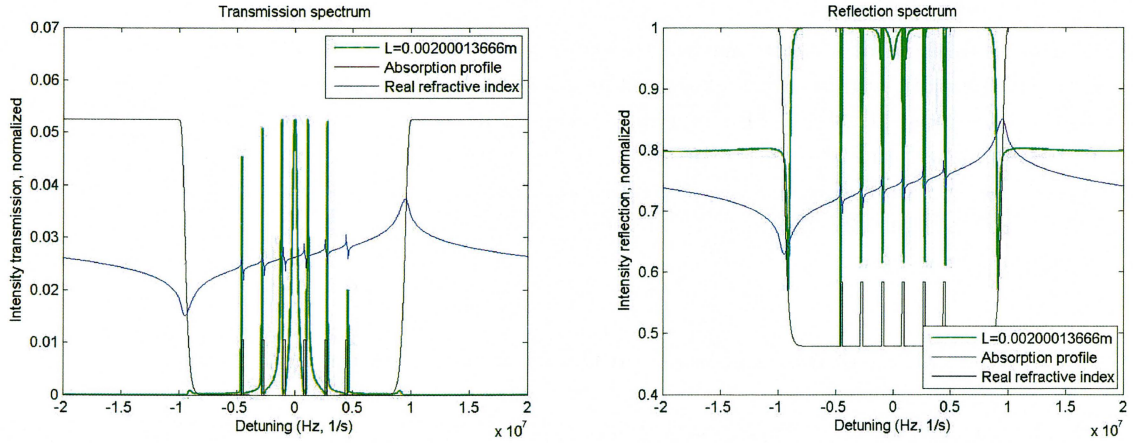

(a) Transmission spectrum

(b) Reflection spectrum

FIG. 27: Simulation of a cavity with a spectral hole together with the AFC protocol inside the medium, finesse=10, number of peaks=6. The spectral hole is represented as a supergaussian and the width is almost 20 MHz. The length of the crystal is set to $L = 0.00200013666$ m. The real refractive index and absorption profile have been scaled in order to fit into the plot. Peak absorption $\alpha_L = 5$ on the edge. Zero detuning is at $5 \cdot 10^{14}$ Hz. Note that all values are the same as in Figure 23 except that there are now AFC peaks present.

By looking at the transmission spectrum it will be possible to some extent figure out what conditions and changes that must be done to the absorption profile in order to be on resonance.

From Figure 27a it can be seen that only the two peaks in the middle seems to be on resonance with the cavity. The result of this can be seen in Figure 27b where the frequencies in between the outermost AFC peaks are more or less 100% reflected. One effect that is important to note is that the AFC peaks themself change the real refractive index (due to the Kramers-Kronig relations) and thereby create resonance for some frequencies near themselfs. This can be seen from Figure 27a where there are some narrow transmission peaks just beside the AFC peaks.
A way to enhance the resonance around the AFC peaks is to lower the edges of the pit. In Figure 28 the edges peak absorption is set to $\alpha_L = 1$. Now in Figure 28a it can be seen that in between the AFC peaks there are now transmission, this means that the resonance condition is more or less completely fulfilled for this kind of absorption profile.

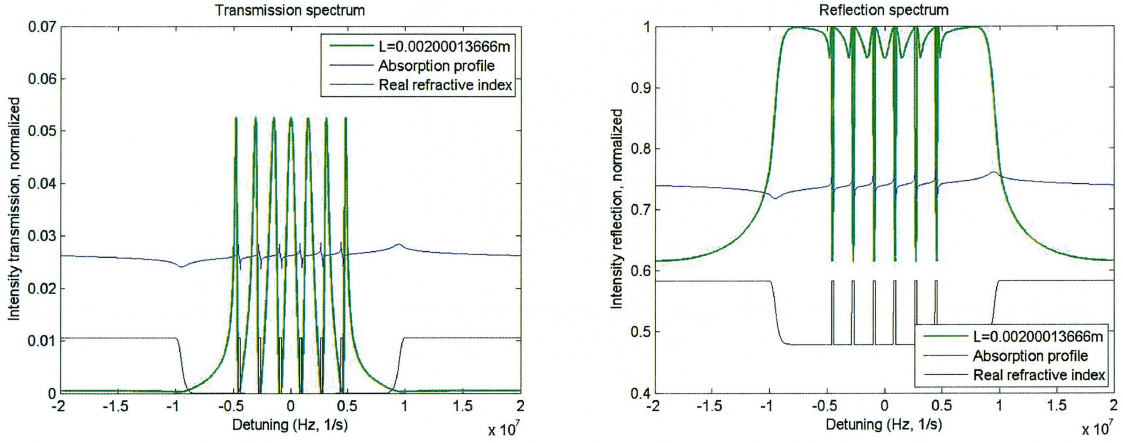

(a) Transmission spectrum

(b) Reflection spectrum

FIG. 28: Simulation of a cavity with a spectral hole together with the AFC protocol inside the medium, finesse=10, number of peaks=6. The spectral hole is represented as a supergaussian and the width is almost 20 MHz. The length of the crystal is set to $L = 0.00200013666$ m. The real refractive index and absorption profile have been scaled in order to fit into the plot. Peak absorption $\alpha_L = 1$ on the edge. Zero detuning is at $5 \cdot 10^{14}$ Hz. Note that all values are the same as in Figure 27 except that the edges of the spectral hole are 5 times lower.

D. Comparsion between theoretical and experimental data

Despite the simplicity of this model it's the agreement with experimental data that matters. There are difficulties on the experimental side to determine all the parameters that are needed in the model. Many times experimentalists and theorists have to do intelligent guesses for a model to fit. This will be done for many cases in this section.

1. Cold cavity

In Figure 29 the experimental cold cavity transmission spectrum is compared with the one given by the model. The experimental data is scaled in height and therefore no units are given on the y-axis, only the shapes can be compared.

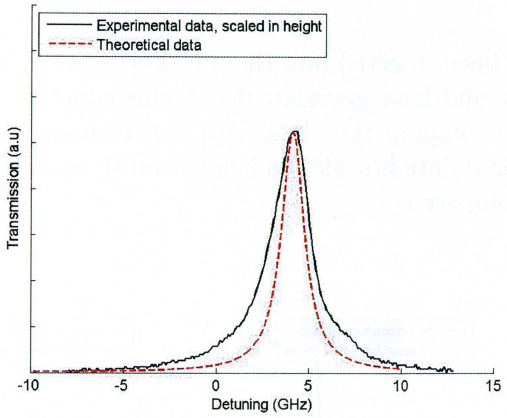

FIG. 29: Comparsion between theoretical and experimental data of the transmission spectrum for a cold cavity (only host medium present). The experimental data is scaled in height.

2. *Spectral hole*

The spectral hole for Pr:YSO can be made 18 MHz wide ([29], p. 25). The inhomogenous profile for a crystal inside a cavity can't easily be readout. The assumption that needs to be made is that the hole-burning procedure for a crystal inside a cavity is the same as the hole-burning procedure without a cavity. This is not necessarily the case. The 18 MHz spectral hole is shown in Figure 30a, the experimental comparsion is shown in Figure 30. The experimental data is scaled in height and therefore no units are given on the y-axis, only the shapes can be compared.

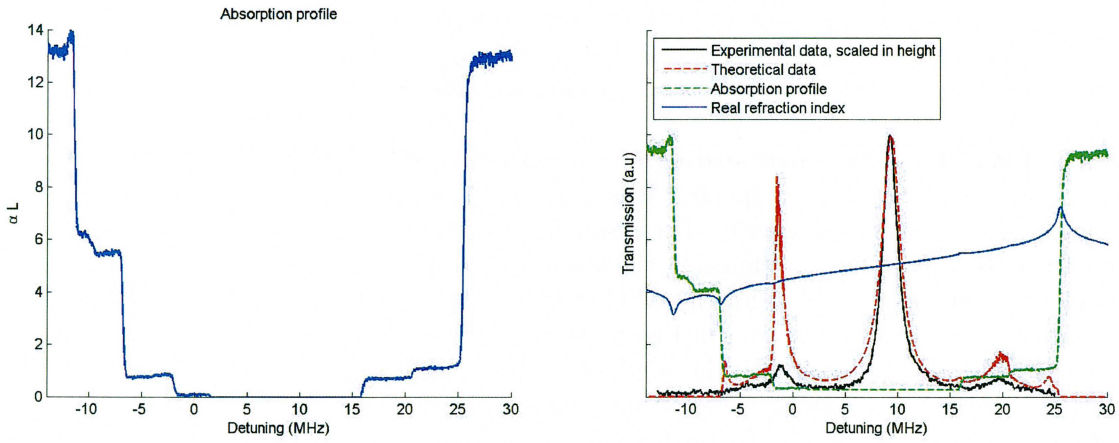

(a) Absorption profile

(b) Transmission spectrum

FIG. 30: Comparsion between theoretical and experimental data of the transmission spectrum for a spectral hole. The experimental data is scaled in height.

3. *AFC structure*

Four AFC peaks have been inserted into the pit. The AFC peaks for the theoretical model are assumed to look the same and have gaussian shape, this is not neccesarily the case in reality. It's in any case interesting to compare this data with experimental data. The result can be seen in Figure 31. The experimental data is scaled in height and therefore no units are given on the y-axis, only the shapes can be compared.

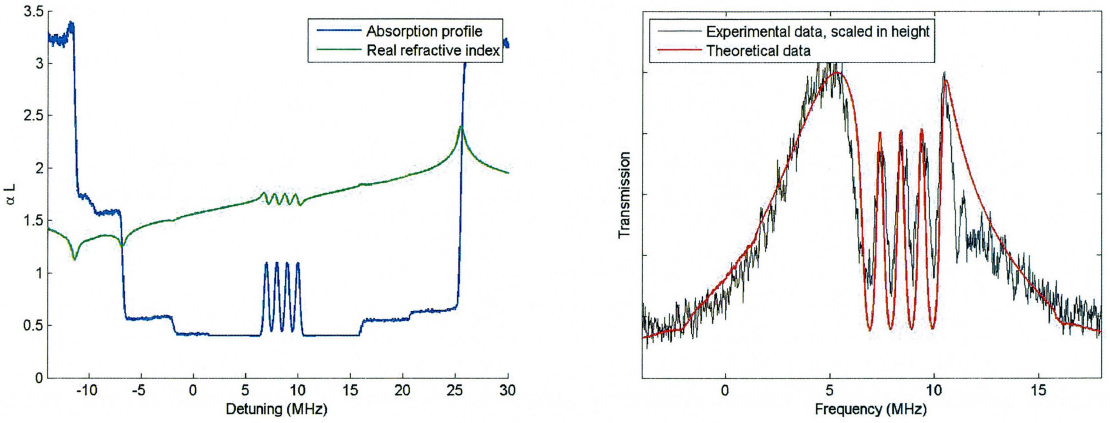

(a) Absorption profile

(b) Transmission spectrum, note that the x-axis has not the same scale as in Figure 31a.

FIG. 31: Comparsion between theoretical and experimental data of the transmission spectrum for a spectral hole together with four AFC peaks. The experimental data is scaled in height.

21. CONCLUSIONS

The FWHM and the mode spacing of the resonance peaks inside the cavity is reduced three orders of magnitude inside a spectral hole (Figure 30) compared to a cold cavity with only the host material present (Figure 29). The resonance peaks and mode spacing can in theory become as narrow as wanted by just changing the absorption of the edges of the spectral hole. A narrow resonance peak is not wanted for the AFC protocol. To get high efficiency all AFC peaks should be on resonance with the cavity. In Figure 27 and Figure 28 it can be seen that the edges of the spectral hole can't be to high. If the edges of the spectral hole is to high the derivative of the real refractive index become large. The FWHM of the resonance peak is inversely proportional to the derivative of the real refractive index (can be seen from Eq. (193) and Eq. (194)) and therefor it's important to have low absorption for the edges.
The length of the cavity can be changed in order to move the resonance peak in frequency this can be seen from Eq. (187) aswell as Figure 23. The length doesn't have to be changed much in order for the resonance peak to be moved a lot in frequency.
One interpretation for the FWHM and the mode spacing to change three orders of magnitude, is that it takes the pulse (relative to the group velocity) three order of magnitude longer time to go through the crystal compared to a cold cavity. This means that the cavity behaves as it was three orders of magnitude longer than it actually is under these circumstances. According to this interpretation the cavity of real length $L = 0.002$ m together with a 20 MHz spectral hole with

absorption $\alpha_L = 5$ on the edges give the same result as a cold cavity of length $L = 2$ m!
The experimental data is in fair agreement with the theoretical model. Many variables that hasn't been measured or can't be measured (the absorption profile can't be measured inside a cavity) on the experimental side. These have to be guessed and put into the theoretical model. Still it was possible to fit the experimental data well enough with this model for all cases shown in Figures 29, 30 and 31. The spectral hole (Figure 30a) made in a crystal without cavity seems to have the same structure as for a crystal inside a cavity. This might not be true for all cases but in this case it seems to be correct.

Part IX
Maxwell-Bloch cavity simulations

22. THEORY

In this section a more advanced theory will be derived compared to Section 19. The equations are basically an extension of the semi-classical MB equations from Section VI where a cavity is included. The theory is based on derivations from Siegman's "LASERS" [25], Lamb's "Theory of an Optical Maser" [43] and Lei Stone Meng Ph. D. thesis [44].

A. Cavity decay constant

A cavity with decay constant due to losses from two mirrors can be derived as follows. The decay constant is defined as the inverse time at the point when the initial intensity of a field is reduced by a factor of e^{-1} and hence

$$I(\tau) = I_0 e^{-1} \tag{195}$$
$$\gamma = 1/\tau \tag{196}$$

where I_0 is the initial intensity, τ is the time it takes for the intensity to decrease a factor of e^{-1} and γ is the decay constant. Suppose that the two mirrors have reflectivity R_1 resp. R_2. For a certain point in time t the intensity is decreased as

$$I(t) = I_0 \cdot (R_1 R_2)^q \tag{197}$$
$$q = \frac{t}{T} \tag{198}$$

where q is the number of round-trips that have been done and T is the time it takes to make one round-trip. By putting Eq. (195) equal to Eq. (197) the decay constant can be extracted.

$$(R_1 R_2)^{\tau/T} = e^{-1} \tag{199}$$
$$\frac{\tau}{T}\ln(R_1 R_2) = -1 \tag{200}$$
$$\gamma = \frac{1}{\tau} = \frac{1}{T}\ln(\frac{1}{R_1 R_2}) \tag{201}$$

The total cavity decay constant for a cavity with one partially transparent mirror and one 100% reflection mirror is ([25], p. 935)

$$\gamma_c^{total} = \gamma_0 + \gamma_1 = 2\alpha_0 c + \frac{1}{T}\ln(1/R_1) \tag{202}$$

where $\gamma_0 := 2\alpha_0 c$ is the internal power losses in a real optical cavity, T is the round-trip time and R_1 is the relfectivity of the partially transparent mirror.
In the case of two partially transparent mirrors (with reflectivity R_1 resp. R_2) and neglecting the internal power losses ($\alpha_0 = 0$) the cavity decay constant as Eq. (201) is

$$\gamma_c = \frac{1}{T}\ln(\frac{1}{R_1 R_2}) = \frac{1}{T}\ln(1/R_1) + \frac{1}{T}\ln(1/R_2) = \gamma_1 + \gamma_2 \tag{203}$$

and hence the total decay constant is the sum of both mirrors decay constants γ_1 and γ_2.
The time it takes for a round-trip in a cold cavity (only host medium present) can be expressed as a function of the speed of light in the medium and the length of the cavity,

$$T = \frac{2nL}{c} \tag{204}$$

where c is the speed of light in vaccum, n is the refractive index of the host medium and the factor of 2 comes from the fact that it's a round-trip.

B. Derivation of the Maxwell-part for a cavity

The field inside the cavity will be treated classically by Maxwell's equations in SI units. Starting of from Eq. (116) in one spatial dimension,

$$\frac{d^2E}{dz^2} - \mu\sigma\frac{dE}{dt} - \frac{n^2}{c^2}\frac{d^2E}{dt^2} = \mu\frac{d^2P}{dt^2} \tag{205}$$

The polarization P will basicly be treated the same way as in the Maxwell-Bloch equations. For a two-level atom ensemble it's the r_x and r_y components of the Bloch vector that determines the electric polarization. The Bloch vector evolves according to the Bloch equations, which are derived in Section 12 and Section 13. In the following the Maxwell-Bloch equations will be expanded and modified so that the equations can describe the evolution of a 2-level system with a host medium in a cavity.
In the following a vital assumption to simplify the equations will be done, that is to expand the electric field and the polarization as ([25], p. 924)

$$E(z,t) = \sum_n E_n(t)u_n(z) \tag{206}$$

$$P(z,t) = \sum_n P_n(t)u_n(z) \tag{207}$$

where $E_n(t)$ and $P_n(t)$ are coefficients that only depends on time, $u_n(z)$ are orthogonal eigenmodes of a cold cavity of length L (only host medium present). Strictly speaking the terms $E_n(t)$ and $P_n(t)$ should be derived by:

$$E_n(t) = \frac{1}{v}\int_0^L u_n^*(z)E(z,t)dz \tag{208}$$

$$P_n(t) = \frac{1}{v}\int_0^L u_n^*(z)P(z,t)dz \tag{209}$$

where v is a normalization constant given that the cavity is defined from 0 to L. In the theory developed by Lamb [43] the Eq. (208) and Eq. (209) are calculated more carefully than in this thesis. In this thesis the derivation is simply assuming that $E_n(t)$ and $P_n(t)$ behaves similar to the MB equations without spatial dependency and no extra terms added from the inner product in Eq. (208) and Eq. (209). In some cases this will not be a good approximation.

The eigenmodes are functions that satisfy the Laplace equation

$$\left(\frac{d^2}{dz^2} + k_n^2\right) u_n(z) = 0 \tag{210}$$

$$u_n(0) = 0 \tag{211}$$

$$u_n(L) = 0 \tag{212}$$

where $k_n = \omega_n n/c$ are the eigenvalues and ω_n are the resonance frequencies for the cold cavity (with the host material). The solution to one-dimensional Laplace equation is

$$u_n(z) = sin(\frac{\pi n z}{L}) \tag{213}$$

for n=1,2,... .
Inserting Eq. (206) and Eq. (207) into Eq. (205) gives:

$$\sum_n \left(- k_n^2 E_n - \mu\sigma \frac{dE_n}{dt} - \frac{n^2}{c^2}\frac{d^2E_n}{dt^2}\right) u_n = \mu \sum_n \frac{d^2P_n}{dt^2} u_n \tag{214}$$

$$\Leftrightarrow \tag{215}$$

$$\sum_n \left(\frac{d^2E_n}{dt^2} + \gamma_c \frac{dE_n}{dt} + w_n^2 E_n \right) u_n = -\frac{1}{\epsilon n^2} \sum_n \frac{d^2P_n}{dt^2} u_n \tag{216}$$

where $\gamma_c = \sigma/(n^2\epsilon)$ is the cavity decay constant. Note that since u_n is an orthogonal basis and it's possible to project Eq. (216) onto an arbitrary u_n. Therefor every term in the sum can be treated separately as

$$\frac{d^2E_n}{dt^2} + 2\gamma_c \frac{dE_n}{dt} + w_n^2 E_n = -\frac{1}{\epsilon n^2}\frac{d^2P_n}{dt^2} \tag{217}$$

In the following only one longitudal mode is going to be used, so the subscript n is going to be dropped:

$$\frac{d^2E}{dt^2} + \gamma_c \frac{dE}{dt} + w_c^2 E = -\frac{1}{\epsilon n^2}\frac{d^2P}{dt^2} \tag{218}$$

where the resonance frequency $\omega_c := \omega_n$.
Now suppose the cavity has two transparent mirrors and the decay constant is defined as $\gamma_c = \gamma_1 + \gamma_2$ (from Eq. (203)). In addition an external incoming field from one side will be added. The equation of motion is now

$$\frac{d^2E}{dt^2} + \gamma_c \frac{dE}{dt} + w_c^2 E = -\frac{1}{\epsilon n^2}\frac{d^2P}{dt^2} + K_1 \frac{d\xi_{in}}{dt} \tag{219}$$

where ξ_{in} is the incoming field and $K_1 = \sqrt{1 - R_1}\frac{c}{nL}$ is the loss due to the first mirror ([44] p. 6). Note that by just inserting a field ξ_{in} into the equation is an assumption that might not hold for all cases. One typical situation where this assumption doesn't hold is when the cavity field and in the incoming field modes doesn't match.
The electric field is now written in terms of Rabi frequencies similar to Eq. (79):

$$E = \frac{\hbar}{2\mu_{ge}} e^{i\omega_L t}(\Omega_r + i\Omega_i) + c.c. \tag{220}$$

First Eq. (220) is inserted into Eq. (219)

$$\frac{\hbar}{2\mu_{ge}}\left(\frac{d^2}{dt^2}+\gamma_c\frac{d}{dt}+\omega_c^2\right)(e^{i\omega_L t}(\Omega_r+i\Omega_i))+c.c.=-\frac{1}{\epsilon n^2}\frac{d^2P}{dt^2}+K_1\frac{d\xi_{in}}{dt} \tag{221}$$

where ω_L is the laser frequency. The left-hand side of Eq. (221) will be developed separately:

$$\frac{\hbar}{2\mu_{ge}}\left(\frac{d^2}{dt^2}+\gamma_c\frac{d}{dt}+\omega_c^2\right)e^{i\omega_L t}(\Omega_r+i\Omega_i)+c.c.= \tag{222}$$

$$e^{i\omega_L t}\frac{\hbar}{2\mu_{ge}}\left(\frac{d^2}{dt^2}+(2i\omega_L+\gamma_c)\frac{d}{dt}+\omega_n^2-\omega_L^2+i\omega_L\gamma_c\right)(\Omega_r+i\Omega_i)+c.c. \tag{223}$$

SVEA (Slowly Varying Envelope Approximation) will be applied in the same manner as Eq. (120) together with the assumption that
$|\omega_n-\omega_L|\ll\omega_L$. Then the following inequalities are obtained ([25], p. 925-947),

$$\Omega''_{r/i}\ll\omega_L\Omega'_{r/i}\ll\omega_L^2\Omega_{r/i} \tag{224}$$

$$\gamma_c\Omega'_{r/i}\ll\gamma_c\omega_L\Omega_{r/i} \tag{225}$$

$$\omega_c^2-\omega_L^2=(\omega_c+\omega_L)(\omega_c-\omega_L)\approx 2\omega_L(\omega_c-\omega_L) \tag{226}$$

These inequalities turns Eq. (223) into

$$\frac{\hbar}{2\mu_{ge}}\left(2i\omega_L\frac{d}{dt}+2\omega_L(\omega_c-\omega_L)+i\omega_L\gamma_c\right)e^{i\omega_L t}(\Omega_r+i\Omega_i)+c.c. \tag{227}$$

The polarization is expressed almost the same way as in Eq. (133):

$$P(z,t)\;=\;\frac{1}{4\pi}N\int_{-\infty}^{+\infty}g(\Delta)((r_x+ir_y)e^{i(\omega_L t)}\mu_{ge}^*+c.c.)d\Delta \tag{228}$$

The external field is written as:

$$\xi_{in}=\frac{\hbar}{2\mu_{ge}}e^{i\omega_L t}(\Upsilon_r^{in}+i\Upsilon_i^{in})+c.c. \tag{229}$$

where Υ_r^{in} and Υ_i^{in} are the real and imaginary Rabi frequencies of the incoming field.
SVEA will be used for the polarization exactly as in Eq. (137).
The right-hand side of Eq. (221) will now be developed and SVEA gives: $\Upsilon'_{r/i}\ll\omega_L\Upsilon_{r/i}$

$$-\frac{1}{\epsilon n^2}\frac{d^2P}{dt^2}+K_1\frac{d\xi_{in}}{dt}= \tag{230}$$

$$-\omega_L^2\frac{1}{4\pi\epsilon n^2}Ne^{i\omega_L t}\int_{-\infty}^{+\infty}g(\Delta)(r_x+ir_y)\mu_{ge}^*d\Delta+e^{i\omega_L t}K_1\frac{\hbar}{2\mu_{ge}}\left(\frac{d}{dt}+i\omega_L\right)(\Upsilon_r^{in}+i\Upsilon_i^{in})+c.c.=^{SVEA}$$

$$-\omega_L^2\frac{1}{4\pi\epsilon n^2}Ne^{i\omega_L t}\int_{-\infty}^{+\infty}g(\Delta)(r_x+ir_y)\mu_{ge}^*d\Delta+e^{i\omega_L t}K_1\frac{i\hbar\omega_L}{2\mu_{ge}}(\Upsilon_r^{in}+i\Upsilon_i^{in})+c.c. \tag{231}$$

Now set Eq. (227) equal to Eq. (231)

$$\frac{\hbar}{2\mu_{ge}}\left(2i\omega_L\frac{d}{dt}+2\omega_L(\omega_c-\omega_L)+i\omega_L\gamma_c\right)e^{i\omega_L t}(\Omega_r+i\Omega_i)+c.c.= \tag{232}$$

$$-\omega_L^2\frac{1}{4\pi\epsilon n^2}Ne^{i\omega_L t}\int_{-\infty}^{+\infty}g(\Delta)(r_x+ir_y)\mu_{ge}^*d\Delta+e^{i\omega_L t}K_1\frac{i\hbar\omega_L}{2\mu_{ge}}(\Upsilon_r^{in}+i\Upsilon_i^{in})+c.c. \tag{233}$$

$$\Leftrightarrow \tag{234}$$

$$\left(\frac{d}{dt}+i(\omega_L-\omega_c)+\frac{\gamma_c}{2}\right)e^{i\omega_L t}(\Omega_r+i\Omega_i)+c.c.= \tag{235}$$

$$i\frac{\omega_L|\mu_{ge}|^2N}{4\pi\epsilon n^2\hbar}e^{i\omega_L t}\int_{-\infty}^{+\infty}g(\Delta)(r_x+ir_y)d\Delta+e^{i\omega_L t}\frac{K_1}{2}(\Upsilon_r^{in}+i\Upsilon_i^{in})+c.c. \tag{236}$$

The next step is to extract the real and the imaginary part aswell as the term $e^{i\omega_L t}$ into two different equations.

$$\frac{d\Omega_r}{dt}-(\omega_L-\omega_c)\Omega_i+\frac{\gamma_c}{2}\Omega_r=-\frac{\alpha c}{2\pi n}\int_{-\infty}^{+\infty}g(\Delta)r_y d\Delta+\frac{K_1}{2}\Upsilon_r^{in} \tag{237}$$

$$\frac{d\Omega_i}{dt}+(\omega_L-\omega_c)\Omega_r+\frac{\gamma_c}{2}\Omega_i=\frac{\alpha c}{2\pi n}\int_{-\infty}^{+\infty}g(\Delta)r_x d\Delta+\frac{K_1}{2}\Upsilon_i^{in} \tag{238}$$

where $\alpha=\frac{|\mu_{ge}|^2\omega_L N}{2c\hbar n\epsilon}$ is called the absorption coefficient.

C. The complete equations

The postulates of quantum mechanics are only valid for a closed system. When performing an experiment the system 2-level atom model is not a closed system. A quick fix to solve this problem is to introduce two phenomenological decay constants T_1 and T_2. $1/T_1$ is the rate for the population term of the atom to relax toward equilibrium. $1/T_2$ is the rate at which the coherence will decrease. The complete equations is found by adding Eq. (237) and Eq. (238) that describes the macroscopic polarization and the Bloch equations from Eq. (100)-(102), this final set of equations:

$$\frac{dr_x(t,\Delta)}{dt}=-\Delta r_y(t,\Delta)-\Omega_i(t)r_z(t,\Delta)-\frac{r_x(t,\Delta)}{T_2} \tag{239}$$

$$\frac{dr_y(t,\Delta)}{dt}=\Delta r_x(t,\Delta)+\Omega_r(t)r_z(t,\Delta)-\frac{r_y(t,\Delta)}{T_2} \tag{240}$$

$$\frac{dr_z(t,\Delta)}{dt}=\Omega_i(t)r_x(t,\Delta)-\Omega_r(t)r_y(t,\Delta)-\frac{1+r_z(t,\Delta)}{T_1} \tag{241}$$

$$\frac{d\Omega_r(t)}{dt}-(\omega_L-\omega_c)\Omega_i(t)+\frac{\gamma_c}{2}\Omega_r(t)=-\frac{\alpha c}{2\pi n}\int_{-\infty}^{+\infty}g(\Delta)r_y(t,\Delta)d\Delta+\frac{K_1}{2}\Upsilon_r^{in}(t) \tag{242}$$

$$\frac{d\Omega_i(t)}{dt}+(\omega_L-\omega_c)\Omega_r(t)+\frac{\gamma_c}{2}\Omega_i(t)=\frac{\alpha c}{2\pi n}\int_{-\infty}^{+\infty}g(\Delta)r_x(t,\Delta)d\Delta+\frac{K_1}{2}\Upsilon_i^{in}(t) \tag{243}$$

The reflected/transmitted fields out of the material are assumed to be (similar to expression in [9], p. 299, but with a phase shift of the reflected part of the incoming field):

$$\Omega_r^{refl} = \sqrt{1-R_0}\sqrt{R_2}\Omega_r - \sqrt{R_0}\Upsilon_r^{in} \tag{244}$$
$$\Omega_i^{refl} = \sqrt{1-R_0}\sqrt{R_2}\Omega_i - \sqrt{R_0}\Upsilon_i^{in} \tag{245}$$
$$\Omega_r^{trans} = \sqrt{1-R_2}\Omega_r \tag{246}$$
$$\Omega_i^{trans} = \sqrt{1-R_2}\Omega_i \tag{247}$$

where R_0 is the reflectivity for the first mirror and R_2 is the reflectivity for the second mirror of the cavity. Note that the reflected/transmitted fields is not valid for all choices to R_0 and R_2, a small investigation about this is done in Subsection 22 D.

D. Regime where MB cavity model is valid

Comparsion with the equations derived in Subsection 19 A will be done for one simple example in order to see in what regime the MB cavity model is valid. The MB cavity equation will be solved in the steady state $\frac{d\Omega_r}{dt} = 0$ on resonance $\omega_L = \omega_c$. The Rabi frequency is assumed to only have a real part and no ions are present $\alpha = 0$ (cold cavity with only host medium present). Starting from Eq. (242):

$$\frac{d\Omega_r}{dt} - (\omega_L - \omega_c)\Omega_i + \frac{\gamma_c}{2}\Omega_r = -\frac{\alpha c}{2\pi n}\int_{-\infty}^{+\infty} g(\Delta) r_y d\Delta + \frac{K_1}{2}\Upsilon_r^{in} \tag{248}$$
$$\Rightarrow \tag{249}$$
$$\frac{\gamma_c}{2}\Omega_r = \frac{K_1}{2}\Upsilon_r^{in} \tag{250}$$
$$\Leftrightarrow \tag{251}$$
$$\Omega_r = \frac{K_1}{\gamma_c}\Upsilon_r^{in} \tag{252}$$

Inserting Eq. (252) into Eq. (246) and Eq. (244):

$$\Omega_r^{refl} = \left(\sqrt{1-R_0}\sqrt{R_2}\frac{K_1}{\gamma_c}\Upsilon_r^{in} - \sqrt{R_0}\right)\Upsilon_r^{in} = \left(\frac{\sqrt{1-R_0}\sqrt{1-R_1}\sqrt{R_2}}{\ln(\frac{1}{\sqrt{R_1 R_2}})} - \sqrt{R_0}\right)\Upsilon_r^{in} \tag{253}$$

$$\Omega_r^{trans} = \sqrt{1-R_2}\frac{K_1}{2\gamma_c}\Upsilon_r^{in} = \frac{\sqrt{1-R_2}\sqrt{1-R_1}}{\ln(\frac{1}{r_1 r_2})}\Upsilon_r^{in} \tag{254}$$

Finally taking the ratio between the outgoing intensity and initial intensity,

$$T_c^{MB} = \left|\frac{t_2 t_1}{\ln(\frac{1}{r_1 r_2})}\right|^2 \tag{255}$$

$$R_c^{MB} = \left| -r_0 + \frac{t_0 t_1 r_2}{\ln(\frac{1}{r_1 r_2})}\right|^2 \tag{256}$$

where $r_0 = \sqrt{R_0}$, $t_0 = \sqrt{1-R_0}$, $t_1 = \sqrt{1-R_1}$, $t_2 = \sqrt{1-R_2}$, $r_1 = \sqrt{R_1}$ and $r_2 = \sqrt{R_2}$.
This is now going to be compared to Eq. (184) and Eq. (185) given that there is no absorption

$n_i = 0$ and that the resonance condition is fulfilled $2kL = 2\pi$,

$$T_c = \left| \frac{t_1 t_2}{1 - r_1 r_2} \right|^2 \tag{257}$$

$$R_c = \left| -r_0 + \frac{t_1 r_2 t_0}{1 - r_1 r_2} \right|^2 \tag{258}$$

The serie expansion of $ln(x)$ is [45]

$$ln(x) = (x-1) - \frac{(x-1)^2}{2} + \frac{(x-1)^3}{3} - \frac{(x-1)^4}{4} + ... \tag{259}$$

$$\ln(\frac{1}{r_1 r_2}) = (1 - r_1 r_2) - \frac{(1 - r_1 r_2)^2}{2} + \frac{(1 - r_1 r_2)^3}{3} - \frac{(1 - r_1 r_2)^4}{4} + ... \tag{260}$$

where $-1 \leq x \leq 1$. The regime where Eq. (255) and Eq. (257) resp. Eq. (256) and Eq. (258) are almost equal can now be found if $1 - r_1 r_2 \approx 0$ and hence the MB cavity model is almost equal to the interference equations if the reflectivities are close to one.

E. Numerical simulations with the Runge-kutta method

The Runge-kutta method can be used to numerically solve the equations in the above section. In the numerical model $g(\Delta)$ can't be defined from $-\infty$ to $+\infty$, therefore a different α will be used called α_0. $\alpha_0 := \alpha(\omega_0)/g(\omega_0)$ where $g(\omega_0) \neq 0$ ([22], p. 50).

F. Impedance matching condition for the AFC protocol

The impedance matching condition is fulfilled when the absorption of the material inside the cavity is matched to the transmission of the coupling mirror. This will in best case lead to total aborption. Total absorption of an incoming photon is the first vital step towards a high efficient quantum memory. Given that the reflectivity is chosen to be $R_1 = 0.98$ for the first mirror and $R_2 = 0.9998$ for the second mirror gives the following impedance matching condition for a cavity that is on resonance:

$$e^{-\alpha_L}\sqrt{R_2} = \sqrt{R_1} \tag{261}$$

$$\Leftrightarrow \tag{262}$$

$$\alpha_L = ln(\sqrt{R_2/R_1}) \approx 0.01 \tag{263}$$

The AFC peaks should then have an effective absorption of $\alpha_L^{effective} \approx 0.01$. The peak absorption should then basically be the effective absorption multiplied by the finesse to reach the impedance matching condition [35].

G. Readout pulse

To be able to test the equations derived in this section against the equations in Section 20 the readout pulse is going to be defined. The purpose of the readout pulse is to get the transmission/reflection spectrum for every frequency. The idea is to do a linear frequency scan with a weak

Name	Value
t_0	$\sqrt{0.02}$
t_1	$\sqrt{0.02}$
t_2	$\sqrt{0.0002}$
r_0	$\sqrt{0.98}$
r_1	$\sqrt{0.98}$
r_2	$\sqrt{0.9998}$

TABLE II: Constants for MB cavity simulations.

pulse so that every time-step represent a particular frequency:

$$fs(t) = \omega_{start} + (\omega_{end} - \omega_{start})t/(t_{end}) \tag{264}$$

where $fs(t)$ is the linear frequency scan as a function of the time t. ω_{start} and ω_{end} are angular frequencies. The frequency scan starts at ω_{start} and stops at ω_{end} given that the pulse is sent in for a duration of t_{end}. The phase is defined to be the integral of the frequency [25]:

$$\varphi(t) = \int fs(t)dt = \omega_{start}t + (\omega_{end} - \omega_{start})t^2/(2t_{end})) \tag{265}$$

where $\varphi(t)$ is the phase that can be inserted into Eq. (51).

23. RESULTS AND DISCUSSION

The equations in Section 22 C are built up with many assumptions. In Subsection 22 D it was shown that for a cavity without atoms and with a frequency chosen such that there is resonance, only high reflectivities are a good regime for these equations. A simulation test will be done to see if this simulator produce the same result as the interference equations in Section 20 inside a spectral hole when the reflectivities are chosen to be high. If this holds, the next step is to try the AFC scheme by sending in a light pulse into the material. This wasn't possible to do with the interference equations. All results in this section will only be valid for one longitudal cavity mode and the decay constants for the Bloch equation $1/T_1$ and $1/T_2$ are put to zero if nothing else is noted. For all simulations concerning the interference simulator in this section some parameter will be constant, these are represented in Table II. For the MB simulator the length is chosen to be $L = 0.002$m, the refractive index $n = 1.0$. As can be seen in Table II, the reflectivity for the mirror for the incoming intensity is $R_1 = 0.98$ and the reflectivity for the mirror in the back of the crystal is chosen to be $R_2 = 0.9998$.

A. Spectral hole as a supergaussian

In the following a spectral hole from a supergauss function with a width of almost 20 MHz will be included inside the inhomogenous broadening. In Figure 32 the intereference simulator and MB cavity simulator output are shown for both the transmission and reflection part. The output from the equations in Section 22 C has been generated with a readout pulse described in Subsection 22 G.

The transmission spectrums coincide suprisingly well, while the reflection parts are a little bit

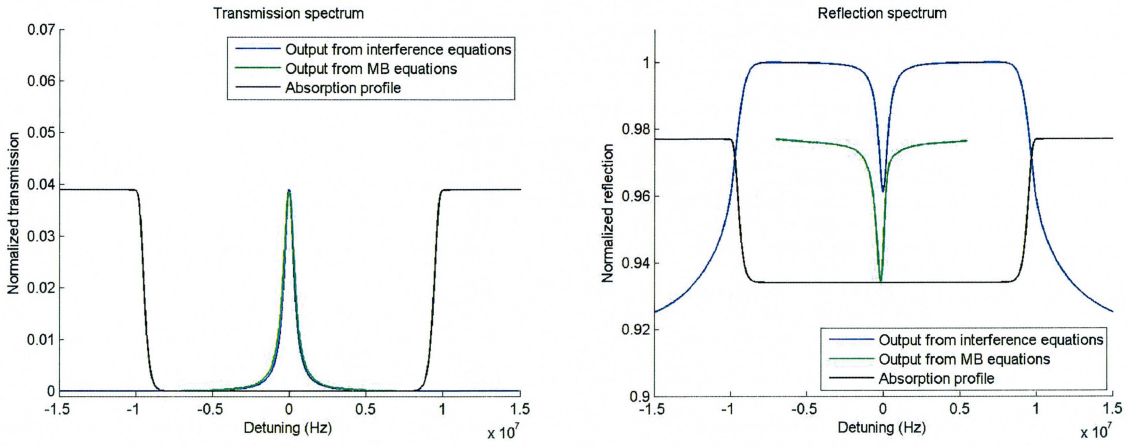

(a) Transmission spectrum

(b) Reflection spectrum

FIG. 32: Simulation of a cavity with a spectral hole present. The spectral hole is represented as a supergaussian and the width is almost 20 MHz. The length of the crystal for the interference simulator, from Section 20, is chosen so that the transmission peaks are centered in the spectral hole: $L = 0.002000103$ m. Peak absorption $\alpha_L = 0.5$ on the edge of the spectral hole. Zero detuning is at $5 \cdot 10^{14}$ Hz. The resonance frequency for the MB cavity model is chosen to be $\omega_c = \omega_L$, from Section 22 C (that is, the resonance frequency is chosen to be zero with respect to the detuning for the MB simulator). The graph with the MB equations is obtained by a readout pulse described in Subsection 22 G.

different from each other. The reflection spectrum in Figure 32b seems to be translated overall and the highest value is $R_1 = 0.98$ compared to the highest value of the interference simulator which is one. This error is non-wanted but as it's proportional to R_1 the claim in Subsection 22 D that the model coincide when the reflectivities are close to one seems still to be valid.

B. Spectral hole together with the AFC protocol

At the Quantum information group in Lund the AFC peaks are made by initially burn a spectral hole. When the spectral hole has been created some ions are sent back into the spectral hole in such a way that they are forming an atomic frequency comb (AFC). An example of how the absorption profile might look like after this procedure in theory is shown in Figure 26. In Figure 33 the output from the MB simulator and the interference simulator are shown. In Figure 33 there have been six AFC peaks inserted into the spectral hole. The "noise" from the MB output comes from the fact that the readout pulse excites the atoms inside the material. This leads to that the atoms send out coherent radiation for a short while after the excitation has occured. The mixing between the radiation from the atoms and the linear frequency scan creates this beating effect. This is an extreme effect in the reflection seen in Figure 33b, due to this the result with the interference simulator will not be shown. The transmission spectrums coincide fairly well. In Figure 34 the absorption on the edges of the spectral hole has decreased. The beating effect is still extreme for the reflection part, while the transmission spectrums look almost the same.

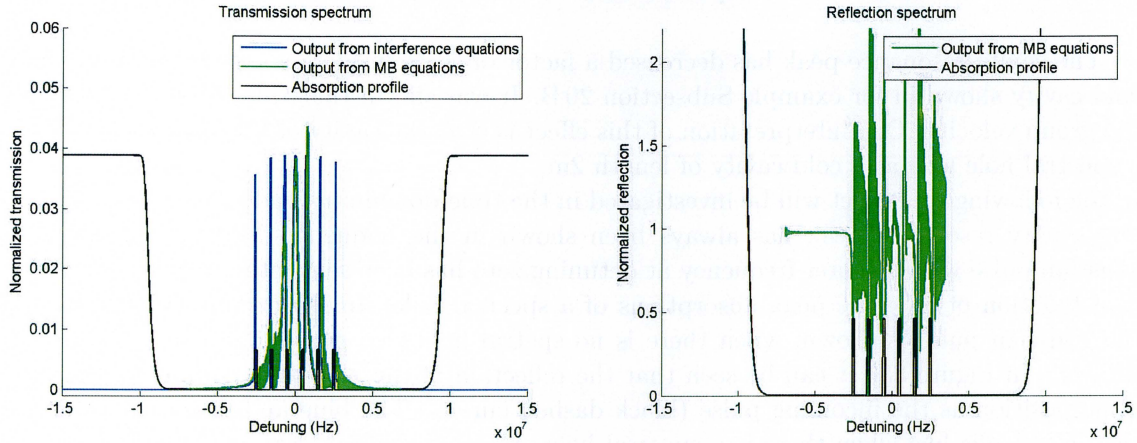

(a) Transmission spectrum (b) Reflection spectrum

FIG. 33: Simulation of a cavity with a spectral hole together with the AFC protocol, finesse=8.5, number of peaks=6. The spectral hole is represented as a supergaussian and the width is almost 20 MHz. The length of the crystal is set to $L = 0.002$m. Peak absorption $\alpha_L = 0.5$ on the edge. Zero detuning is at $5 \cdot 10^{14}$ Hz. The resonance frequency ω_c is chosen to be zero with respect to the detuning for the MB simulator. Note that all values are the same as in Figure 32 except that there are now AFC peaks present.

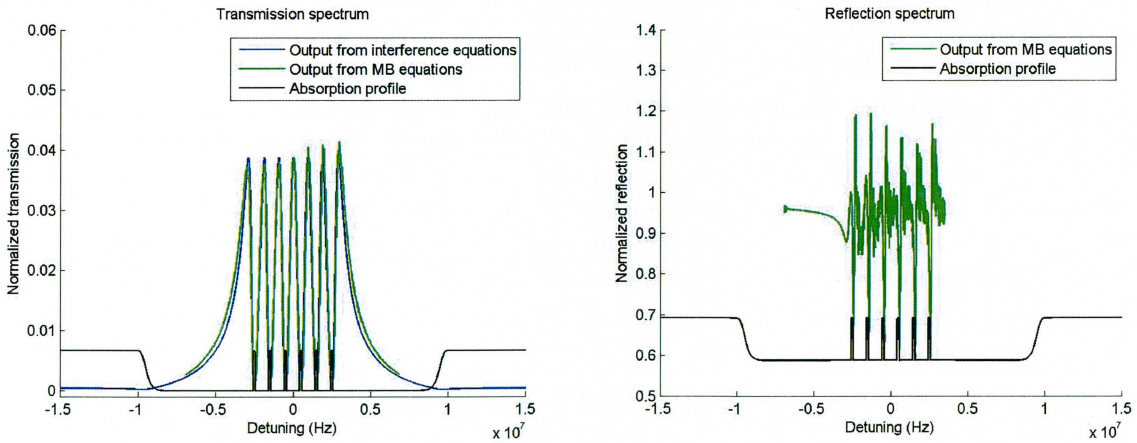

(a) Transmission spectrum (b) Reflection spectrum

FIG. 34: Simulation of a cavity with a spectral hole together with the AFC protocol, finesse=8.5, number of peaks=6. The spectral hole is represented as a supergaussian and the width is almost 20 MHz. The length of the crystal is set to $L = 0.002$m. Peak absorption $\alpha_L = 0.085$ on the edge. Zero detuning is at $5 \cdot 10^{14}$ Hz. The resonance frequency ω_c is chosen to be zero with respect to the detuning for the MB simulator.

C. Spectral hole and slow light effects

The cavity resonance peak has decreased a factor of three inside a spectral hole compared to a cold cavity shown in for example Subsection 20 B. It was shown that this effect was connected to the group velocity. One interpretation of this effect is that the cavity of length 2mm together with a spectral hole acts as a cold cavity of length 2m.
In the following this effect will be investigated in the time-domain instead of the frequency-domain (the cavity resonance peak has always been shown in the frequency-domain). In Figure 35 a gaussian pulse with a center frequency at detuning zero has been sent into a medium and is shown as a function of different peak absorptions of a spectral hole. In Figure 35c the transmission of the gaussian pulse is shown, when there is no spetral hole (red curve) the gaussian pulse is not delayed. In Figure 35b it can be seen that the reflection of the red curve is in almost exactly the same position as the incoming pulse (black dashed curve). The blue and green curves show how the pulse looks like when there is a spectral hole present. This is the time-domain version of the slow light effect. The intepretation is that it takes time to build up a field inside the cavity (just as if the cavity length was in order of 2 m). To clarify how this works Figure 36 shows the real Rabi frequencies multiplied by the transmission and reflection coefficients (this is the same as looking at Eq. (244) with $r_0 = \sqrt{R_0}$ and $t_0 = \sqrt{1 - R_0}$). The blue negative curve is the reflected field and the red curve is the field inside the cavity multiplied by the transmission coefficient out of the transparent mirror. Note that the red curve is delayed compared to the reflected field (blue curve) and by adding those curves the outgoing green curve is obtained. The square of the green curve in Figure 36 is shown as the green curve in Figure 35.

D. Spectral hole and slow light effects with an AFC structure

The first step that must be fulfilled in the making of a highly efficient quantum memory is to absorb as much of the incoming pulse as possible. Two examples will be shown that demonstrates how the edges of a spectral hole affects the storage of an incoming pulse. In Figure 37 the spetral hole and the AFC peaks have the same peak absorption. The peak absorption of the AFC structure is chosen such that the impedance matching condition holds, given that the structure is on resonance. The efficiency is above 80% which is fairly good for a quantum memory. In Figure 38 the peak absorption of the AFC peaks is such that the impedance matching condition holds, given that the structure is on resonance. The edges of the spectral hole has been increased compared to Figure 37. Total absorption of the incoming pulse is now not possible due to the slow light effects described in Subsection 23 C, this affects the efficiency of the quantum memory in a negative manner.

E. Efficiency for the AFC protocol together with a cavity

Two different cases will be shown to see how the absorption of the incoming field and the efficiency are affected. The incoming pulse is a gaussian with center around zero detuning ($\omega_L = 0$ Hz with respect to the detuning). In Figure 39 the first case is shown, the x-axis is the peak absorption of the edges of the spectral hole and the y-axis is the peak absorption of the AFC peaks (for example if the peak absorption of the AFC peaks is $\alpha_L = 0.085$ and the peak absorption of the AFC edges are $\alpha_L = 0.085$ the absorption profile in Figure 37a is used, if the peak absorption of the AFC peaks is $\alpha_L = 0.085$ and the peak absorption of the AFC edges are $\alpha_L = 0.5$ the absorption profile from Figure 38a is used). In Subsection 22 F it was shown that for reflectivity $R_1 = 0.98$,

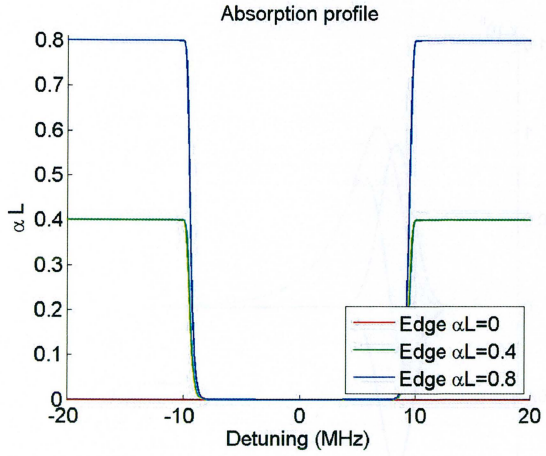

(a) Absorption profile

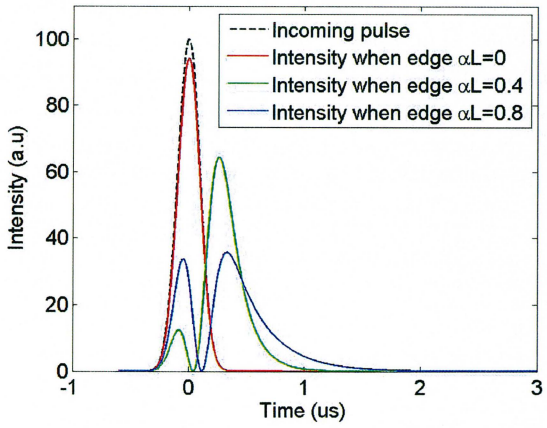

(b) Incoming pulse and reflected pulse

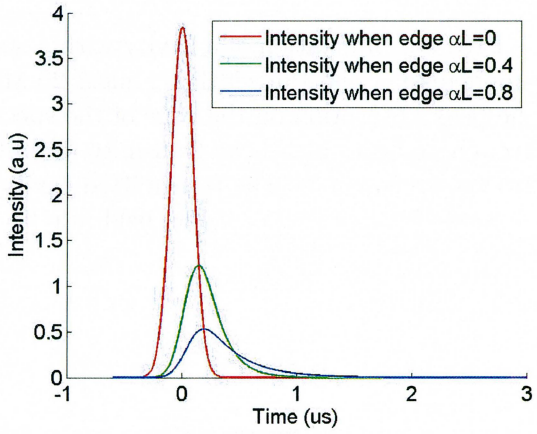

(c) Transmitted pulse

FIG. 35: Simulation of a cavity with a spectral hole. The spectral hole is represented as a supergaussian and the width is almost 20 MHz. The length of the crystal is set to $L = 0.002$ m. The slow light effects delays the buildup inside the cavity compared to a cold cavity.

the effective absorption should be approximately $\alpha_L^{effective} = 0.01$ with a finesse $F = 8.5$ the peak absorption becomes $\alpha_L^{peak} = \alpha_L^{effective} \cdot F = 0.085$.

The second case shown in Figure 40 shows different resonance frequencies ω_c on the x-axis . The incoming pulse and the AFC-structure are centered around zero detuning. The peak absorption edges of the spectral hole are constant and set to $\alpha_L = 0.17$.

To clarify how much the resonance frequency (ω_c) shifts the cavity peak inside the spectral hole a figure will be shown. The maximum resonance frequency used in Figure 40 was $\omega_c = 0.2GHz$ with respect to the detuning (note that $\omega_L = 0$ with respect to the detuning). In Figure 41 three different values of the resonance frequencies have been used together with an empty spectral hole (the AFC peaks are removed to avoid the beating effect).

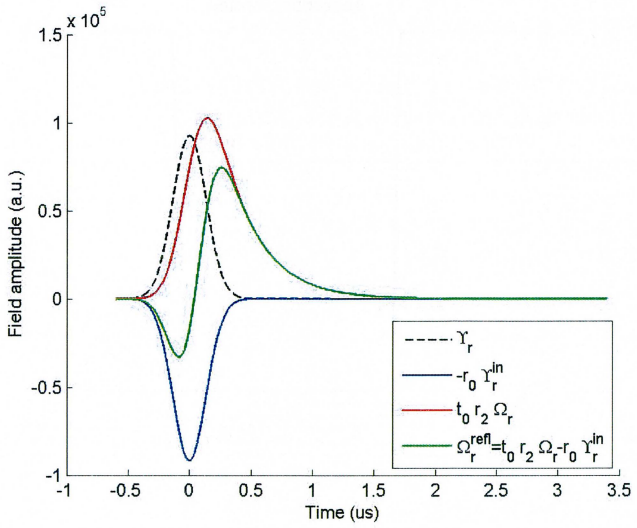

FIG. 36: Simulation of a cavity with a spectral hole. The spectral hole is represented as a supergaussian and the width is almost 20 MHz. The length of the crystal is set to $L = 0.002$ m. The peak absorption on the edge of the spectral hole are chosen to be $\alpha L = 0.4$. The field of the incoming reflection and the transmitted cavity field is shown separately and then added together as the green curve. The transmitted cavity field is not built up directly inside the cavity and hence the resulting outgoing field in reflection has both a negative and positive amplitude.

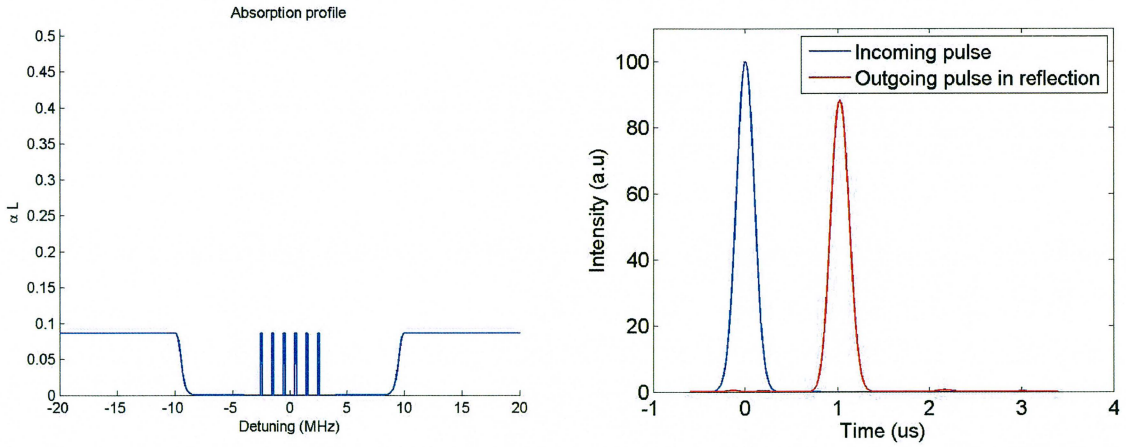

(a) Absorption profile

(b) Incoming pulse and reflected pulse

FIG. 37: Simulation of a cavity with a spectral hole together with the AFC protocol, finesse=8.5, number of peaks=6. The spectral hole is represented as a supergaussian and the width is almost 20 MHz. The length of the crystal is set to $L = 0.002$ m. Peak absorption $\alpha_L = 0.085$ on the edge. Zero detuning is at $5 \cdot 10^{14}$ Hz. The resonance frequency ω_c is chosen to be zero with respect to the detuning for the MB simulator.

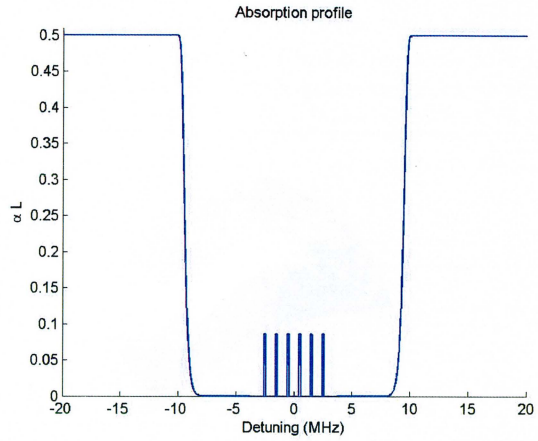

(a) Absorption profile

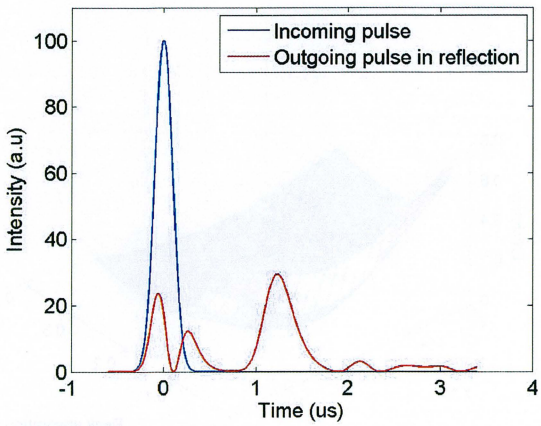

(b) Incoming pulse and reflected pulse

FIG. 38: Simulation of a cavity with a spectral hole together with the AFC protocol, finesse=8.5, number of peaks=6. The spectral hole is represented as a supergaussian and the width is almost 20 MHz. The length of the crystal is set to $L = 0.002$ m. Peak absorption $\alpha_L = 0.5$ on the edge. Zero detuning is at $5 \cdot 10^{14}$ Hz. The resonance frequency ω_c is chosen to be zero with respect to the detuning for the MB simulator.

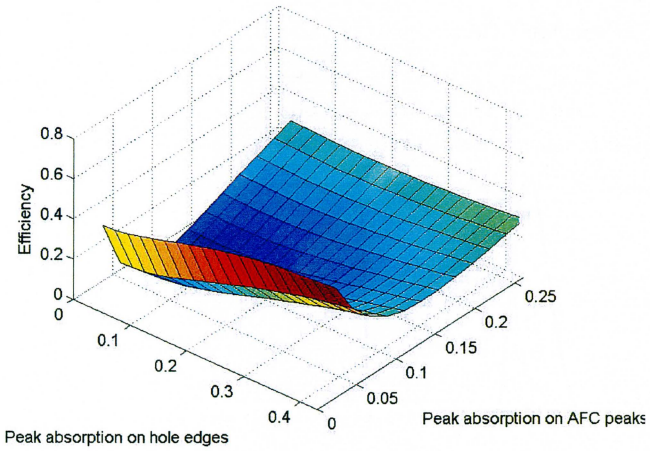

(a) Absorption; 0 means total absorption; 1 means no absorption

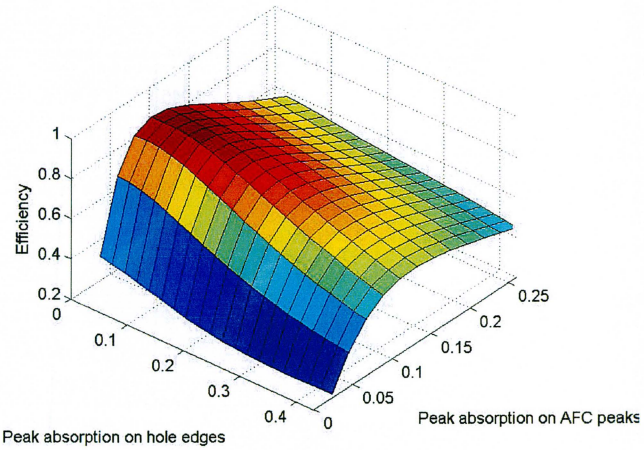

(b) Efficiency

FIG. 39: Efficiency for the outgoing stored pulse and absorption of incoming pulse shown as a function the peak absorption of the AFC peaks and peak absorption on the edges of the spectral hole. The spectral hole is represented as a supergaussian and the width is almost 20 MHz. The length of the crystal is set to $L = 0.002$ m. The resonance frequency is chosen to be zero with respect to the detuning.

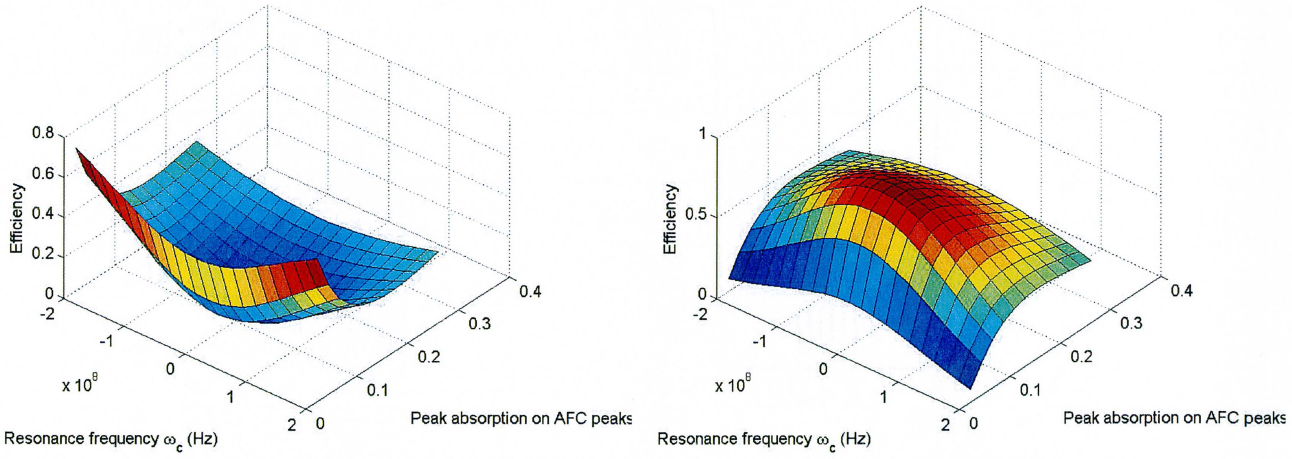

(a) Absorption; 0 means total absorption; 1 means no absorption

(b) Efficiency

FIG. 40: Efficiency for the outgoing stored pulse and absorption of incoming pulse shown as a function of the peak absorption of the AFC peaks and the resonance frequency ω_c. Finesse=8.5, number of peaks=6. The spectral hole is represented as a supergaussian and the width is almost 20 MHz. The length of the crystal is set to $L = 0.002$m. Peak absorption $\alpha_L = 0.017$ on the edge (ratio between the edge of the spectral hole and the AFC peaks = 2), peak absorption $\alpha_L = 0.085$ of the AFC peaks.

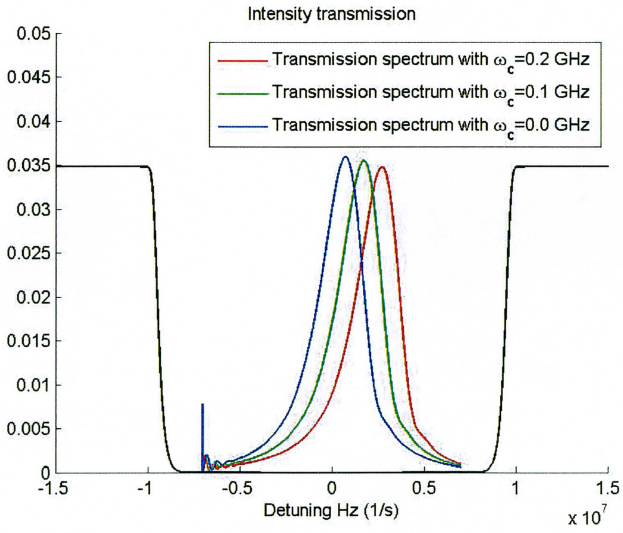

FIG. 41: Transmission spectrum for an empty spectral hole shows how much the cavity peak is shifted for different resonance frequencies. $\omega_c = 0.2$ GHz is the maximum resonance frequency with respect to the detuning that was used in Figure 40. The reason for the shift to be in order of MHz when the value of ω_c is in the order of GHz is due to the change in refractive index explained in Subsection 20 B.

24. CONCLUSIONS

In this section semi-classical equations to simulate a cavity with a medium inside have been derived. The equations in this section should by all means give rise the same effects as the interference equations derived in Section 19. The comparsion between the two simulators was shown in Figues: 32, 33 and 34. The transmission spectrums from the two simulators coincide fairly well. The reflection spectrum contains a lot of beating effects coming from the fact that the readout pulse excite population that sends out coherent radiation for a short while. The outcoming pulse is then a mix of radiation from the linear frequency scan and the ions.
In Figure 39 the absorption of the incoming field and the efficiency of the outgoing stored pulse were shown as a function of the peak absorption of the edges of the spectral hole and the peak absorption of the AFC peaks. Most efficiency is obtained having a low peak absorption on the edges of the spectral hole. The motivation of this in the time-domain is that the slow light effect has to be small otherwise it will take to long time to build up a field in the cavity which is described in Subsection 23 D. The motivation in the frequency-domain is that the edges of the spectral hole should be as low as possible because the cavity peak is getting broader in frequency and can cover more of the AFC structure.
For $R_1 = 0.98$ and $R_2 = 0.9998$ which is chosen to be the reflectivity for these simulations the impedance matching conditions is fulfilled when the peak absorption of the AFC structure was 0.085 given that the finesse is $F = 8.5$. This value maximizes the efficiency in Figure 39 if the peak absorption of the edges are low enough.
In Figure 40 the absorption of the incoming field and the efficiency of the outgoing stored pulse were shown as a funtion of the peak absorption of the AFC peaks and the resonance frequency ω_c. The efficiency was at maximum for $\omega_c = 0$ Hz where the resonance frequency is given with respect to the detuning. The reason for the maximum to be at $\omega_c = 0$ Hz is that the incoming pulse ($\omega_L = 0$ Hz with respect to the detuning) and the AFC structure are centered around the zero detuning.
The conclusions of this section are that negative effects of the quantum memory efficiency and the absorption of the incoming pulse can be seen when the peak absorption of the edges and the resonance frequency are not optimal. These are important facts to know in order to realize a high efficient quantum memory with this type of setup. In these simulations it has been shown that, given that the experiment can be approximated and evolves according to the Equations (239)-(247), an efficiency over 80% can be obtained under perfect conditions with an AFC finesse of $F = 8.5$.

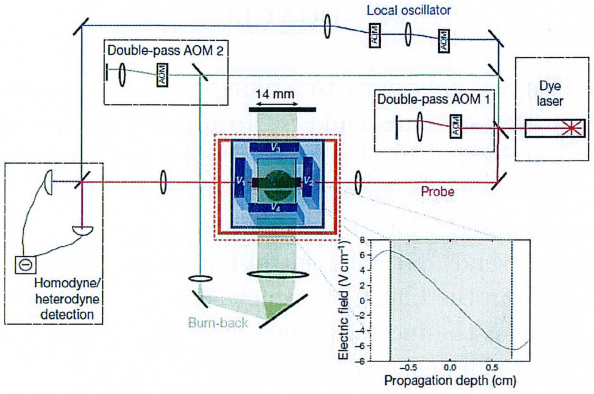

FIG. 42: Picture from [46], where the peak (burn-back) was created in the orthogonal direction relative the storage pulse propagation.

Part X
Hole-burning techniques

Making a spectral hole in the inhomogenous profile is a key concept for many applications. Both the CRIB and the AFC scheme (see Section VII) relies on the fact that there is one or several narrow peak(s) in the absorption profile. Near the peak(s) (in the frequency-domain) there should be ideally no absorbing ions in order to get a high-efficiency quantum memory. In this section a new scheme is introduced that improves the sharpness of structures at the edge of a spectral hole. The scheme is theoretically explained, moreover a proof-of-concept by Maxwell-Bloch simulations has been done to see how much improvement the scheme gives compared to old techniques.
Two main ways exists in order to burn a spectral hole. Either the burning is performed by pulses propagating in the same/opposite direction as the storage pulses or the buning pulses propagates in orthogonal direction relative the storage pulses. Both ways have different advantages and disadvantages.

25. THEORY

A. Burning in orthogonal direction relative the storage pulses

In 2010 a paper regarding quantum memories was published in Nature [46]. Experimental results had shown efficiency close to 70%. This experiment was done with the GEM protocol (see subsection 16 D 2). The need of an initial sharp peak is crucial to get high efficiency. In order to obtain a sharp peak they burned the structure from the orthogonal direction relative the storage pulse propagation. In Figure 42 the experimental setup is shown. Note that the burn-back beam is orthogonal to the probe direction. This way the peak will be uniform along the probe direction. For the purpose of a quantum memory this technique is very promising. In the case of a quantum memory the direction of the incoming pulse is well-defined in direction. Therefor the incoming pulse can be chosen to be orthogonal to the burn-back beam.
For other applications the direction of the incoming pulse is not well-defined. For example the direction might be randomly distributed. In this case burning in the orthogonal direction relative the storage pulses will not work since the orthogonal direction is undefined.

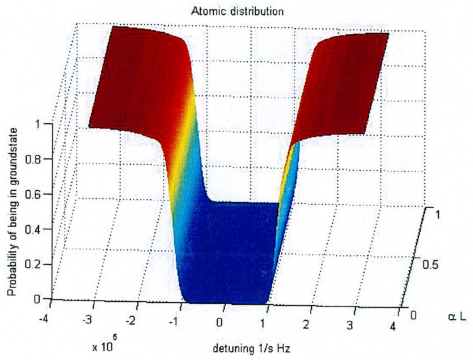

(a) Bloch simulator

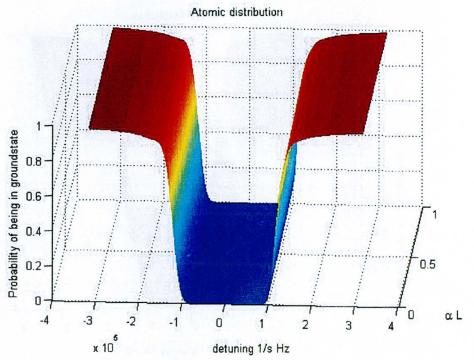

(b) Maxwell-Bloch simulator

FIG. 43: Example 1: The Bloch simulator and the Maxwell-Bloch simulator is compared for low optical depth. The goal is to burn a spectral hole. The simulators follow the approximations in Subsection 25 G. And the optical depth is chosen to be $\alpha L = 1$. Note that both result looks the same, and hence for this example the Bloch simulator is a good approximation of the Maxwell-Bloch simulator.

B. Burning in the same direction as the storage pulses

In Lund at the Quantum Information Group the hole-burning procedure is done by sending in burn pulses in the same direction as the storage pulses. The advantage of burning in the same direction as the storage pulses is that it's easy. The laser doesn't have to be aligned in any particular way since the storage pulses will go the exact same direction. Although the alignment is easier when burning in the same direction as the storage pulses, there is a problem in making structures that is uniform through the whole crystal.

C. The sharpness problem

Experimentally it has been seen that creating a structure in the inhomogenous profile in a crystal with low optical depth differs compared to a crystal with high optical depth. The reason for this is that the burning pulses are absorbed differently for different optical depth. Previous simulations in Lund at the Quantum Information Group has been done with a 2-level Bloch-simulator together with a program calculating the de-excitations in the crystal. These results were very successful when comparing with experiments for low αL. But for high αL the simulator suddenly didn't show the same result as experimental data.
A comparsion between the Maxwell-Bloch simulator and the Bloch simulator will be shown in order to see the difference. The Bloch simulator only consists of Eq. (142)-(144) whereas the Maxwell-Bloch simulator consists of Eq. (142)-(146). Therefore the difference between the simulators is that the Maxwell-Bloch simulator takes into account the spatial change in the burn pulses (the Maxwell part) while the Bloch simulator doesn't. Two examples will be shown in order to see the difference. Both examples are created by the simulator described in Subsection 25 G. The goal is to burn a spectral hole into an atomic distribution. In the first example shown in Figure 43, a low αL is used. It can be seen that the spectral hole in Figure 43a looks the same as in Figure 43b. Hence the simulators coincide pretty well. That is, the Bloch simulator is a good approximation to the Maxwell-Bloch simulator for low αL. In the second example a relatively high αL is used (see Figure 44) and as can be seen the results Figures 44a and 44b don't coincide. The conclusion why

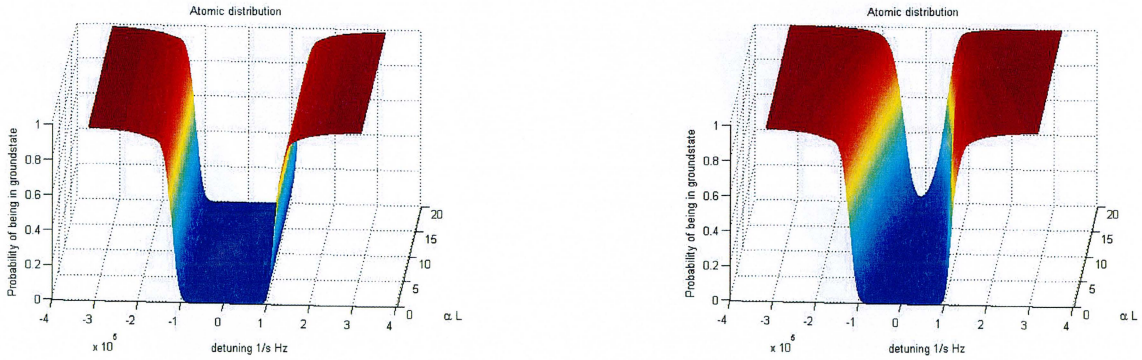

(a) Bloch simulator

(b) Maxwell-Bloch simulator

FIG. 44: Example 2: The Bloch simulator and the Maxwell-Bloch simulator is compared for high optical depth. The goal is to burn a spectral hole. The simulators follow the approximations in Subsection 25 G. And the optical depth is chosen to be $\alpha L = 20$. Note that both result don't look the same, and hence for high optical depth the Bloch simulator isn't a good approximation of the Maxwell-Bloch simulator.

Figure 44a and Figure 44b differs is that the Maxwell part in the Maxwell-Bloch simulator takes into account that the burning pulse is decreasing when exciting atoms as it propagates through the crystal. This means that the initial burning pulse will not look the same in the whole crystal for large αL due to absorption.
The fact that the burning pulse will get partially absorbed as it propagtes through an absorbing medium is obvious. But this effect is negative since many applications rely on the fact that the structure of the atomic distribution is uniform. A first solution to the problem would be to repeat the same pulse several times, but in fact this will not solve the problem completely. The reason is that the burning pulses are well-defined in time and hence the pulses has some tail in frequency and is not as sharp as wanted. The time- and frequency-domain are connected via the Fourier transform. For example the Fourier transform of a square pulse in time-domain gives a sinc function in frequency. This drawback will always exist if you can't use infinitely long pulses in the time-domain. The consequence for the burning procedure is that the front of the crystal will always contain less absorbing atoms than the back. As an example lets continue with Figure 44b and send in the same pulse 15 times (the simulations uses the approximation stated in Subsection 25 G). In Figure 45, one edge of the spectral hole can be seen at 5 different positions. The non-uniform effect through the crystal can be seen. If the burning pulse is repeated several times the front absorption will decrease outside the wanted interval due to that the incoming pulses are broad in the frequency domain.

D. A scheme to minimize the sharpness problem

From subsection 25 C it should be clear that repeating the burning pulse several times is not a very good solution to get a uniform and sharp edge for high αL.
In this part of the thesis a scheme to improve the uniformity and sharpness of the edges is proposed. The scheme is based on using the DC Stark effect to shift the atoms absorbing frequency both constant and linearly with the z-position.
There are several steps included in the scheme with some assumptions.
The first assumption is that the Stark splitting will split the resonance frequency into max two

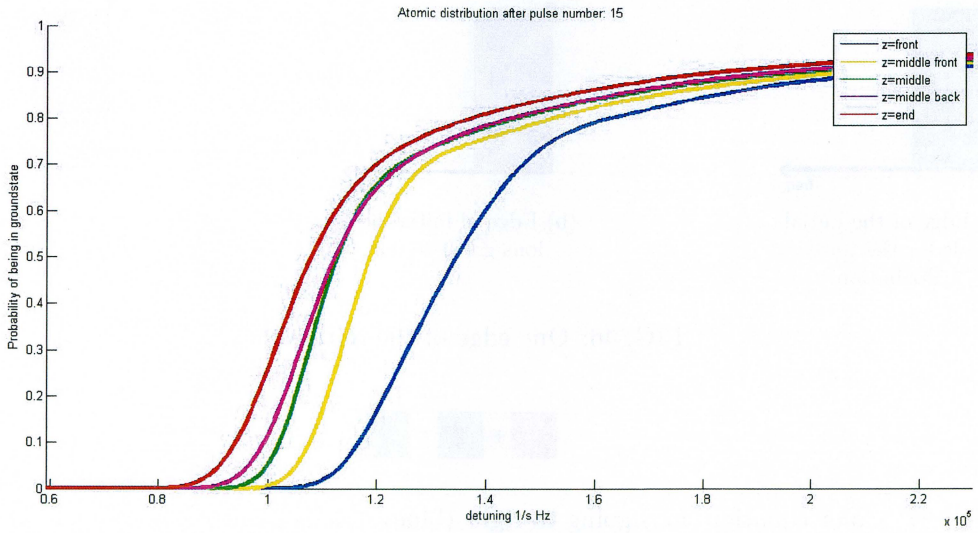

FIG. 45: Edge of a spectal hole with $\alpha L = 20$ plotted at 5 different positions inside crystal. The burning pulse is repeated 15 times. Note that the front of the crystal contains less absorbing ions than the back for any given frequency.

parts. For example crystals for the transverse CRIB protocol is not accepted (the transverse CRIB protocol assumes that the dipole moment has a random orientation with respect to the electric field, see subsection 16 D 1 for more details) while crystals for the AFC and the longitudal CRIB protocols are accepted (AFC and longitudal CRIB both can have crystal properties that has a maximum of two dipole moment orientation with respect to the electric field). Figure 6 demonstrates the effect for a $Eu : YAlO_3$ crystal with two dipole moment orientations with respect to the electric field where the energy levels are split into two parts, one part shifted to higher energies and the other part to lower energies.

The second assumption is that a tunable constant DC field can be applied as well as a tunable linear DC field as a function of z-position (like the linear shift in the GEM protocol in subsection 16 D 2).

In the following the scheme will be presented. In the result section a proof-of-concept for the scheme is done and in the conclusions the scheme is summarized in a list.

The idea of the scheme is to be able to burn away ions in the crystal in sections. By shifting ions differently in frequency for different z-position this will be possible. This way the front and the back of the crystal can get the same shape in principle.

The first step is to burn a hole through the crystal with as straight edges as possible (having a good initial pulse, without any applied electric field). This initial hole should be more narrow than the hole that is wanted. Suppose that this first step is completed, this is shown in Figure 46a. Figure 46a shows the total absorption inside the crystal for one edge of the spectral hole. It will be important to look seperately at the ions that shifts to the left (shift to lower frequencies) and to the right (shift to higher frequencies) when an electric field is applied. Figure 46b and Figure 46c represent the ions going to the left respectively the ions going to the right when an electric field is applied. Since there is no electric field applied at the moment these look the same. The sum for Figure 46b and Figure 46c gives Figure 46a and hence the equation in Figure 47 is used.

Suppose a linear electric field with respect to the z position is applied according to the following

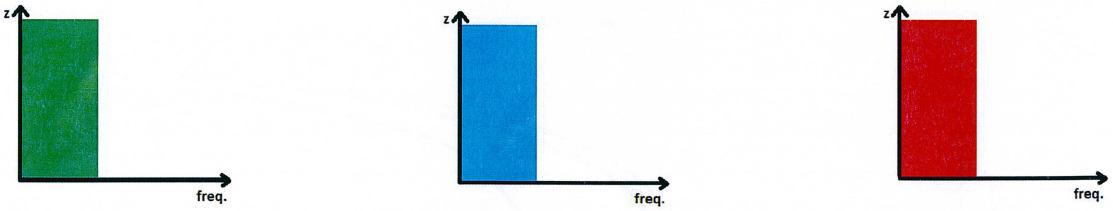

(a) Edge of the initial hole for the total distribution

(b) Edge of initial hole, ions going to left

(c) Edge of initial hole, ions going to right

FIG. 46: One edge of the initial hole.

FIG. 47: Color equation, ions going to right (blue) + ions going to left (red) = total ions distribution (green)

equation

$$\eta(z) = \eta_0 \cdot (z - L/2) \tag{266}$$

$$\eta_{left}(z) = -\eta_0 \cdot (z - L/2) \tag{267}$$

$$\eta_{right}(z) = \eta_0 \cdot (z - L/2) \tag{268}$$

where $\eta(z)$ is the linear frequency gradient, η_0 is the maximum strength of the electric field, L is the total length of the crystal. $\eta_{left}(z)$ describes how the ions that shift to the left (blue color) are changing their resonance frequency and $\eta_{right}(z)$ describes how the ions that shift to the right (red color) are changing their resonance frequency.
To get a feeling of how this would be done experimentally, Figure 48 is a small sketch of how four electrodes would be setup around the crystal. By just applying Eq. (266) the result will look like Figure 49a. Figure 49b and Figure 49c show the different components from Eq. (267) resp. Eq. (268).
By now it should be clear how a linear freqency gradient shifts the resonance frequency in the crystal. To continue explaining the scheme one problem arise with just using a linear frequency

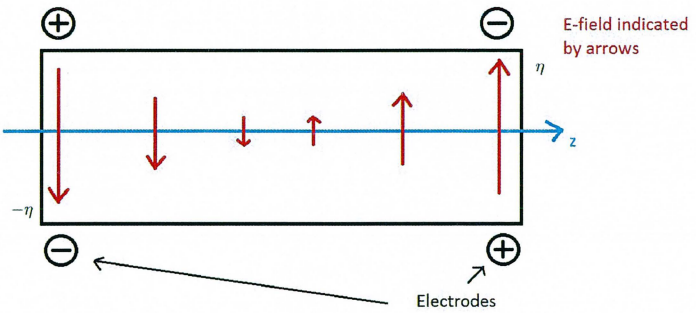

FIG. 48: Experimental sketch for how a linear electric field can be applied to a crystal. The electric field strength is indicated by the red arrows.

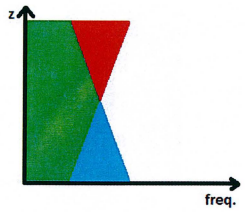

(a) Total distribution (summation of Figure 49b and Figure 49c according to the color equation in Figure 47).

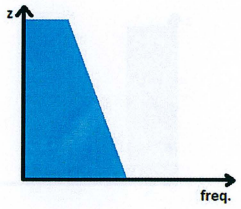

(b) Ions going to left by Eq. (267)

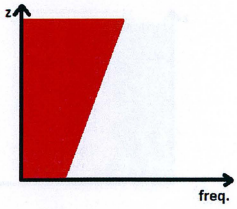

(c) Ions going to right by Eq. (268)

FIG. 49: Effect of a linear frequency gradient on the edge of Figure 46 by Eq. (266).

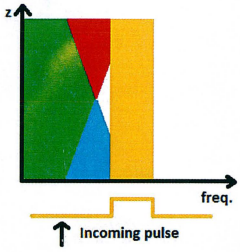

(a) Total distribution when a linear frequency is turned on and a burning square pulse comes in.

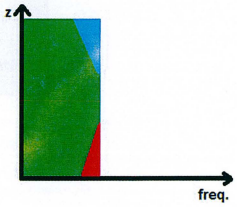

(b) Result after the electric field is turned off.

FIG. 50: Example of burning away some ions together with a linear frequency gradient. The incoming pulse is assumed to be a square pulse in frequency. Note that this type of burning procedure is not a wanted effect in order to get an uniform edge.

gradient given that the ions split into two parts. The problem is that if a pulse comes in it will burn away ions in the front of the ions going to left (blue color) and after that burn away ions going to the right (red color) in the end of the crystal. A non-uniform edge will be created and this is not wanted in this scheme. To see an example of this effect, suppose there is an square pulse in frequency coming in from $z = 0$ propagating to $z = L$ shown in Figure 50a. When the electric field then is turned off the result of the total distribution is shown in Figure 50b.
The trick to fix this problem which continues the explanation of the scheme is to add a constant electric field as well. The result of only having a constant electric field is shown in Figure 51. As can be seen the separation between the ions going to the left and ions going to the right is large. By applying a linear frequency gradient in addition to the constant electric field we can now access the back of the crystal without affecting the front (assuming that we have an ideal square pulse in frequency). The tunable electric field equations now look like:

$$\eta(z) = \eta_0 \cdot (z - L/2) + \eta_c \tag{269}$$

$$\eta_{left}(z) = -\eta_0 \cdot (z - L/2) - \eta_c \tag{270}$$

$$\eta_{right}(z) = \eta_0 \cdot (z - L/2) + \eta_c \tag{271}$$

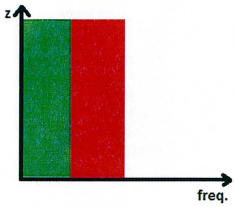

(a) Total distribution

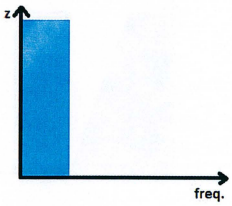

(b) Ions going to left by Eq. (267)

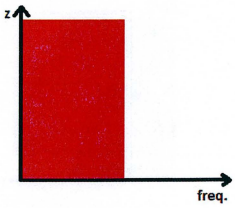

(c) Ions going to right by Eq. (268)

FIG. 51: Effect of a constant electric field on the edge of a spectral hole.

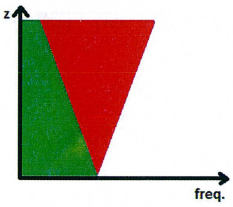

(a) Total distribution

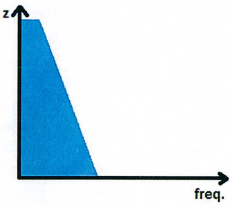

(b) Ions going to left by Equation 267

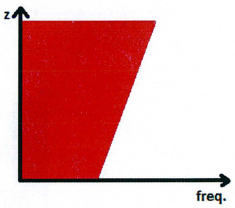

(c) Ions going to right by Equation 268

FIG. 52: Effect of a constant electric field together with a linear frequency gradient on the edge of a spectral hole.

where the parameters are the same as Eq. (266) and η_c is the strength of the constant electric field. This step can be seen in Figure 52 and now applying the square pulse in frequency, as in Figure 50a, only the back of the crystal is affected. The last thing to do in order to complete the scheme is to do the inverse (changing sign of the electric field) of Figure 52 to be able to burn in the back of the crystal on the ions going to left (blue).

E. Burning in the same and opposite direction as the storage pulses

There is another/complementing possibility to minimize the number of pulses sent in. This is to every second time send in a pulse from the opposite direction of the crystal. The effect will be that the ions in the middle will be the ones that has to be taken care of separately in order to get uniform and sharp edges. With the scheme in the previous subsection together with two extra electrodes this can be done. So this scheme presented below is an extension to the scheme in subsection 25 D. To get a feeling of how this would be done experimentally, Figure 53 is a small sketch of how 6 electrodes would be setup around the crystal. The set of equations can now be rewritten as

$$\eta(z) = \eta_0 \cdot (z - L/4)(\theta(z) - \theta(z - L/4)) - \eta_0 \cdot (z - 3L/4)(\theta(z - L/2) - \theta(z - L)) \quad (272)$$

$$\eta_{left}(z) = -\eta(z) \quad (273)$$

$$\eta_{right}(z) = \eta(z) \quad (274)$$

where $\eta(z)$ is the linear frequency gradient, θ is the Heaviside step function, η_0 is the strength of the electric field, L is the total length of the crystal, $\eta_{left}(z)$ is how the ions are shifted to the left (blue) and $\eta_{right}(z)$ is how the ions are shifted to the right (red).

To separate the blue ions from the red ions a constant field is applied. This effect together with

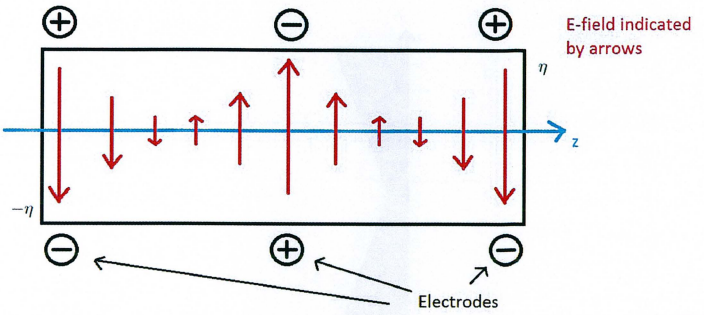

FIG. 53: Experimental sketch with 6 electrodes, the strength of the electric field are shown as red arrows.

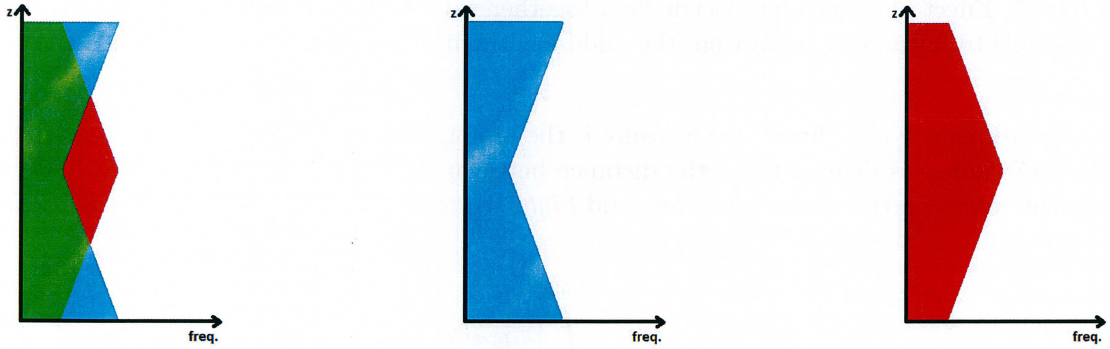

(a) Total distribution

(b) Ions going to left by Eq. (273)

(c) Ions going to right by Eq. (274)

FIG. 54: Effect of a frequency shift on the edge by Equation 272.

the effect of sending in a burn pulse is shown in Figure 55. This extra scheme would improve the uniformness of the burning procedure even more since the same structure can be created separately in the back, the front and the middle of the cystal without the effect of affecting each other.

F. Rules and definitions for the proof-of-concept

The making of a sharp uniform edge is not trivial. There are a lot of different variables, in other words this is a multi-dimensional optimization problem. To solve this problem optimally a clever optimization algorithm have to be used but this goes outside the scope of this thesis. The purpose of this proof-of-concept is only to show that it's possible to use the scheme and that it improves the sharpness. Two restrictions have been made for the proof-of-concept:

- Only two pulses are allowed, they are predefined.
- The initial hole is predefined and created by the widest pulse in frequency from the two pulses allowed.
- The electric field can be tuned constant and/or linear with respect to z-direction.

The concept is said to be proven if the edge can be made sharper and uniform than with either of the two pulses when no electric field involved.

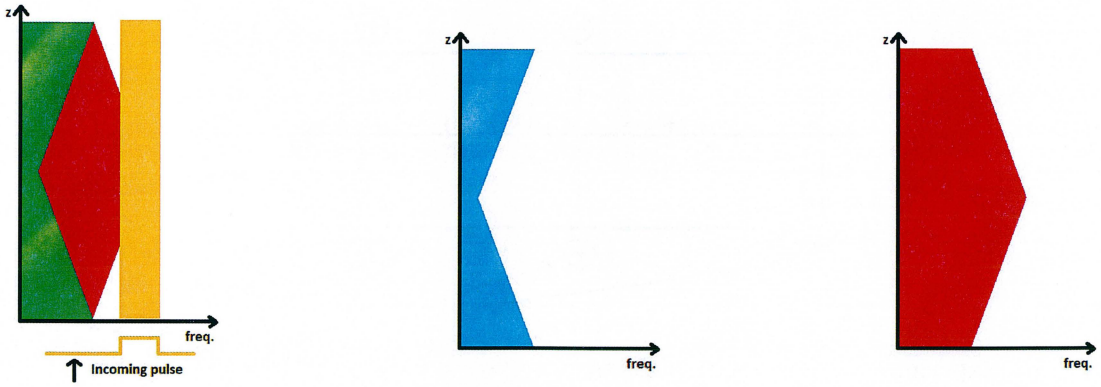

(a) Total distribution (b) Ions going to left (c) Ions going to right

FIG. 55: Effect of a constant electric field together with a frequency shift on the edge. It's now possible to burn away parts from the middle without affecting the front/back of the crystal.

Two measures will be defined, one measure is the uniformness and the other measure is sharpness. The uniformness is defined to be the distance between the front and back summed between two different values on the y-axis called *low* and *high*, see results in Table III. In mathematical terms this is:

$$u(low, high) = \frac{\int_{low}^{high} |x_{start}(y) - x_{end}(y)| dy}{high - low} \tag{275}$$

where u is the measure of uniformness, $x_{start}(y)$ (the blue curve) and $x_{end}(y)$ (the red curve) is the x-values for given y-values. The parameters is also shown in Figure 56, the uniformness is illustrated as the black area. The smaller the black area is the more uniform structure exists. Suppose that an average of all z-slices in a spectral hole is taken. Then the sharpness is defined to be the distance between on the x-axis for some y-values *low* and *high*. This is described by the following equation:

$$s(low, high) = |x(y = low) - x(y = high)| \tag{276}$$

where s is a measure for sharpness, $x(y)$ is the average curve of all z-slices, *low* and *high* are two chosen value between zero and one.

G. Approximations in simulating a spectral hole burning process

The Maxwell-Bloch equations will be used (derived in Section VI) with some additional approximation. When burning a spectral hole several pulses are sent into the material. Usually a long waiting time will occur between each pulse. This waiting time is important in order to let the ion de-excite. The de-excitation process is a key point since with some probability the ions can fall down into a third level that has a long lifetime. This process is called optical pumping [47].
In the following the additional approximation is described:

- For all discretized points in space and in frequency (detuning) there will be some or no excitation by the incoming burn pulses. The final excitation probability (the excitation

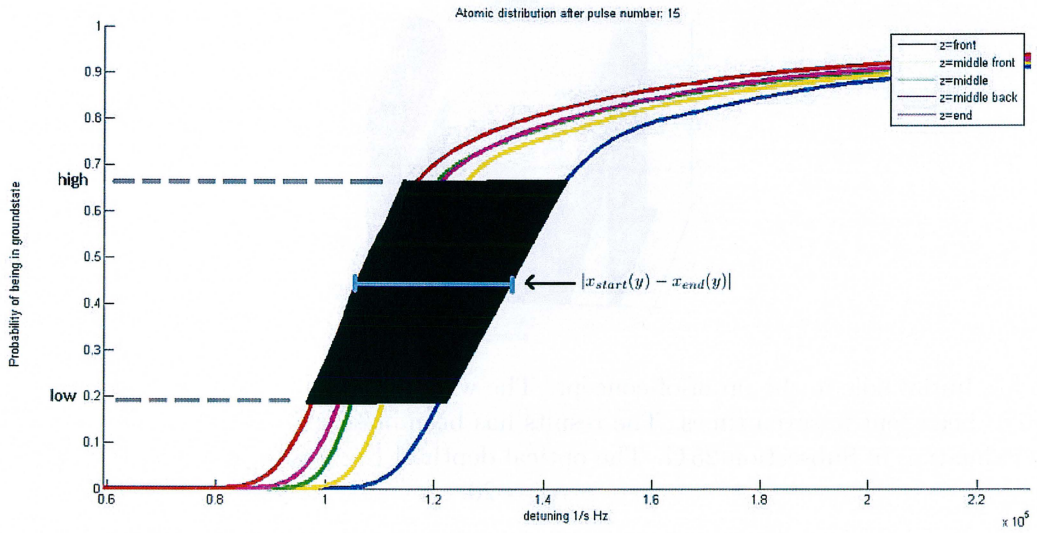

FIG. 56: Eq. (275) is shown in the figure. The black area is the definition of $u(low, high)$, $low = 0.19$ and $high = 0.67$ in this case.

probability is $(1 + r_z)/2)$, after the pulse has propagated through the sample, is with what probability that the ions will be assumed to drop down into a third level. This third level doesn't effect the 2-level system of interest (this is an approximation of optical pumping). This approximation relies on that the third level has a much longer lifetime compared to the two-level system being simulated.

26. RESULTS AND DISCUSSION

A proof-of-concept is going to be shown with simulations that follow the approximation in Subsection 25 G. The ions going to the left can be well separated from the ions going to the right due to an applied constant electric field (Figure 52), therefore the simulations will only care about the ions going to the right (red color). It is then assumed that the inverse is done in the same way for the ions going to the left by only applying a sign change to the electric field.
Two pulses are allowed according to Subsection 25 F. The initial hole is shown in Figure 57, this hole is made by sending in the widest predefined pulse in frequency seven times.
The scheme described in Subsection 25 D has been applied by using the second predefined pulse (this pulse is more narrow in frequency than the initial pulse that burned the spectrol hole in Figure 57) together with a lot of trial and error in selecting the constant and linear electric field. The result between the initial hole and the improved one by using the scheme can be compared in Figure 58.

As can be seen in Figure 58b the height of all curves to the right of the edge has decreased, this is a cost one have to pay when sending in extra pulses. This is an effect coming from the fact that the pulses is finite in time ($80\mu s$) in the simulations and therefore the pulse has a long tail in frequency. To see how well the scheme works compared to sending in each of the two pulses that was used in the simulations without any applied electric field is going to be plotted. In Figure 59 the two different predefined pulses can be compared, where the repetition of the pulses is chosen in a way to optimize the sharpness of the edge.

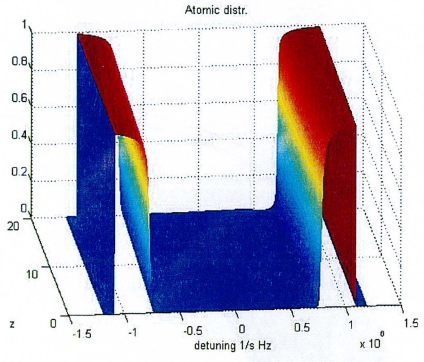

FIG. 57: Initial hole in the proof-of-concept. The widest pulse in frequency of the two allowed pulses has been sent in seven times. The results has been obtained by simulations that follow the approximation in Subsection 25 G. The optical depth of the peak absorption is chosen to be $\alpha_L = 20$.

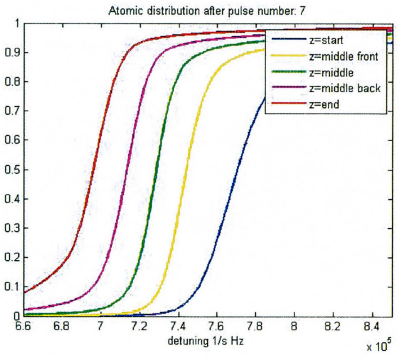

(a) Initial hole in the proof-of-concept. From Figure 57.

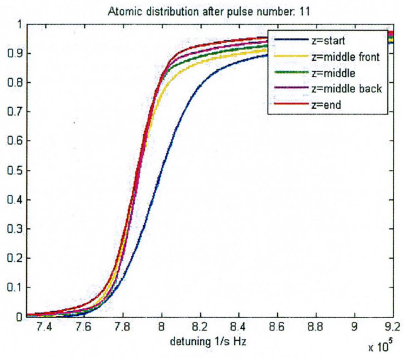

(b) The narrow pulse is repeated 4 times for different linear frequencies.

FIG. 58: Comparsion between the inital hole from Figure 57 and the improved edge create by the described scheme in Subsection 25 D. Note that the improved edge is not at the same frequency as the inital hole due to the extra pulses that is sent in.

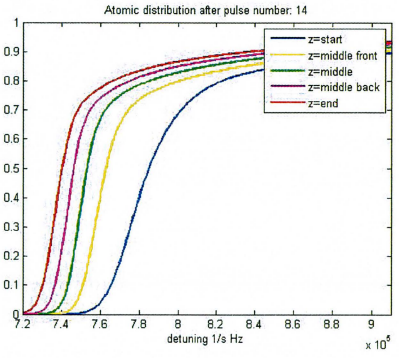

(a) Inital/widest pulse in frequency repeated 14 times.

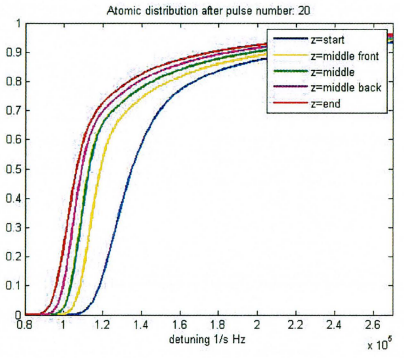

(b) Most narrow pulse in frequency repeated 20 times.

FIG. 59: Compare the two predefined pulses without frequency shift.

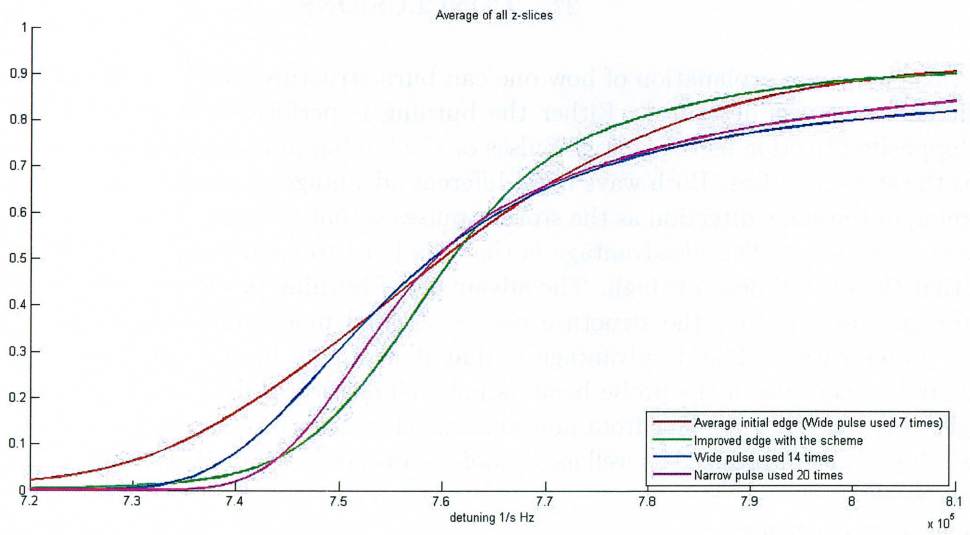

FIG. 60: Average of all z-slices to see difference of the sharpness of the edge.

TABLE III: Comparsion with Eq. 275 with $low = 5\%$ and $high = 85\%$.

Figure	**Description**	**u (in units of** 0.1 **MHz**
58a	7 wide pulses	4.94
-	9 wide pulses	3.91
59a	14 wide pulses	3.18
-	7 narrow pulses	5.69
59b	20 narrow pulses	1.90
58b	7 wide pulses and then apply tuned electric field with 4 narrow pulses	0.87
-	7 wide pulses and then apply tuned electric field with 6 narrow pulses	1.38

As the number of pulse repetition increases the Eq. (275) decreases if no electric field is applied. So the more pulse repetition the more uniform distribution. This is obvious by taking the example to send in infinitely many pulses (given that the third-level lifetime is infinite). This will create a non-existing edge and hence all z-slices will look the same. Another way to see the difference between the different populations is to take an average of all the z-slices, this is done in Figure 60. Note that the more pulses one sends in comes with the price that the absorption after the edge becomes lower (right side of the Figure 60). In Table IV the values Eq. (276) is chosen to $low = 5\%$ and $high = 85\%$.

Eq. (276) is a function that can be minimized in an optimization algorithm to find local/global minima.

27. CONCLUSIONS

In this part some explanation of how one can burn structures in the inhomogenous broadening in different ways was described. Either the burning is performed by pulses propagating in the same/opposite direction as the storage pulses or the buning pulses propagates in orthogonal direction as the storage pulses. Both ways have different advantages and disadvantages. The advantage of burning in the same direction as the storage pulses is that it's easy to know the direction to send in the storage pulse. The disadvantage is that it's hard to create a uniform and sharp structure given that the optical depth is high. The advantage of burning in the orthogonal direction relative the storage pulses is that the structure can be created more uniform in the direction that the storage pulses enters. The disadvantage is that it might be hard to know where to send in the storage pulse. But also if the probe beam is not well defined in direction or randomly distributed in angle, this scheme will suffer from non-uniform/sharpness problems as the other ones.
A new scheme was introduced as well as a proof-of-concept by simulations showing that the scheme actually works.
Summary of the scheme:

- Burn an inital hole that is more narrow in frequency than wanted.
- Use a constant electric field together with a linear frequency gradient field that is depending on z-direction. The constant electric field is needed when the distributions is splitted in two parts
- Tune the linear frequency gradient so that the end of the crystal is reached and then send in a more narrow pulse in frequency. This way different parts in the crystal can be treated more or less seperately and hence a uniform structure can be made.
- After each narrow pulse change the linear frequency gradient so that the end result will be uniform.
- Repeat the procedure but with a sign change of the electric fields, that way both the ions going to the left and the ions going to the right is affected equally.

Things to remember:

- The pulses is limited in time so the pulses has long tails in frequency.
- In order to keep as much of the atomic distribution outside of the pit as high as possible don't send in too many pulses. This is due to the frequency tails.

TABLE IV: Comparsion with Eq. 276 with $low = 5\%$ and $high = 85\%$.
Proof-of-concept*=7 wide pulses and then apply tuned electric field with 4 narrow pulses

Curve in Figure 60	**Description**	**s (in units of 0.1 MHz**
Red	7 wide pulses	3.99
-	9 wide pulses	3.81
Blue	14 wide pulses	5.24
-	7 narrow pulses	2.99
Purple	20 narrow pulses	4.37
Green	Proof-of-concept*	2.62
-	Proof-of-concept*	3.31

- The sharpness problem is a multi-dimensional optimization problem. To use this scheme optimally, a smart optimization algorithm is required together with for example Eq. (276) in order to find local/global minimas. Eq. (276) is a measure of how sharp an edge is.
- All comparsion tables and figures described above is only a proof-of-concept done with trial and error. The improved edge is most uniform according to Eq. (275) and most sharp according to Eq. (276) with $low = 5\%$ and $high = 85\%$ seen in Tables III and IV.

Part XI
Summary

This thesis have theoretically investigated three different problems that all concern highly efficient quantum memories. The method of investigation was to numerically solve a set of equations. The main set of equations that were used are called the Maxwell-bloch equations, this is a semi-classical model where the ions are evolving according to quantum mechanics in the dipole approximation and the incoming electric field by Maxwell's wave equation. The connection between quantum mechanics and Maxwell's equations is that the ions contributes to a macroscopic polarization that affect the electric field.
The main conclusions for all three problem will be listed:

1. Transverse/longitudal CRIB and AFC are three different quantum memory protocols. Every protocol has advantages and disadvantages: CRIB relies on a frequency shift of the ions in order to send out the stored pulse, the Stark effect can be used to make this possible. The AFC protocol don't need a frequency shift, but instead it's the periodic structure in the inhomogenous profile that makes it possible to send out a stored pulse. The AFC and transverse CRIB protocol doesn't give high efficiency in the forward direction while in the backward direction efficiency close to unity is possible. Longitudal CRIB can give efficiency close to unity in the forward direction but introduces a phase shift to the outgoing field.
   Three different shapes of the peaks inside the inhomogenous profile were used to see how much the efficiency is affected. It turns out that the shape is very important and in the three cases that were tested the supergauss shape was in favor of a gauss or a lorentz shape.

2. A new experimental setup where a rare-earth-ion-doped crystal together with a cavity has been put together at the Quantum information group in Lund. The experimental results was explained in this thesis. The cavity resonance peak for a cold cavity is in the order to GHz whereas inside the spectral hole the cavity resonance peak is in the order of MHz. It turns out that the cavity resonance peak is proportional to the group velocity. The group velocity inside a spectral hole is approximately three orders of magnitude lower than the phase speed of light in vaccum. The experimental results were matched to the theoretical result and a fair agreement between these two was found.
   A set of equations based on the Maxwell-Bloch equantions for a cavity was derived and showed that under perfect circumstances the new experimental setup together with the AFC protocol can give efficiency over 80%. But if the edges of the spectral hole are to high compared to the AFC peaks or if the cavity is not perfectly on resonance the efficiency will be greatly reduced.

3. Creating sharp structures inside the spectral hole is important for the quantum memory protocols. A new scheme was explained that allows creation of a more sharp and uniform strucuture inside the inhomogenous profile relying on the Stark effect. A proof-of-concept with the Maxwell-Bloch equations showed that this scheme works in principle, but to get optimal values a multi-dimensional optimization algorithm is required.

[1] Wolfgang Tittel Nicolas Gisin, Gregoire Ribordy and Hugo Zbinden. Quantum cryptography. *REVIEWS OF MODERN PHYSICS, VOLUME 74*, 2002.
[2] Rob Thew. Qurep, quantum repeaters for long distance fibre-based quantum communication, October 2010.
[3] S. A. Moiseev and S. Kröll. Complete reconstruction of the quantum state of a single-photon wave packet absorbed by a doppler-broadened transition. *Phys. Rev. Lett.*, 87(17), 2001.
[4] M. P. Hedges, J. J. Longdell, Y. M. Li, and M. J. Sellars. Efficient quantum memory for light. *Nature*, 465(7301):1052–1056, June 2010.
[5] Hugues de Riedmatten Mikael Afzelius, Christoph Simon and Nicolas Gisin. Multimode quantum memory based on atomic frequency combs. 2008.
[6] M.Sabooni M.Huang S.Kröll M.Afzelius I.Usmani B.Lauritzen N. Sangouard H.de Riedmatten N.Gisin A. Amari, A.Walther. Towards an efficient atomic frequency comb quantum memory. *Journal of Luminescence 130*, pages 1579–1585, 2010.
[7] Samuel Tornibue Kometa. Quantum state storage in a rare-earth doped crystal, placed inside a cavity. Master's thesis, Lund university, 2011.
[8] M. Afzelius and C. Simon. Impedance-matched cavity quantum memory. *Physical Review A*, 82(2), 2010.
[9] M. A. Nielsen and I. L. Chuang. *Quantum computation and quantum information.* Cambridge University Press, 2000.
[10] Renato Renner. *Lecture Notes, Quantum Information Theory.* 2010.
[11] Wikipedia. Qubit. http://en.wikipedia.org/w/index.php?title=Qubit&oldid=426786871, 2011.
[12] David McMahon. *Quantum Computing Explained.* 2008.
[13] Sven Spanne. *Föreläsningar i Matristeori.* 1997.
[14] Persson och Biers. *Analys i flera variabler.* 2005.
[15] J. I. Cirac H.J. Briegel, W. Dur and P. Zoller. Quantum repeaters for communication. *Arxiv, quant-ph/9803056v1.*
[16] Matthieu Legr'e. Quantum repeaters for the novice. http://quantumrepeaters.eu/index.php/qcomm/quantum-repeaters, 2010.
[17] Qiang Zhang Yu-Ao Chen Kai Chen Jorg Schmiedmayer Alexander M. Goebel, Claudia Wagenknecht and Jian-Wei Pan. Multistage entanglement swapping. *PHYSICAL REVIEW LETTERS PRL 101, 080403*, 2008.
[18] Wikipedia. Rotating wave approximation. http://en.wikipedia.org/w/index.php?title=Rotating_wave_approximation&oldid=420452237, 2011.
[19] C. S. Cornish. *Highly efficient photon echo generation and a study of the energy source of photon echoes.* PhD thesis, 2000.
[20] Unpublished N. Sangouard, 2009.
[21] Christopher J. Foot. *Atomic Physics.* 2005.
[22] Mattias Nilsson. *Coherent interactions in rare-earth-ion-doped crystals for applications in quantum information science.* PhD thesis, Division of Atomic Physics, LTH, 2004.
[23] Franz X. Kaertner. 6.977 ultrafast optics. Website, 2005.
[24] Frank Trager. *Springer handbook of lasers and optics.* Springer, 2007.
[25] A. E. Siegman. *Lasers.* University science books, Mill Valley, California, 1986.
[26] L. Mandel and E. Wolf. *Optical Coherence and Quantum Optics.* Cambridge University Press, New York, October 1995.
[27] Wolfram Math World. Chain rule. http://mathworld.wolfram.com/ChainRule.html, 2011.
[28] Wikipedia. Runge kutta methods. http://en.wikipedia.org/w/index.php?title=Runge_Kutta_methods&oldid=423705060, 2011.
[29] Andreas Walther. *Coherent processes in rare-earth-ion-doped solids.* PhD thesis, Lund University, 2009.
[30] W. Tittel A. I. Lvovsky, B. C. Sanders. Optical quantum memory. 2010.
[31] M. Nilsson and S. Kröll. Solid state quantum memory using complete absorption and re-emission of photons by tailored and externally controlled inhomogeneous absorption profiles. *Opt. Commun.*, 247:393–403, 2004.

[32] Mikael Afzelius Nicolas Sangouard, Christoph Simon and Nicolas Gisin. Analysis of a quantum memory for photons based on controlled reversible inhomogeneous broadening. *PHYSICAL REVIEW A 75, 032327*, 2007.
[33] A. L. Alexander-P. K. Lam G. Hetet, J. J. Longdell and M. J. Sellars. Photon echoes produced by switching electric fields. *PHYSICAL REVIEW LETTERS PRL 100, 023601*, 2008.
[34] P. K. Lam J. J. Longdell, G. Htet and M. J. Sellars. Analytic treatment of controlled reversible inhomogeneous broadening quantum memories for light using two-level atoms. *PHYSICAL REVIEW A 78, 032337*, 2008.
[35] Mikael Afzelius and Christoph Simon. Impedance-matched cavity quantum memory. *PHYSICAL REVIEW A 82, 022310*, 2010.
[36] Sergey A. Moiseev Sergey N. Andrianov and Firdus F. Gubaidullin. Efficient multimode quantum memory based on photon echo in an optimal qed cavity. *PHYSICAL REVIEW A 82, 022311*, 2010.
[37] M.C. Teich B.E.A Saleh. *FUNDAMENTALS OF PHOTONICS*. Second edition, 2007.
[38] P . W . Milonni. *Fast Light, Slow Light and Left-Handed Light*. Taylor & Francis, 2004.
[39] E. Hecht. *Optics*, volume 2nd. Addison-Wesley, 1987.
[40] Wikipedia. Geometric series. http://en.wikipedia.org/w/index.php?title=Geometric_series&oldid=427317647, 2011.
[41] Daniel J. Gauthier and Robert W. Boyd. Fast light, slow light and optical precursors: What does it all mean? *Photonics spectra*, 2007.
[42] Nan Lin. An investigation of slow light and time delay-bandwidth in pr3+:y2sio5 by using persistent spectral hole burning technique. Master's thesis, Lund university, 2010.
[43] Willis E. Lamb Jr. Theory of an optical maser. *Physical Review, Volume 134, Number 6A*, 1964.
[44] Lei Stone Meng. *Continuous-wave Raman Laser in H2: Semiclassical Theory and Diode-pumping Experiments*. PhD thesis, Department of Physics Montana State University, 2002.
[45] Wikipedia. Natural logarithm. http://en.wikipedia.org/w/index.php?title=Natural_logarithm&oldid=426024694, 2011.
[46] Yongmin Li & Matthew J. Sellars Morgan P. Hedges, Jevon J. Longdell. Efficient quantum memory for light. *Nature Vol 465*, 2010.
[47] MIT Department of Physics. Optical pumping, 2011.